DOE Award No.: DE-FE-0009963

Final Research Performance Report (Period: 10/01/2012 to 12/31/2016)

Measurement and Interpretation of Seismic Velocities and Attenuations in Hydrate-Bearing Sediments

Project Period (10/1/2012 to 12/31/2016)

Submitted by: PI Manika Prasad
Colorado School of Mines (DUNS #010628170.)
1500 Illinois Street
Golden. CO 80401
e-mail: mprasad@mines.edu
Phone number: (303) 273-3457

Submission Date: 1/31/2017

M. Prasad

Prepared for: United States Department of Energy
National Energy Technology Laboratory

Office of Fossil Energy

Disclaimer

Table of Contents

List of Figures

A. Studies Undertaken

1. **Micro X-ray CT Imaging under Confining Pressure**: We developed a pressure vessel and ultrasonic transducers suitable for the use in the micro CT machine. We tested functionality of the pressure and temperature control system and demonstrated that changes in rock samples can be imaged within the resolution constraints of the Xradia-400 machine. We observe compaction of samples subjected to confining pressures resulting in grain damage and fracturing of sediment grains. When the confining pressure was decreased some cracks experienced further fracturing. The grain damage is irreversible. Further fracturing of grains in pre-compacted sediment was observed upon repeated confining pressure cycling. We could also image and document presence of residual water after hydrate formation. Furthermore, we could capture compaction of clay due to hydrate formation in the pore space.
2. **Seismic Velocity and Attenuation Measurements:** We used an instrumented pressure vessel to perform ultrasonic and seismic measurements. We tested unconsolidated sediments, sand, clay, and sand-clay mixtures, as well as sandstones containing with different amounts of THF and CH4-hydrates.
3. **Complex Resistivity Measurements:** We included feed-throughs with electrical wires for a pressure vessel which was used to perform ultrasonic and complex resistivity measurements. This updated setup was pressure tested. Nine samples were prepared to perform ultrasonic and complex resistivity measurements during hydrate formation.
4. **NMR studies:** We demonstrated the use of NMR spectra to understand hydrate formation and dissociation. The collected NMR spectra are constant and consistent when hydrate equilibrium is reached in closed systems. We find that existence of fluid interfaces in partially dissociated hydrate samples in a closed system that are believed to give late time NMR T2 response.
5. **Theoretical Models:** Theoretical models correlate different pore-scale hydrate distributions and their impact on ultrasonic velocities. Also, Thermodynamic models of the phase behavior CH4 – CO2 – H2O system provided us with the equilibrium phases at various pressures and temperatures.
6. **Comparison of Well Log Data and Laboratory Measurements:** We compared log data on velocity and attenuation with our laboratory data. The comparison was made via a so-called “Loss Diagram” that allows separation between bulk and shear losses. This separation can in turn allow deductions about the loss mechanisms that might aid in remote sensing of hydrate-bearing sediments from seismic data.

B. Major Findings

Free water presence: We successfully performed electrical conductivity measurements on Castlegate Sandstone samples before and after methane hydrate formation. Our measurements show that we can distinguish initiation and completion of the hydrate formation process. Our electrical conductivity measurements also corroborated our previously reported observation that even after the hydrate formation was completed, we still had free water in the sample which was turned into ice after lowering the temperature below the freezing point of water.

Hydrate Location: We performed **u**ltrasonic velocity measurements on sandstones, sand-clay mixtures, and pure sand (Ottawa sand F110) with different THF hydrate saturations (60% and 40%). We observe increasingly smaller velocity increases due to hydrate formation with decreasing hydrate saturation. This observation suggests that at low concentration, hydrate are not cementing. A further confirmation of non-cementing hydrates at low hydrate concentration is the larger increase in velocities with increasing confining pressure. A cementing hydrate would create a stiffer framework and prevent large compaction-driven increases in velocity. We also find that the effect of hydrate cementation is more pronounced in Vp-Vs ratios. These measurements provide a diagnostic tool to detect hydrate saturations.

Data comparison and dissemination: We obtained velocity and attenuation data for methane hydrates formed using the excess gas and excess water method. Data from the excess gas method shows that already small amounts of hydrate have a strong influence on the Vp-Vs ratio (hydrate saturations of about 3%). Whereas the data from methane hydrates formed with the excess water method shows that changes start to occur at higher gas hydrate saturations (>30 %). A comparison of methane hydrate data formed using the excess water method with our THF hydrate data show a great match. In both cases, the decreases in Vp-Vs ratio with increasing hydrate saturation are comparable.

C. Implications of Research

Research Objectives

An over-arching goal of this research is to calibrate geophysical techniques for hydrate exploration, evaluation, and production monitoring. Extensive field data of hydrate-bearing sediments exist, but quantitative estimates of the amount and distribution of hydrates are difficult to determine.

Thus, the primary project objectives were to relate seismic and acoustic velocities and attenuations to hydrate saturation and texture. The project aimed to collect seismic properties along with other measurements (e.g., complex resistivity, micro-focus x-ray computed tomography, etc.). The multiphysics dataset would enable researchers to understand not only the interaction between mineral surfaces and gas hydrates, but also how the hydrate formation method affects the hydrate-sediment system in terms of elastic properties.

Ultimately, the suite of measurements acquired in this project would

- Allow interpretations of borehole and surface data to derive hydrate saturation
- Provide a means of calibrating geophysical field data
- Provide insight into the formation of natural gas hydrate deposits
- Improve the ability to detect and evaluate hydrates in the subsurface
- Provide impetus for feasible, economic, and safe production schemes for natural gas hydrates.

Research Achievements and Key Advances

1. **Technical Achievements**: We have successfully designed multiphysics measurements for
    - Simultaneous acoustic measurements during quantifiable hydrate formation under controlled pressure and temperature conditions.
    - Acoustic and / or complex conductivity measurements during quantifiable hydrate formation under controlled pressure and temperature conditions.

2. **Scientific Achievements**: Our measurements have shown that:
    - ***Presence of Free water even after hydrate formation*:** Complex conductivity and NMR experiments confirm our acoustic and MXCT observations: there is evidence of a layer of water around the grains even at high hydrate conversion. The results are same for THF and methane hydrates. The water layer coating the grains alters indirect geophysical measurements
    - ***Hydrate location changes with hydrate saturation**:* Ultrasonic velocity measurements show that at low concentration, hydrates are not cementing. As hydrate saturation increases, acoustic data show evidence of hydrate cementation.

- ***Vp-Vs ratio useful as diagnostic tool for hydrate saturations:*** Higher hydrate saturations decrease Vp-Vs ratios significantly, while reducing hydrate saturations lead to increase in Vp-Vs ratios. THF and methane hydrates formed with the excess water method show similarities. An increase in confining (or overburden) pressure decreases the Vp-Vs ratio due to compaction.
- ***Loss Diagram as a diagnostic tool****:* Our data compilation has shown the usefulness of a "Loss Diagram" (Qp/Qs versus Vp^2/Vs^2) to diagnose major loss mechanisms associated with hydrate saturations and location. An increase in hydrate saturation leads to lower Qp/Qs and Vp^2/Vs^2; the major loss mechanism changes from primarily bulk losses to equal amounts of bulk and shear losses.

Implications and Applications

1. Bulk water present in the matrix together with hydrates gives rise to high attenuation in hydrate-saturated sediments. This attenuation can be a key diagnostic tool to analyze seismic amplitudes.
2. Since the change in hydrate location with changing hydrate concentration are detectable with velocity and Vp-Vs ratios. The significant Vp-Vs ratio change with hydrate saturation has the potential to differentiate between hydrates and no-hydrates where BSR are detected by seismic.

Avenues for Future Follow-on Research:

1. Confirm the laboratory data with well log data by creating a loss diagram from sonic scanner and dipole sonic logs
2. Forward model velocity and attenuation values for different hydrate saturations to establish realistic scenarios of seismic detection of BSRs.
3. Develop attenuation models for a three-phase saturation (water, hydrate, and gas) in hydrate-bearing sediments, possibly cemented by hydrates. Current models are too simplistic to efficiently capture the phenomena and thus leave room for opposing interpretations.
4. Acquire good quality seismic data to combine experimental results with seismic interpretations and forward models.

D. Status of Milestone Completion

Milestone	**Title / Description**	**Status towards completion / Date of Completion**
Task 1	Project Management Plan Development	**Complete & approved** **Date:** 12/1/2012
Task 2	Low Frequency Equipment Upgrades	**Complete & approved** **Date:** 6/1/2013
Task 3	Hydrate Thermodynamic Modeling	**Complete & approved** **Date:** 5/31/2014
Task 4	Acquire In Situ Data (logs)	**Complete & approved** **Date:** 5/31/2014
Task 5	THF hydrate-saturated Rock measurement	**Complete & approved** **Date:** 6/15/2014
Task 6	THF hydrate grown in pressure vessel	**Complete & approved** **Date:** 4/15/2014
Task 7	CH4 hydrate from free gas Measurements	**Success:** Made hydrates from free gas and have conducted electrical measurements on the CH4 hydrate bearing sediments. Completed acoustic measurements. (Students will continue to perform experiments for their theses.) **Date:** 1/31/2017
Task 8	CH4 hydrate (gas in solution) measurement	**Unsuccessful**: Work planned however, experiments were unsuccessful **Date**: 12/31/2016.
Task 9	CO2-CH4 replacement hydrate measurement:	**Abandoned:** After reading various other studies and consulting with our co-I, Dr. Carolyn Koh, and given the delays in equipment reliability, we decided to abandon these efforts and focus instead on the CH4 hydrates first. Initial results were reported in earlier reports
Task 10	MXCT Scanning Characterization	**Success: Measurement system:** We built a new set of ultrasonic P-wave transducers and a new aluminum pressure cell for the use inside of the CT scanner with a bigger inner diameter than the previously used Torlon cell.

		The cell has been pressure tested and the ultrasonic transducers have been proven to work. **Success**: **MXCT scans under pressure:** Completed MXCT scans of various hydrates that made in our labs. The in situ hydrate imaging under pressure is also completed **Date**: 12/31/2016.

Figure 1. Milestone status with dates of completion for each Milestone (continued on next page).

Task 11	Model Laboratory Measurements	**Success:** Created models to explain experimental data in context of the various hydrate-forming habits. The most rewarding aspect of our work has been that we can demonstrate a gradual shift of hydrates from pore filling to framework and cementing locations with increasing hydrate concentration **Date**: 1/31/2017.
Task 12	Comparison with Log Data	**Success:** Here, we have compiled a large amount of data both in our own laboratories as well as from other researchers. This compilation of data shows clearly that we should be able to separate large concentrations of hydrates in sediments from minor amounts using shear and compressional wave data. **Date**: 10/31/2016.
Task 13	Technology Transfer	**Success**: Two papers published, numerous conference papers (SEG, ICGH, AGU); one paper accepted; two more papers underway. **Date**: 10/31/2016.

Figure 1. Milestone status with dates of completion for each Milestone.

E. Detailed Descriptions

1. Micro X-ray CT Imaging under Confining Pressure

Experimental Method

The goal of this work is to make µCT images of hydrate-bearing sediments while pore and confining pressure is applied. The MicroXCT-400 apparatus from XRadia was used for the MXCT measurement. The initial sample holder consisting of two dry-ice containers at the top and bottom and a plastic tube for the sample in between has been used to perform the measurements (Figure 2). This setup provided a temporary cooling of the sample to keep the hydrate stable long enough to scan it. Data acquisition for one tomography took about 20 minutes, allowing the examination of hydrate dissociation. In the final version of the experiment, we implemented pressure and temperature control system inside the Xradia-400 µCT machine. The temperature control was intended for scans of gas-hydrate bearing sediments. In addition to pressure and temperature control, we measure ultrasonic P-wave velocities simultaneously with µCT imaging. The combination of imaging and velocity measurements allow us to gain insight on the influence of pore-scale changes on elastic properties. The confining pressure stability is able to maintain confining pressures up to 13.8 MPa (2000 psi) for periods of more than 20 hours leading to a significant improvement in µCT image resolution to 5 µm.

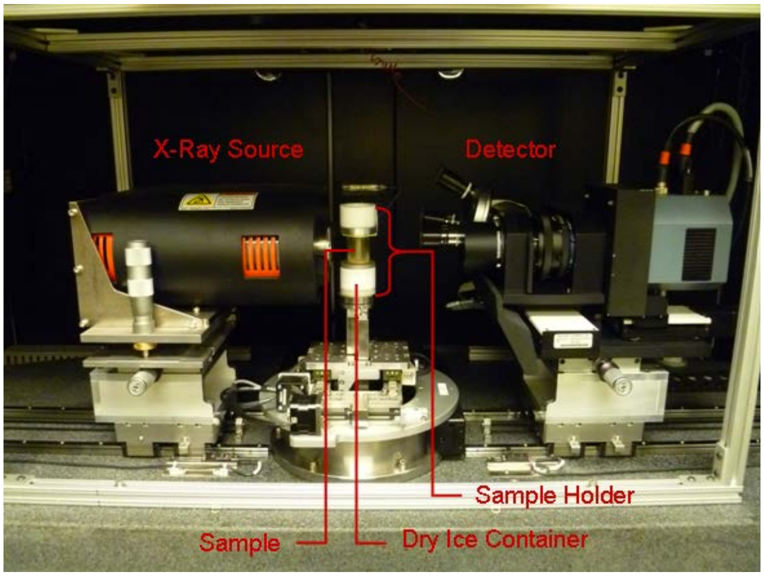

Figure 2: Experimental setup inside the CT scanner

Initially, the hydrate was formed outside of the CT scanner prior to the image acquisition. The samples were formed in cylindrical plastic containers with a volume of 1.1 ml. The laboratory samples characterized by MXCT measurements consisted of borosilicate glass beads (diameter: 1 mm), de-ionized water, THF and barium chloride. All samples had a porosity around 30%. H_2O-THF ratios resulting in 20%, 40%, 60%, 80% and 100% hydrate saturation have been used. After combining all sample compounds, the sample was sealed to prevent the THF from volatizing and water from evaporating. The samples were then stored in a freezer, where they were slowly cooled to -25°C over a time period of about 48 hours. The samples were cooled to -80°C for one hour to avoid immediate dissociation of the hydrate before scanning.

MXCT measurements allow the distinction between materials with different bulk densities. They provide insight into the distribution of different sample components in the pore space. In contrast to sediment grains, glass beads have uniform density (2.23 g/cm^3), X-ray absorbance value, and shape. These properties make it easier to interpret the bulk MXCT images. To enhance the density contrast between ice and hydrate, 5 wt% barium chloride was added to the fluid mixture. The density contrast for a sample with 60% hydrate saturation for example is increased by five times when barium chloride is added. As the hydrates form, barium chloride is excluded from the hydrate structure and freezes within the water phase.

The dissociation process was monitored by taking six consecutive tomographies. For each tomography, 200 images were taken with an angular increment of 1°. The low number of images and the big angular increment were chosen in order to minimize the scanning time. An X-ray source voltage of 90 keV and a power of 7 Watt were used for the tomographies. The scanning time for one series of six tomographies was about 2 hours.

The output data of the MXCT scanner are gray scale images. Different gray values represent materials with different bulk densities. Dark gray areas indicate low bulk density, light gray to white areas correspond to high bulk density.

Sample Holder for the MXCT

With the Xradia-400 µCT machine. The temperature control was intended for scans of gas-hydrate bearing sediments. In addition to pressure and temperature control, we measure ultrasonic P-wave velocities simultaneously with µCT imaging. The combination of imaging and velocity measurements allow us to gain insight on the influence of pore-scale changes on elastic properties. The confining pressure stability is able to maintain confining pressures up to 13.8 MPa (2000 psi) for periods of more than 20 hours leading to a significant improvement in µCT image resolution to 5 µm.

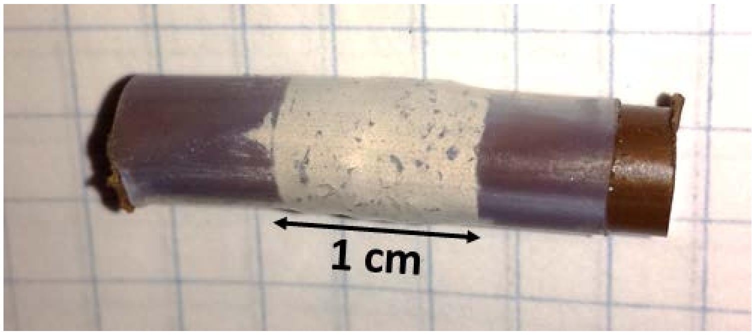

Figure 3: Sample of coarse-grained quartz sand with 30wt% bentonite between Torlon end pieces and heat-shrink jacket and artefacts in the CT images.

The sample shown in Figure 3 consists of a 1-cm long sediment pack placed between two Torlon end pieces which will later be replaced by the ultrasonic transducers. The sample was jacketed with heat-shrink tubing and clamped with steel wires on both ends. As sediment we used coarse grained quartz sand mixed with 30wt% bentonite. The sample was dry; pore pressure was not applied for these initial tests.

Our updated MXCT setup now has a set of bigger ultrasonic P-wave transducers (Figure 4) that are housed inside an aluminum cell (Figure 5) with larger inner diameter (20.6 mm) and thinner walls allowing for more space inside of the cell. The cell has been pressure tested to 5000 psi (34.5 MPa). The inner diameter of the cell allow us to measure samples with a diameter of 12.6 mm The transducers consist of piezoelectric PZT P-wave crystals with a diameter of 4 mm encased by cylindrical pieces of PEEK. The PZT crystal is backed by a mixture of tungsten and epoxy to attenuate reflections from the back of the crystal. The ground wire is attached to the side of the PZT crystal facing towards the sample and is covered with a layer of conductive epoxy. The signal wire is attached to the back of the PZT crystal and held in place by the tungsten backing. The wires are fixed with ports at the outward facing end of the transducers and soldered wires to connect to the feed-through to the ports. The small dimensions of the transducers led us to the decision to include only P-wave crystals for now. Pore fluid lines are added to both transducers. The top transducer has a stainless steel fluid line and the bottom transducer has a flexible PEEK fluid line of 20 cm length. A hole is drilled through the entire length of the PEEK housing, the diameter of the hole is larger for the last 5 mm (1 mm diameter) to fit the fluid line. The fluid line can be connected to the feed-through pore fluid line with a Swagelok fitting. The fluid line, ports and wires are protected and sealed by a layer of flexible epoxy on the outward facing side of the transducer.

Figure 4: Aluminum pressure cell for use inside CT scanner

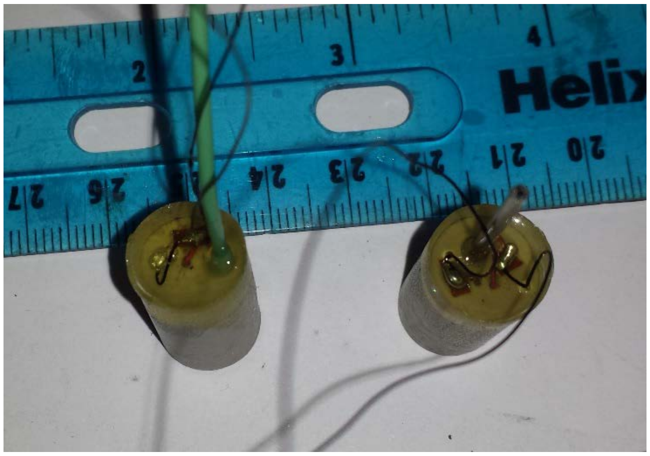

Figure 5: Ultrasonic P-wave transducers for use inside micro CT scanner.

An example for a compressional waveforms collected with the transducers is shown in Figure 6. The waveforms were collected on 19.5 mm, 47.5 mm, 67.6 mm and 102.1 mm long pieces of aluminum at 22°C and atmospheric pressure. The arrival times for all 4 aluminum pieces is shown in Figure 7 along with the dead time ($\boldsymbol{t_d = 1.58 \cdot 10^{-6} s}$). P-wave velocity for aluminum was estimated as 6452 m/s. The P-wave first arrival with amplitudes of 20 to 60 mV has sufficient signal quality to reliably pick first arrival times. The high signal quality is accomplished by changing the shape of the transducer backing that prevents back reflections.

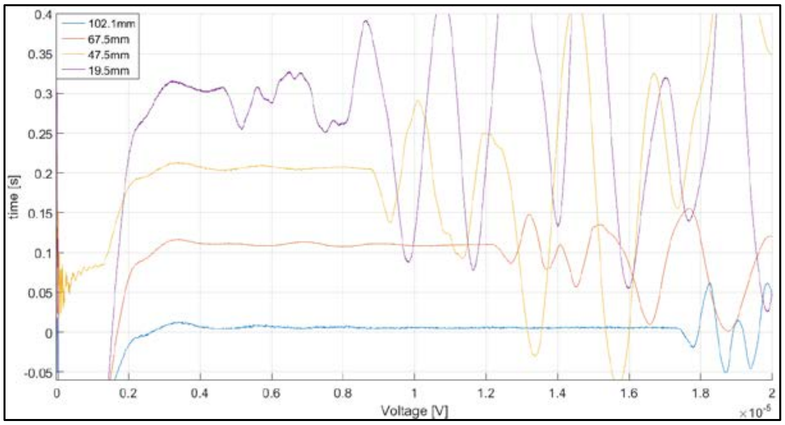

Figure 6: Waveforms for 4 pieces of aluminum – 19.5 mm, 47.6 mm, 67.5 mm and 102.1 mm long

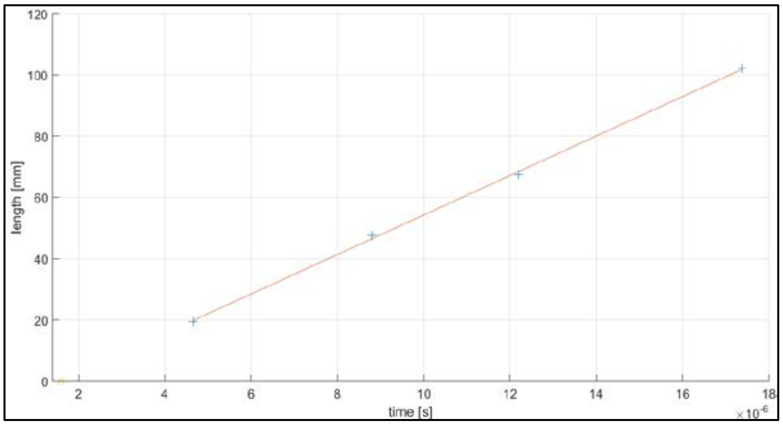

Figure 7: arrival times for all 4 aluminum pieces (blue) and dead time (yellow)

CT cooling System

To grow hydrates within the CT scanner, both temperatures and pressures need to be control to keep the environment within the hydrate stability field. Pressures are controlled by Isco digital pumps and contained within the torlon vessel (Figure 8). Our initial procedure to inflict low temperatures will consist of chilled air flow on the vessel. Other facilities have employed circulating chilled confining pressure or Peltier plates. These systems are more complex, requiring separate pumps or heat sinks, and could interfere with the motion of the scanner base. Care needed to be taken to remove any moisture from the cooling air stream. At lower temperatures, moisture would condense within the flow.

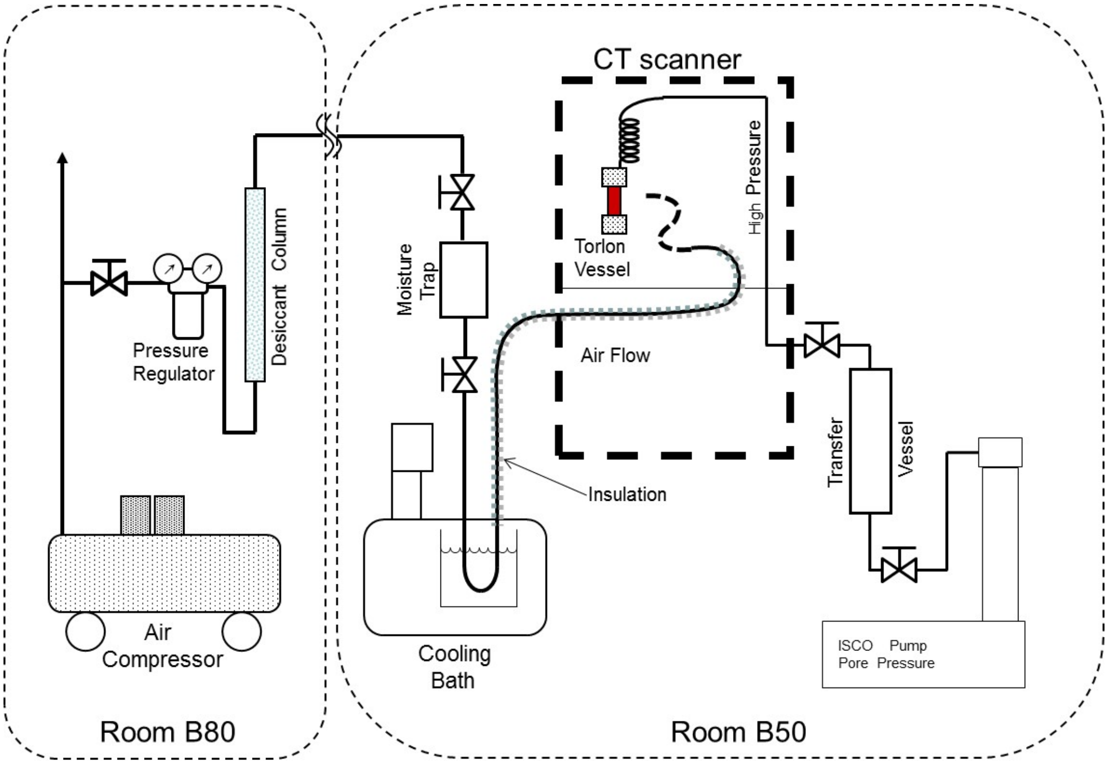

Figure 8: Schematic of the flow system to cool the Pressure vessel within the CT scanner

A calibration column consisting of F110 Ottawa sand, 1mm glass beads, and Fox Hills Sandstone was assembled to test the sensitivity of the CT scan resolution to various scanning parameters within the pressure vessel. This column is shown alongside the vessel in Figure 9 .

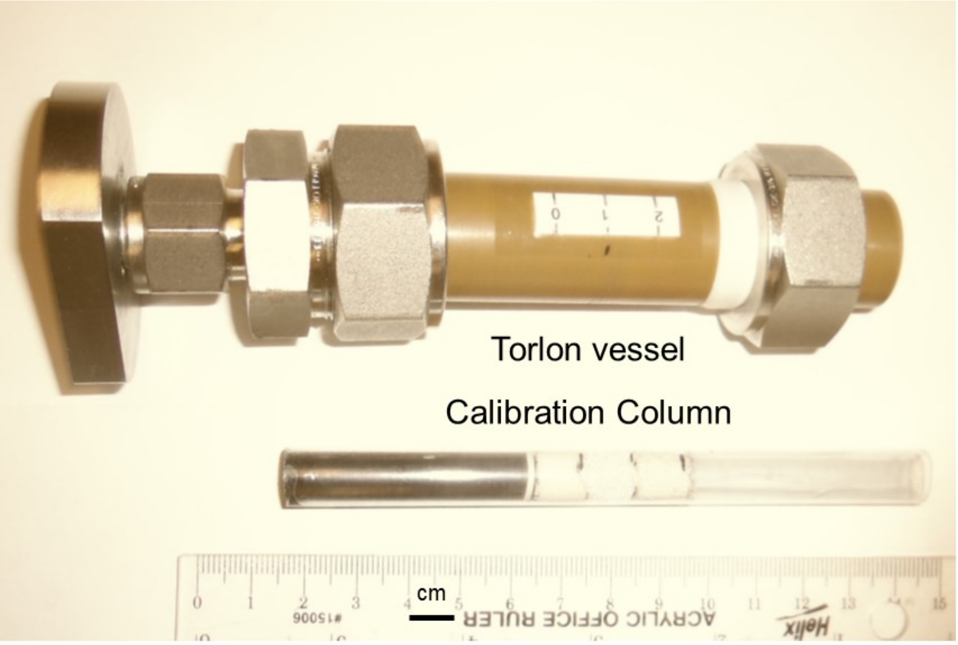

Figure 9. Calibration column outside the torlon vessel.

In Figure 10, the vessel installed in the CT scanner is seen. What is not shown is the additional thermal jacketing around the vessel. We want to keep the system as simple as possible, which justifies the air cooling system. Otherwise, electronic cables and pressure tubes still need to be attached to the vessel. These are shown at the top of Figure 10**.** These connections must not interfere with the motion of the vessel.

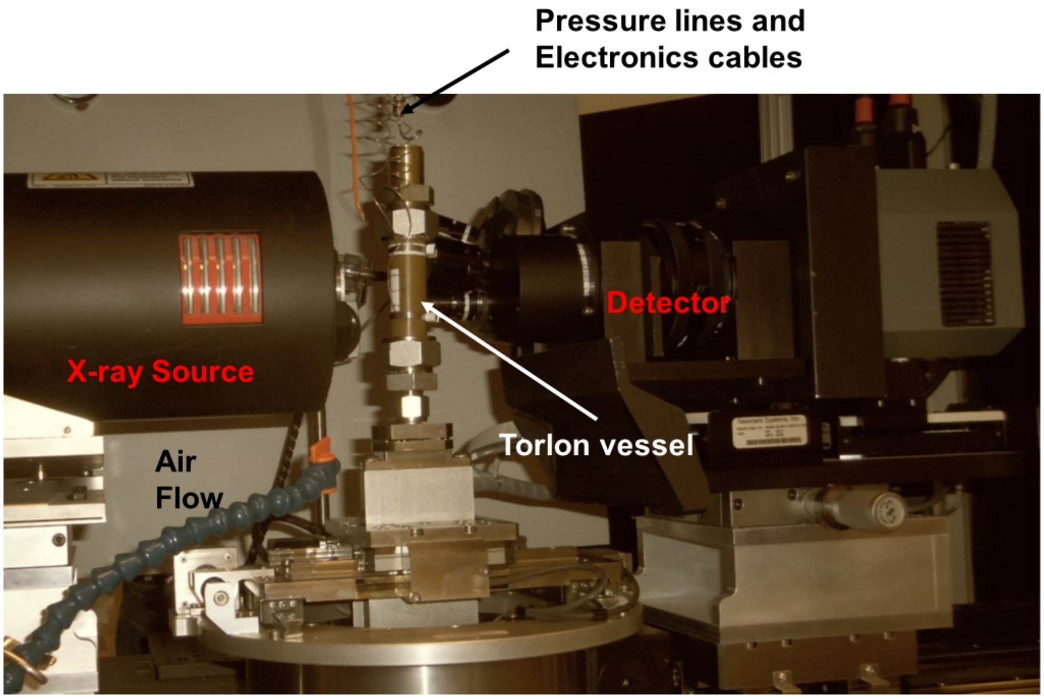

Figure 10. Pressure vessel inside CT scanner (vessel insulation removed)

Preliminary scans of the calibration column within the Torlon vessel are shown in Figure 11. Tests on other vessels we have manufactured indicate that the vessel walls can be made even thinner, without loss of pressure capability. We are now focusing on optimizing the scan parameters to optimize the resolution within the sample.

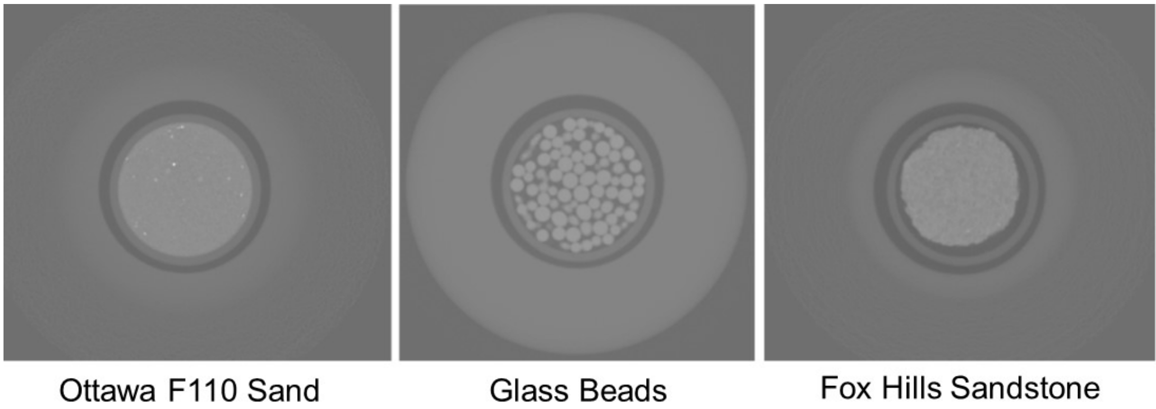

Ottawa F110 Sand

Glass Beads

Fox Hills Sandstone

Thank

you for the

Figure 11. CT scans of the calibration column materials within the torlon vessel.

MXCT Imaging – Methodology

The reconstructed images (Figure 12) contain information but for obtaining a better image quality and quantitative information from the CT images, further steps are required. Because of its low density (Table 1), THF hydrate and ice appear as low gray-value areas in the CT image whereas water with barium chloride and precipitated barium chloride show higher gray values caused by their higher density (Table 1).

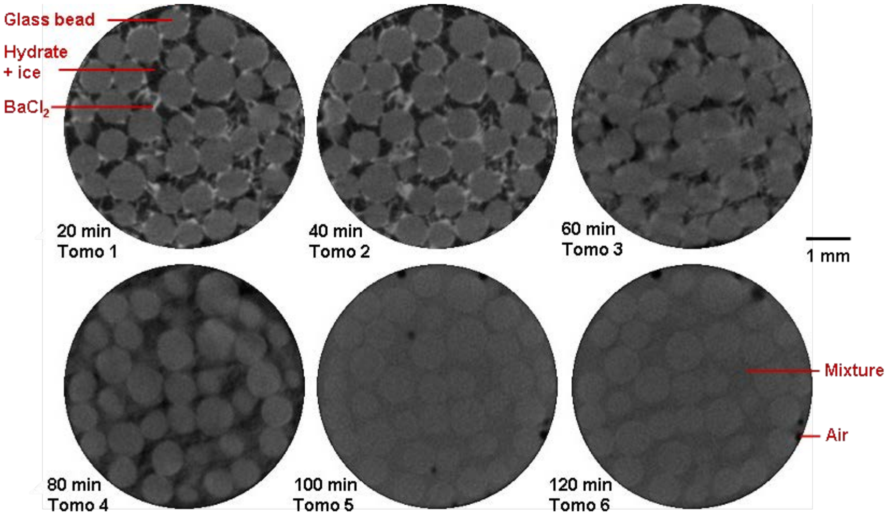

Figure 12: Series of CT images of glass bead sample with initial hydrate saturation of 80%

The gray values in the CT images depend on the density. Light gray and white areas represent substances with high density (barium chloride, water with barium chloride), dark gray areas show substances with low density (ice, THF hydrate).

Figure 12 shows a series of CT images for a sample with 80% hydrate saturation. The images capture the dissociation of THF hydrate. The first two tomographies indicate that THF hydrate and ice is arranged in the pore space and precipitated barium chloride covers the grain surfaces. During the imaging process, the ice melts and the resulting water in the pore space mixes with barium chloride.

Later in the data acquisition, THF hydrate dissociates. Dissociation and melting processes in the pore space cause the observed blurring in Tomographies 3 and 4. After the dissociation (Tomographies 5 and 6), the pore space is filled with a liquid mixture of all sample components (barium chloride, water, THF). We will refer to that as “mixture” in the following text. The mixture has an intermediate density and exhibits a medium gray value (Figure 12). Note that the dark gray circular spots in Tomographies 5 and 6 are air bubbles.

Table 1: Density of sample components for Sh=60% and 5wt% BaCl2

Sample component	Water	$BaCl_2$	$BaCl_2$ + water	THF hydrate	$BaCl_2$-water-THF mixture
Density in g/cm^3	1.00	3.84[a]	1.49	0.97[b]	1.11

[a] Lide and Frederikse, 1995

[b] Kerkar et al., 2009

For image analysis, *ImageJ* and *Matlab* were used. Image processing was used to determine which gray value in the CT images represents which substance in the sample.

Differences between the density of the components before and after dissociation are used to interpret the images. Two different images were subtracted from each other to get a gray value difference and hence a density difference. Table 1 shows the expected density values for the sample components. Density differences are negative between THF hydrate and mixture and between ice and mixture. Density differences are positive between barium chloride and mixture and between barium chloride water and mixture. Thus, images acquired before and after hydrate dissociation were subtracted to better identify the location of ice, barium chloride and THF hydrate in the images.

An *ImageJ* plugin called Mines Bilateral Filter is used to remove noise. The filter smoothes out gray scale differences below a chosen limit and preserves bigger, abrupt differences, such as the border between pore space and glass beads (Figure 13). A threshold of the gray scale value representing the glass beads is produced with *ImageJ*. This threshold is used to remove the glass beads from the image by setting their gray value to zero (Figure 13). The image subtraction was done by a *Matlab* program, which reads two images as 8-bit matrices. They are then converted into double matrices to prevent data loss during subtraction and to allow negative density differences. These two double matrices are subtracted. A *Matlab* figure showing negative (blue) and positive (red) gray value differences is created (Figure 13). Then, the differential matrix is converted back to a matrix of positive integers which is exported as an 8-bit image for further analysis in *ImageJ*.

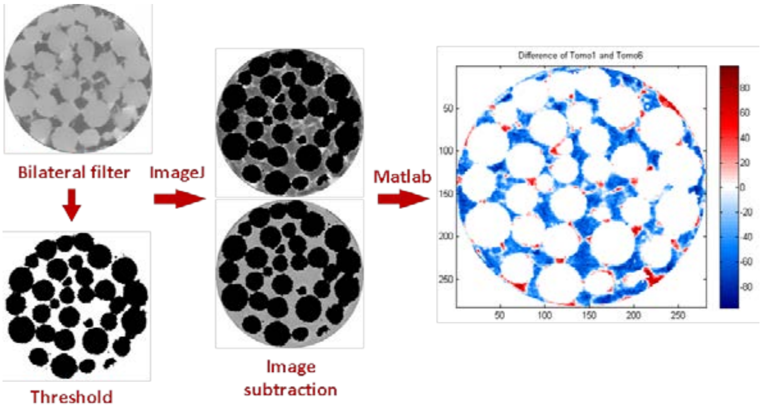

Figure 13: Image processing workflow for MXCT images

Figure 17 shows histograms and differential images referenced by subtracting Tomography 6 for a whole tomography series. The histogram median is shifting from low gray values to medium gray values over a series of tomographies. The number of pixels representing THF hydrate and ice (blue) and pure barium chloride or barium chloride brine (red) decreases. Pixels with intermediate gray values (127 ± 20) are considered either mixture or "indifferent" due to misinterpretation of pixels at the interface of high and low density areas. Figure 7 further shows that the number of pixels with intermediate gray values increases and the number of pixels with high (>147) and low (<107) gray values decreases during the scanning time. Areas of high gray value (red) and low gray value (blue) disappear due to dissociation of hydrate and melting of ice.

Preparation of MXCT Scanner for CH4 Experiments

The cooling system in the MXCT scanner is now functional and has been tested on THF-hydrate bearing glass-bead packs. Air from a compressor is led through a copper coil in a temperature bath filled with ethylene glycol with a temperature of approximately -30°C. The cooled air is then used to cool the sample inside the CT scanner. Modifications made to ensure sufficient cooling were:

1. We used compressed air instead of compressed nitrogen to cool for longer periods of time without changing gas cylinders.
2. The air hose is now paired with a hose loop flowing cooled ethylene glycol. Both hoses are insulated until they reach the sample.
3. The pressure cell containing the sample is covered with a plastic cylinder to confine to cooled air to a small volume around the pressure cell.

We managed to cool the sample with this method to approximately 2°C. This temperature is sufficient to form THF hydrates at atmospheric pressure and methane hydrate at a pressure of 8 MPa without forming ice. The pressure cell has been tested for pressures up to 34.5 MPa.

To test the functionality of the cooling system, we formed THF hydrate in a glass-bead pack and recorded MXCT images shown in Figure 14, Figure 15, and Figure 16. The temperature was kept stable for more than 30 hours.

For previous experiments, we had formed THF hydrate outside of the MXCT scanner and used dry ice for temporary cooling during the scanning process (approximately 2 hours). The longer period of stable, low temperatures allows MXCT scans at higher resolution and of better image quality (Figure 15 and Figure 16). Stable temperatures below 4°C are necessary for the formation of CH4 hydrates.

Figure 14 shows MXCT images taken at lower resolution to cover a large portion of the sample. At this scale, we observe no discrete hydrate bodies but hydrate disseminated throughout the pore space rather homogeneously. The barium chloride brine seems to fill smaller pores.

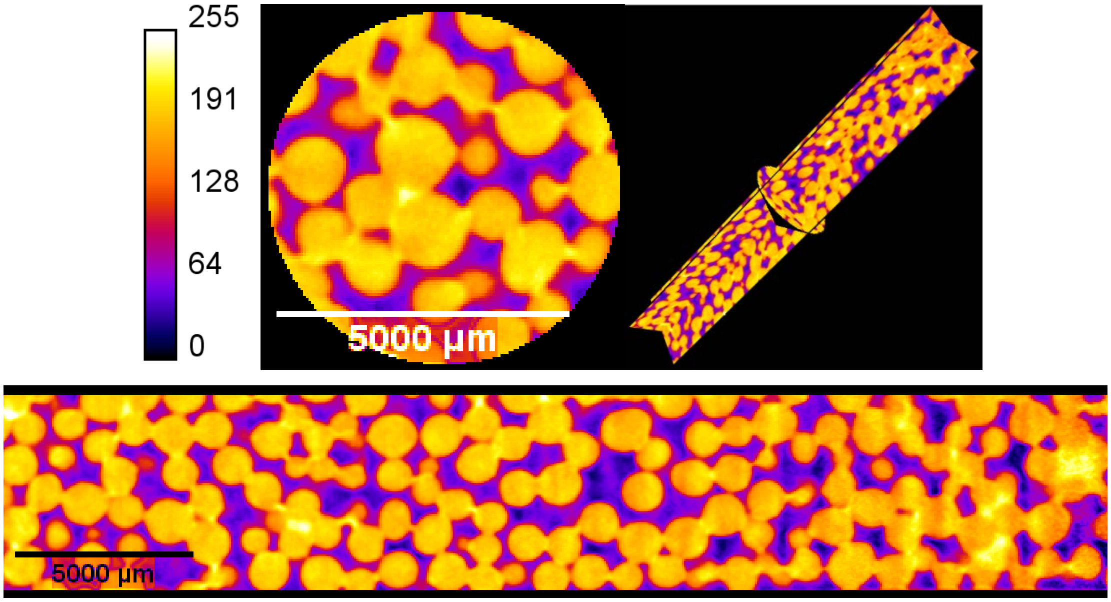

Figure 14. MXCT images of THF-hydrate bearing glass-bead pack at low resolution (1 pixel = 45.4 µm). Filename: CT_vessel_GB_THF_5. Violet: THF hydrate, light yellow: $BaCl_2$ brine, yellow/orange: glass beads.

Figure 15 and Figure 16 show high resolution MXCT images. We observed that barium chloride brine is located in small pores and along the grain surfaces while THF hydrate fills larger pore bodies. THF hydrate seems to have contact with the glass bead surfaces.

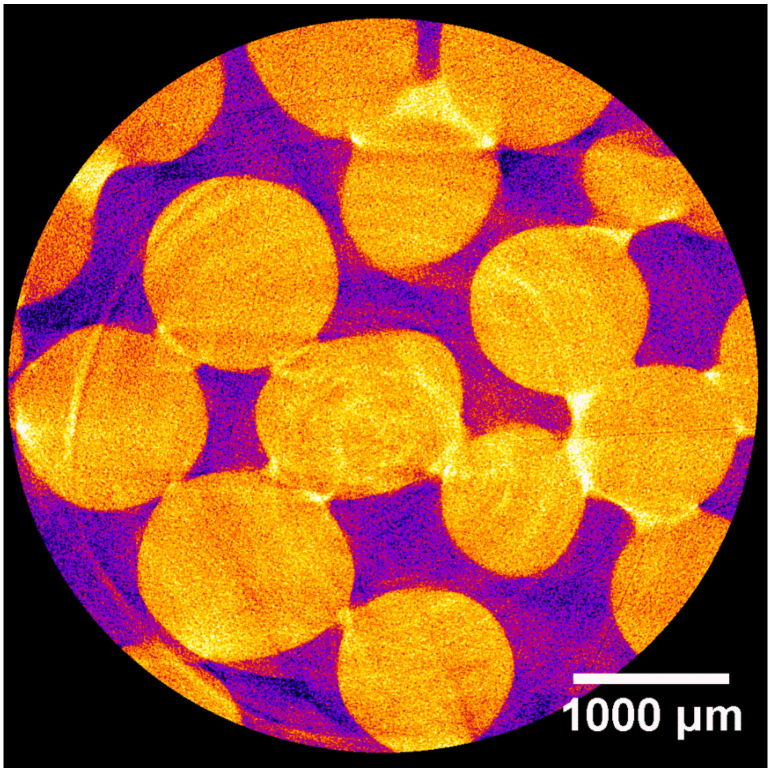

Figure 15. MXCT image at 4X resolution (1 pixel = 5 µm). Filename: CT_vessel_GB_THF_9. Violet: THF hydrate, light yellow: $BaCl_2$ brine, yellow/orange: glass beads.

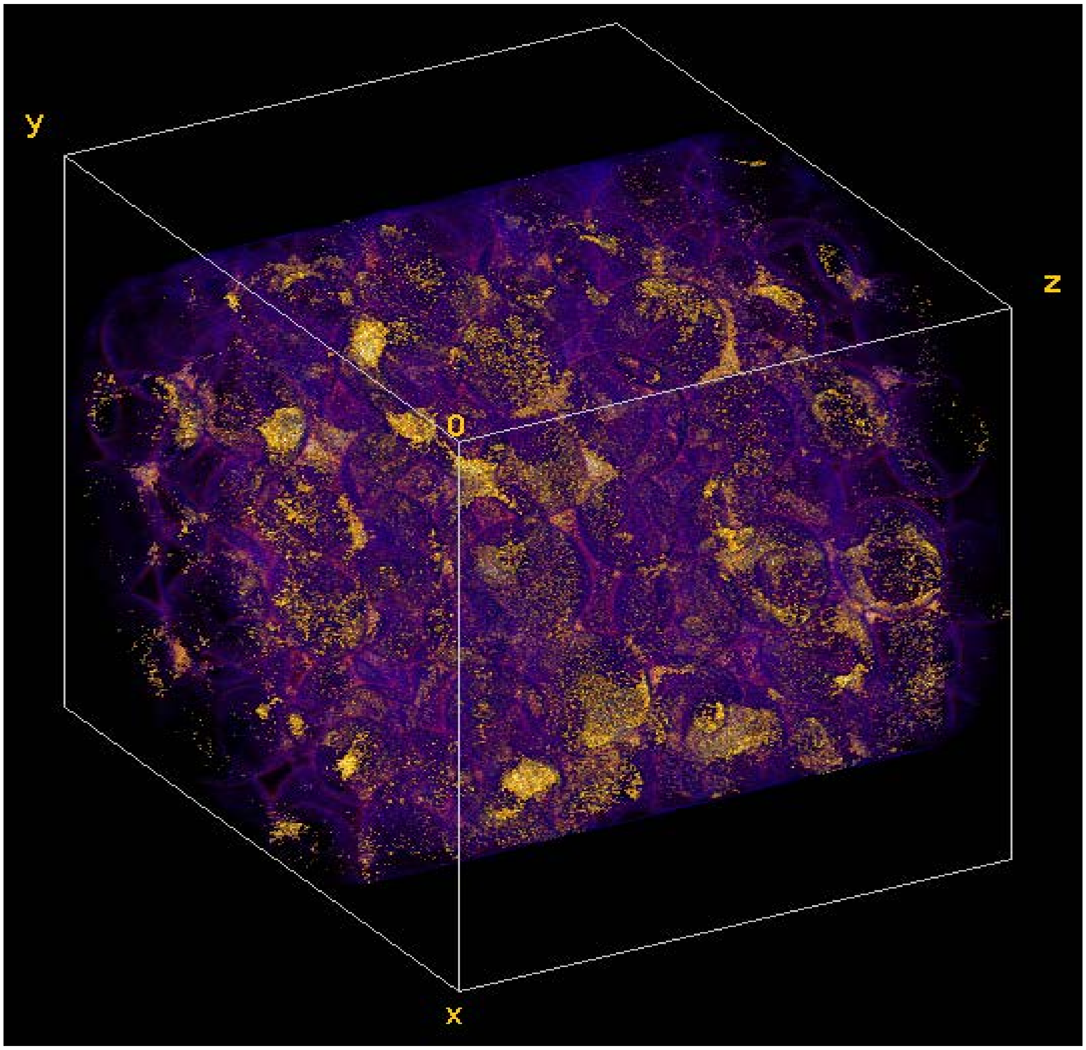

Figure 16. 3D reconstruction of a stack of tomographic images. Filename: CT_vessel_GB_THF_4. Glass beads have been cut out, $BaCl_2$ brine is shown in yellow and THF hydrate in violet.

Figure 17 shows a histogram for the three sample components: THF hydrate, glass beads and barium chloride brine. The gray values for THF hydrate and glass beads form two separate Gaussian distributions with little overlap. A smaller Gaussian distribution at the highest gray scale values represents areas filled with barium chloride brine. The overlap in gray scale for glass beads and barium chloride brine makes the distinction of these two components problematic. However, THF hydrate can be clearly distinguished from barium chloride brine and glass beads. The gray value distributions for each phase in the sample can be used to identify different materials in further MXCT images based on their gray value. Figure 18 shows the histogram of a stack of 600 MXCT images. The histogram shows the two distinct peaks for THF hydrate and glass bead. Barium chloride brine does not appear as a separate peak though due to a smaller area (lower pixel count) filled with barium chloride brine.

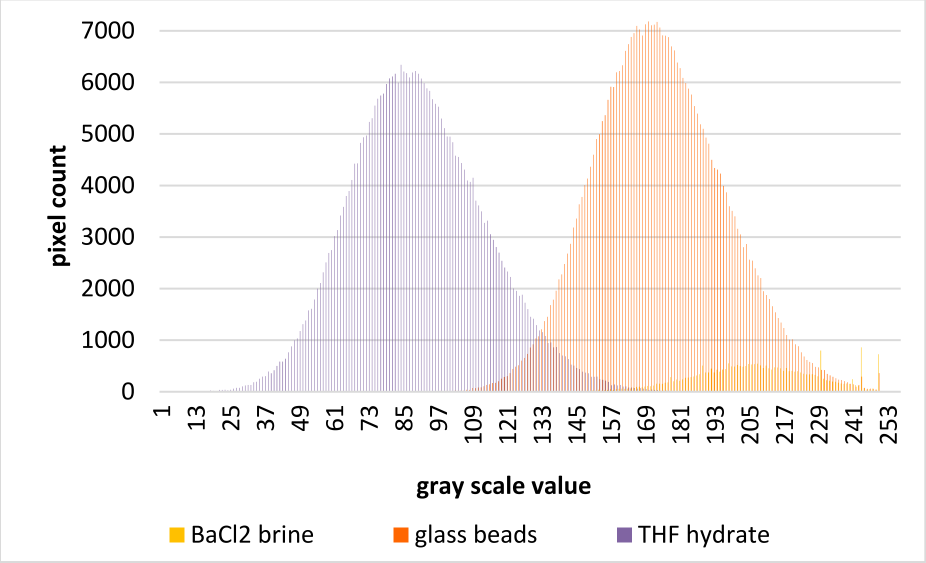

Figure 17. Histogram of representative areas of 3 sample components. THF hydrate and BaCl2 brine can be clearly distinguished based on their gray scale value in tomographic images.

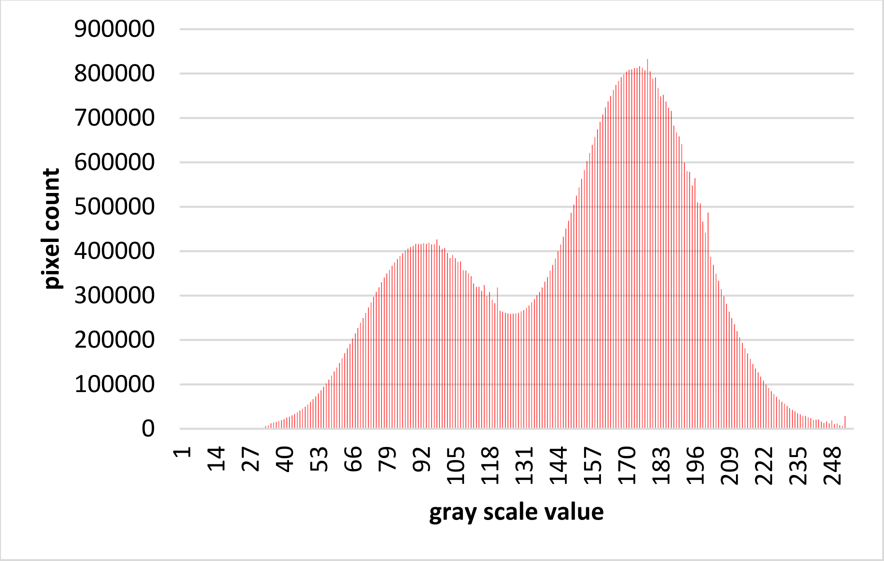

Figure 18. Histogram for entire stack of MXCT images (Filename: CT_vessel_GB_THF_9)

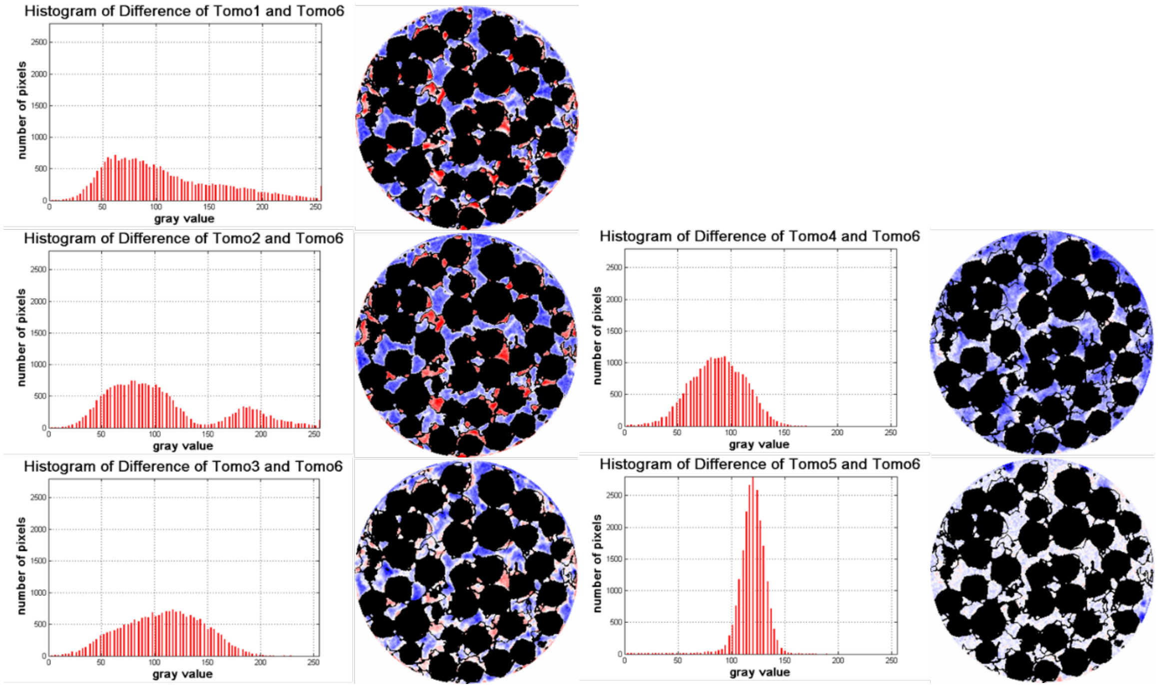

Figure 19: Histograms of gray values and differential CT images for a sample with 80% initial hydrate saturation

Figure 19 shows that the pore space appears mainly white for Tomography 5 meaning all hydrate is dissociated. The remaining blue areas in Tomography 5 are air bubbles.

MXCT Imaging of THF-Hydrate Bearing Clean Sand and Sand with Bentonite

The reconstructed µCT images of THF-hydrate bearing clean quartz sand and quartz sand with bentonite (Figure 20 and Figure 21) contain information about the distribution of different components in the sample. Different gray values in the CT images represent different X-ray attenuation values in the sample. Because of its low attenuation THF hydrate has low gray-values and appears as dark gray areas in the µCT images whereas barium chloride brine has higher gray values caused by its higher attenuation value and is displayed in light gray. The black areas in the pore space represent trapped air bubbles.

Figure 20 shows CT images for a sample with 80% hydrate saturation and the same areas of the sample at room temperature without hydrate. The images indicate that THF hydrate is located in the pore body and is interrupted by randomly shaped areas filled with barium chloride brine. The barium chloride brine appears to cover the surfaces in some areas (indicated by light gray layer on grain surface and rougher, more irregular surfaces in Figure **20**a and Figure **20**b but not in in Figure **20**c and Figure **20**d). Some small pores are entirely filled with barium chloride brine. Hydrate saturation and distribution appears homogeneous in this sample. The distribution pattern indicates that hydrate starts to grow in the pore bodies and grows towards the grains resulting in embedded areas of barium chloride brine and a layer of barium chloride brine on some of the grain surfaces. The resolution of 7.38 µm poses a limit for the interpretation of our images: the THF hydrate appears to touch the grain surfaces in some areas, however, it cannot be ruled out that there is a micro layer of barium chloride brine between the grain and the hydrate which is not resolved in our images. Such micro layers have been described by Sell et al.

(2015). Due to the higher resolution of their images (200 nm) they observed a micro layer of water between quartz grain surfaces and xenon hydrate layers.

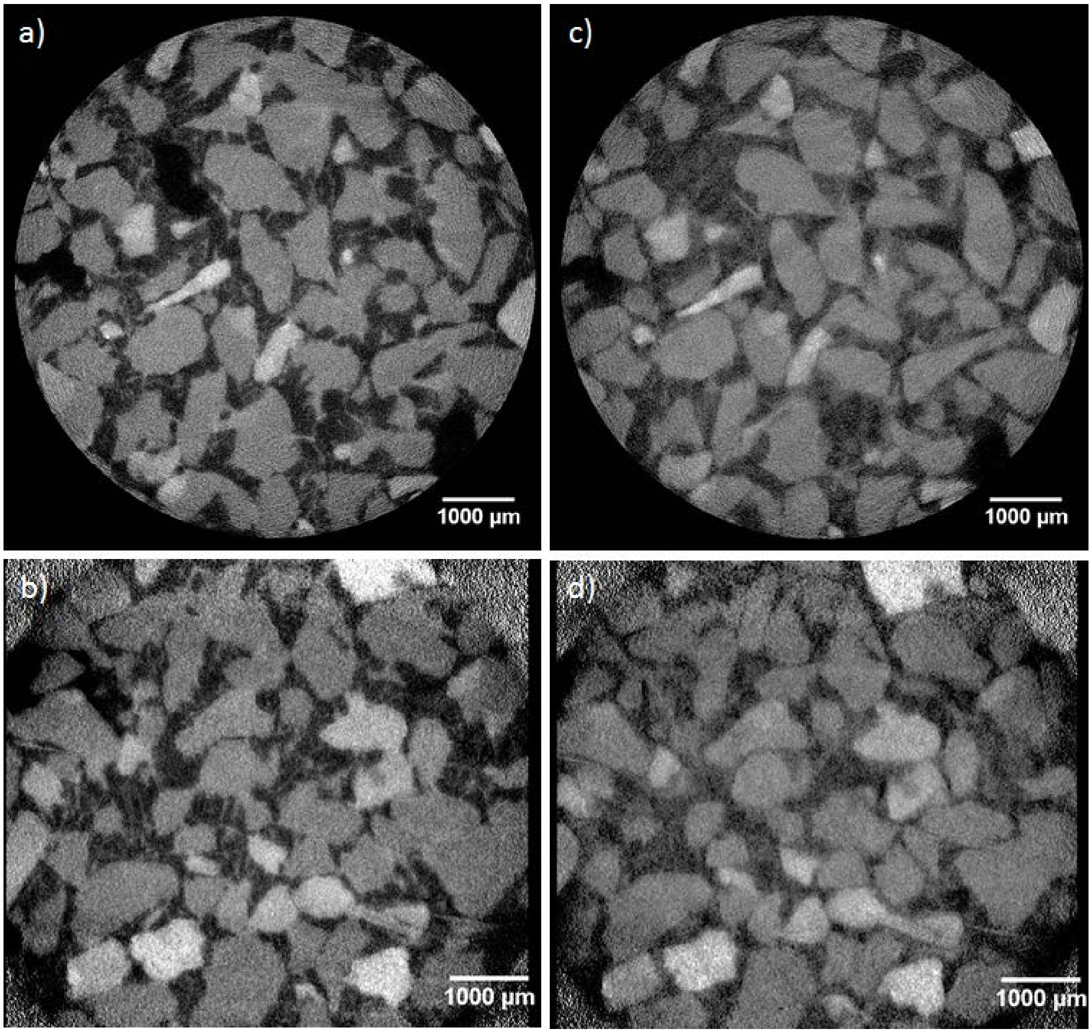

Figure 20: µCT images of horizontal and vertical slices through a quartz sand sample a) and b) at Sh=80%. c) and d) at room temperature after dissociating THF hydrate for comparison. Dark grey areas indicate hydrate, light grey areas represent barium chloride brine in the pore space. Resolution: 7.38µm

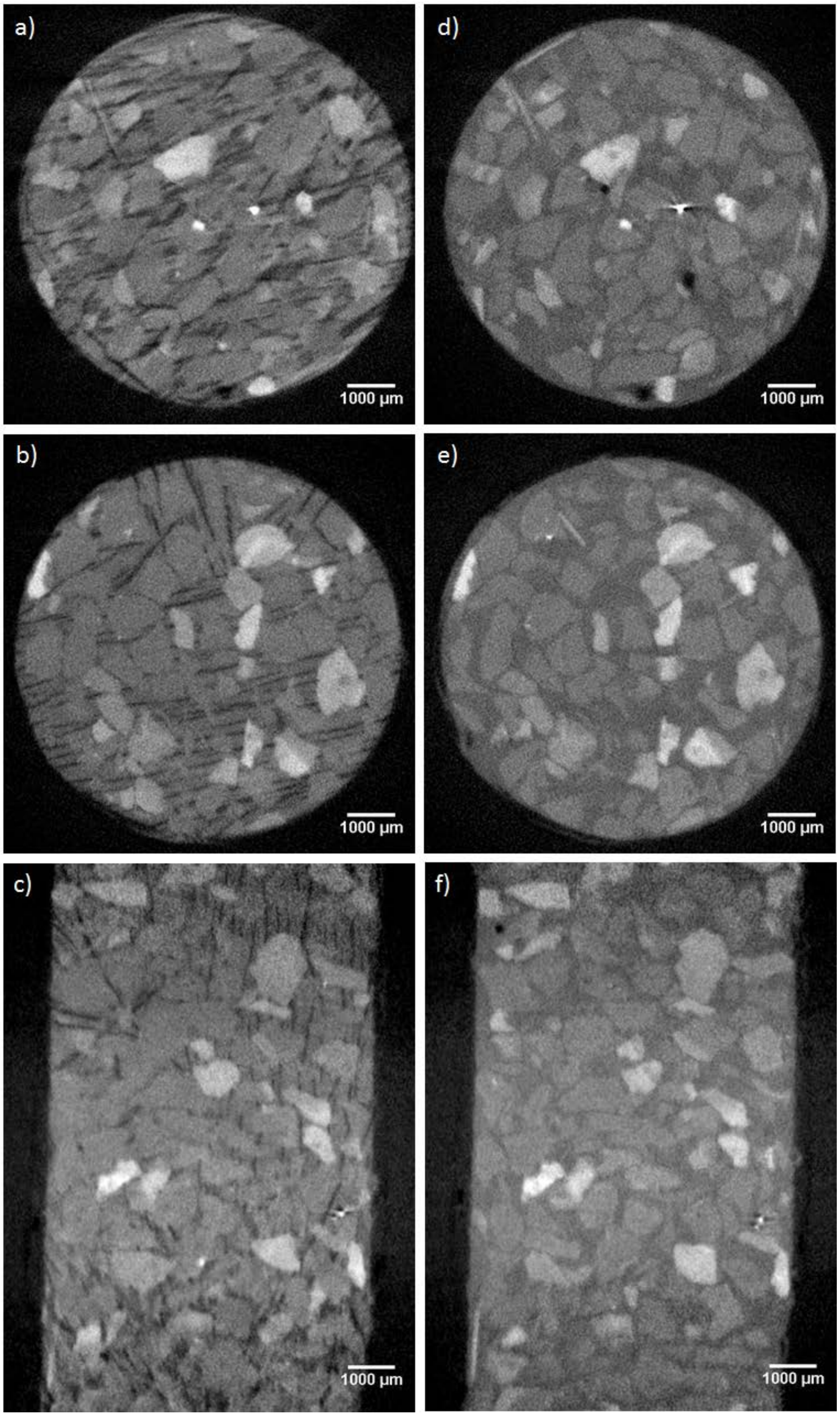

Figure 21: µCT images of horizontal and vertical slices through a quartz sand sample a), b), c) at Sh=40%. d), e), f) at room temperature after dissociating THF hydrate for comparison. Dark gray areas indicate hydrate, light gray areas represent barium chloride brine in the pore space. Resolution: 15.32 µm

Figure 21 shows a sample with 40% hydrate saturation (Images a,b and c) and at room temperature without hydrate in the pore space (images d, e and f). The hydrate distribution differs significantly from the one observed at 80% hydrate saturation (Figure **20**). Note that this sample needed to be cooled to around -1 °C and it is thus possible that ice was formed in addition to hydrate. Figure 21a and Figure 21d show slices from the top of the sample and Figure 21b and Figure 21e are slices near the bottom of the sample. We observed a more heterogeneous distribution of hydrate. The saturation seemed to vary from top to bottom of the sample and the pattern changed from a mixing of barium chloride brine (or ice) and hydrate (Figure **21**a) to discreet needle shaped inclusions of hydrate in a mainly barium chloride brine filled pore space (Figure 21b). The heterogeneity could be explained by a temperature gradient from top to bottom of the sample caused by the cooling system. The difference in hydrate distribution compared to the 80% sample indicate that the same formation method may result in different hydrate distributions and can differ from the distribution models used for effective medium modeling. Although hydrate is located in the bulk pore volume, it seems to contact the grain surfaces as well and thus cement the sediment. That means the hydrate is not strictly confirming one distribution model (the pore filling model). A mixing of hydrate suspended in the pore fluid with hydrate partially cementing the grains is possible. This behavior has been described by Fabricius (2003) as IF (isoframe) models.

Figure 22 shows a sample that contains a mixture of quartz grains and bentonite (30 wt%) as host sediment. A THF-water-BaCl2 mixture which yields 80% hydrate saturation was added. Figure 22 locally shows a similar hydrate distribution pattern as the clay free sample with 80% hydrate saturation: hydrate is located in the pore bodies, barium chloride brine covers surfaces and grows in needle-like random shapes into the pore space. The white streaks in Figure 23 show pure barium chloride precipitated when clay minerals absorbed water molecules from the barium chloride brine. A bigger area of the sample (Figure 23) shows significant heterogeneity. The left side in Figure 23a and the upper part of Figure 23b clearly show higher hydrate saturations than the right and lower part, respectively. This observation indicates that clay in the pore space is moved during hydrate formation and accumulates in some areas of the sample while other pores are deprived of clay and are almost entirely filled with hydrate. However, the clay-filled pores still seem to bear hydrate intermixed with the clays (see for example at the bottom of Figure 22a). This behavior leads to significant heterogeneity and violates the assumptions of the effective medium approach. A more complex model is required to explain changes in elastic properties caused by hydrate-clay distribution observed in this sample. The µCT images show that hydrate forms in the pores as part of the pore fluid and as cement. The presence of clay causes more heterogeneity in hydrate distribution and a mixing of hydrate and clay in the pore space. Given that THF hydrate is a proxy for one possible texture of natural occurring hydrate, we conclude that natural gas hydrate in coarse grained sediments is partially suspended in the pore fluid and partially load bearing when formed from natural gas dissolved in water. This conclusion is essential for the assessment of gas hydrate saturation from seismic and well log data

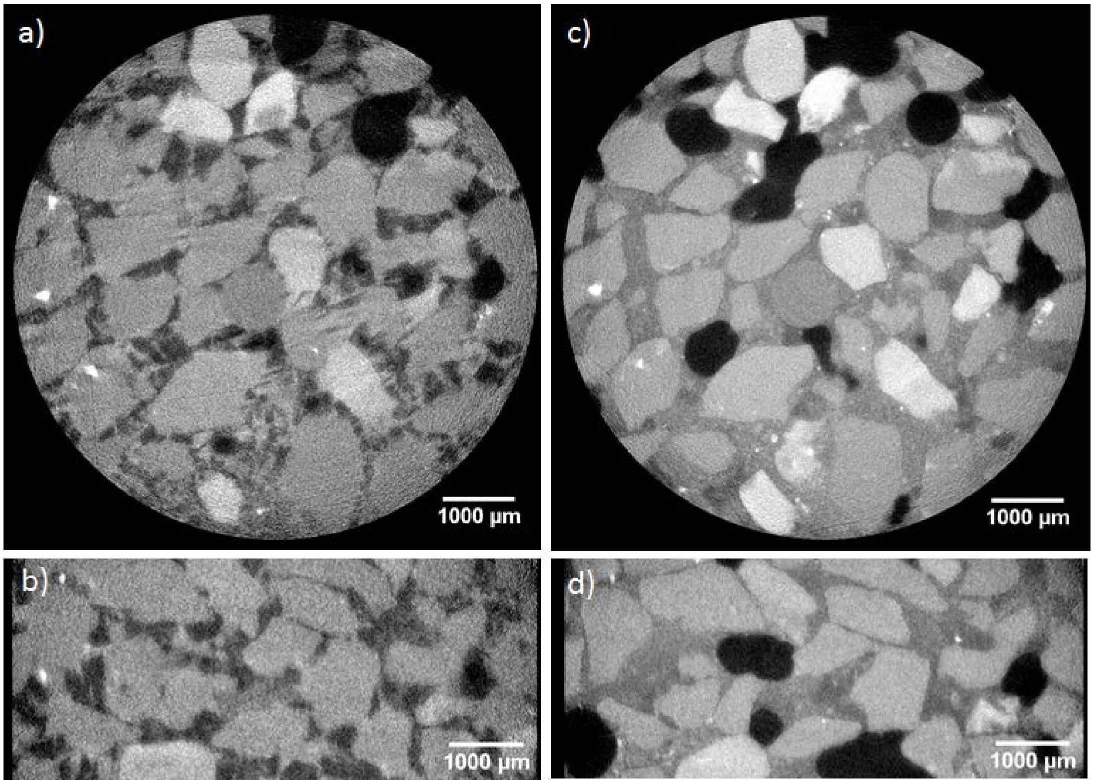

Figure 22: µCT images showing horizontal and vertical slices through a quartz sand sample with 30 wt% clay (bentonite) a) and b) with Sh=80%. c) and d) at room temperature after dissociation of THF hydrate for comparison. Dark gray areas indicate hydrate, light gray areas represent barium chloride brine and clay minerals. Resolution: 7.38 µm

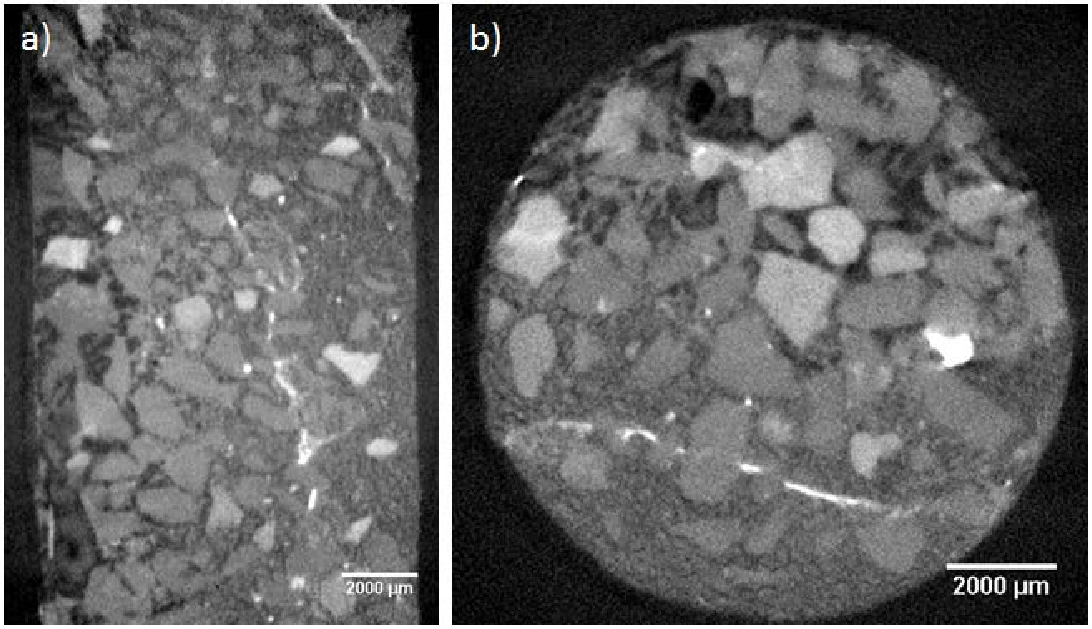

Figure 23: µCT images of quartz sand sample with 30 wt% clay (bentonite) with Sh=80%. A bigger area of the sample is shown here to emphasize the heterogeneity in hydrate distribution. Dark gray areas indicate hydrate, light gray areas represent barium chloride brine and clay minerals, white areas are precipitated barium chloride. Resolution: 20.44 µm

MXCT Imaging Sand – Clay Mixtures under Pressure

We conducted 3 cycles of confining pressure increase to 13.8 MPa (2000 psi) and subsequent decrease to atmospheric pressure. The confining pressure was increased for 16 hours before imaging and decreased back to atmospheric pressure for 8 hours prior to imaging to allow the sample to equilibrate. Multiple pressure cycles were performed to observe if the changes to the sample are reversible and whether there are further changes in a pre-compacted sample when pressurized again.

Figure 24 shows vertical and horizontal slices through the sample. For comparison, we are showing images at atmospheric pressure prior to compaction and at 13.8 MPa confining pressure. We were able to observe grain damage throughout the entire sample, especially in quartz grains that had direct contact points. Grains that were separated by pore space at atmospheric pressure appear to be crushed against each other at elevated pressure which leads to fracturing.

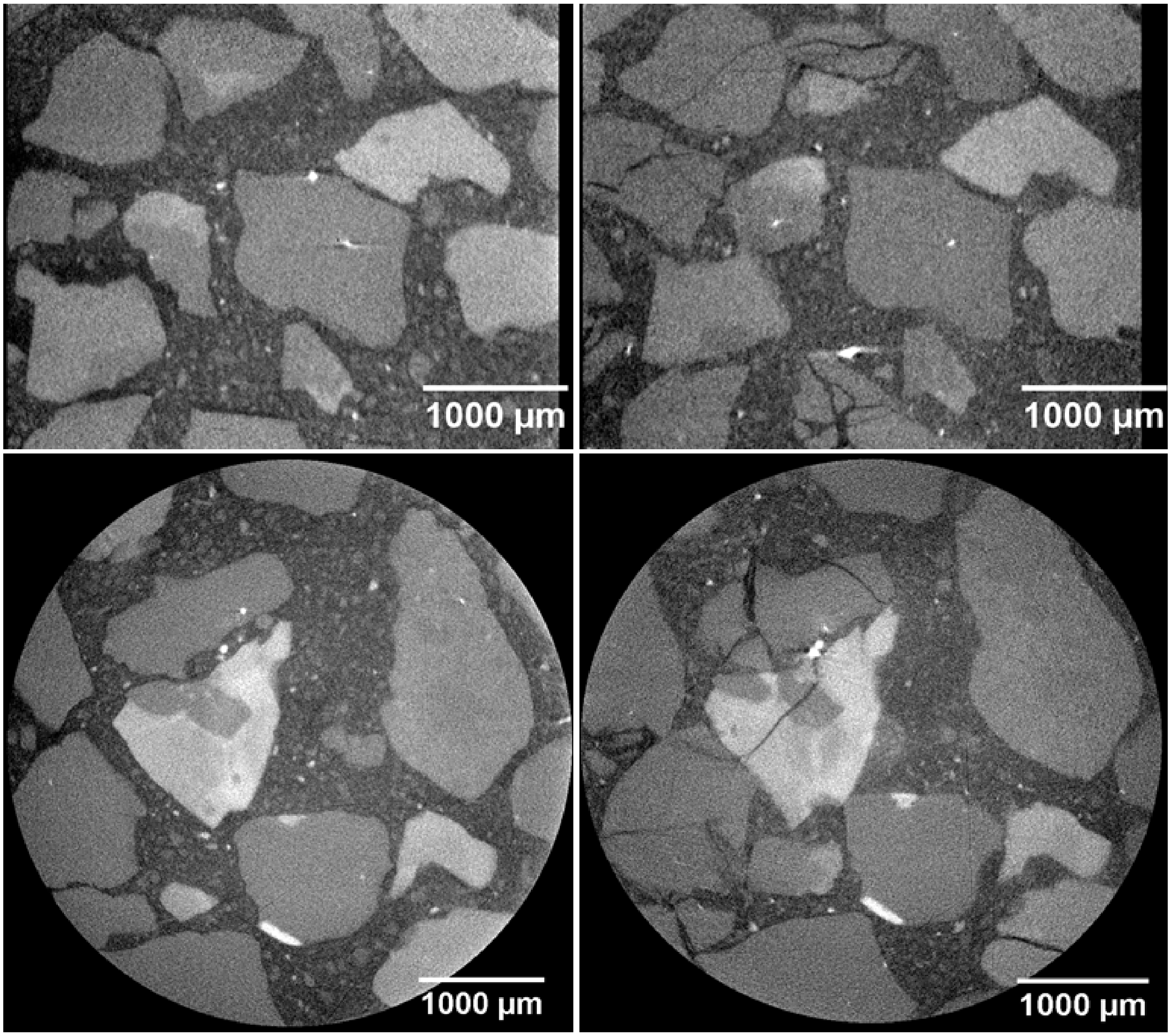

Figure 24: Vertical (top) and horizontal (bottom) slices of µCT images at atmospheric pressure (left) and 13.8 MPa (2000 psi) confining pressure (right). The images clearly show changes in the sample due to pressurization:

grain crushing with associated fracturing was observed especially where quartz grains had direct contact points without clay-filled pore space in between.

Figure 25 shows the comparison between an image taken during the first pressure cycle at 13.8 MPa and a subsequent image taken at atmospheric pressure. For some grains we observed that pre-existing fractures extended further and new fractures occurred upon decreasing the confining pressure. Some fractures also extended further upon repeated increase of confining pressure pointing to the conclusion that pre-compacted samples experience further change when subjected to increased confining pressure again.

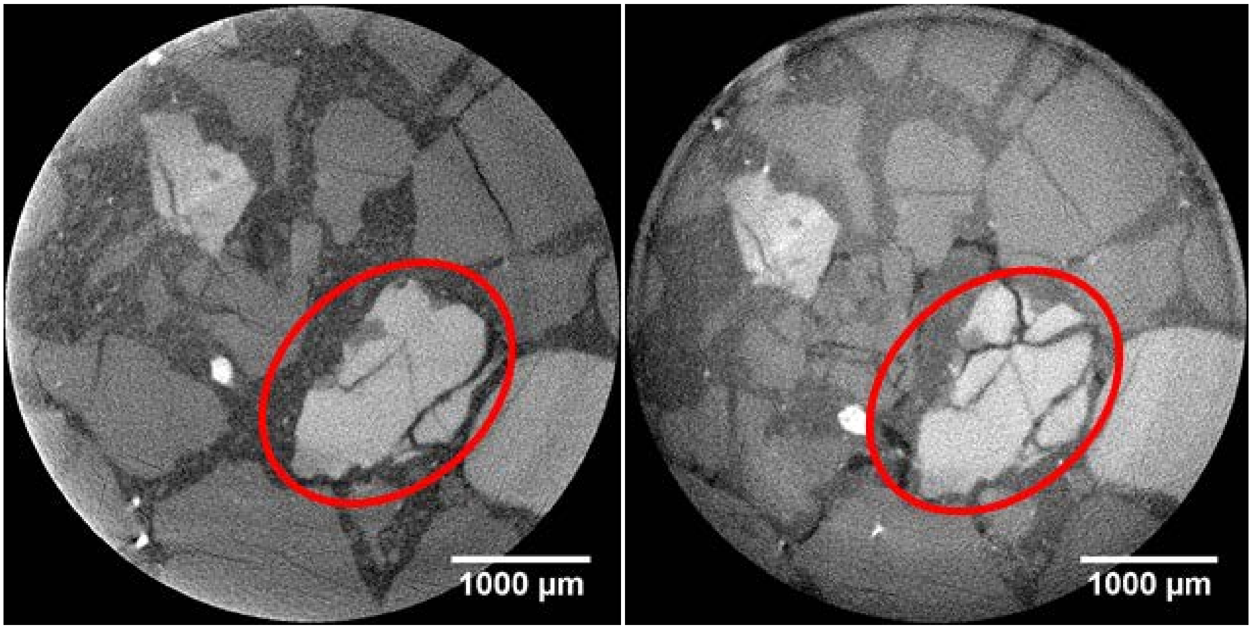

Figure 25: µCT images during first confining pressure increase to 13.8 MPa (2000 psi) (left) and after subsequent decrease to atmospheric pressure. We observe progression of existing fractures and opening of new fractures after confining pressure was decreased between subsequent pressure cycles.

Figure 26 shows images taken during the first pressure cycle at 13.8 MPa, after decreasing the pressure back to atmospheric pressure during the first cycle and after decreasing the pressure back to atmospheric pressure after the second pressure cycle. The bentonite clay in the pore space is compacted upon the application of confining pressure. When the confining pressure µCT imaging under confining is decreased, the clay stays compacted resulting in a decreased volume which leads to the formation of void spaces especially at the grain surfaces of quartz grains. This observed detachment of grains and pore filling materials could potentially lead to decreased stiffness of the sediment. Upon repeated confining pressure cycling these voids seemed to be partially closed again while new ones occurred in other areas of the sample.

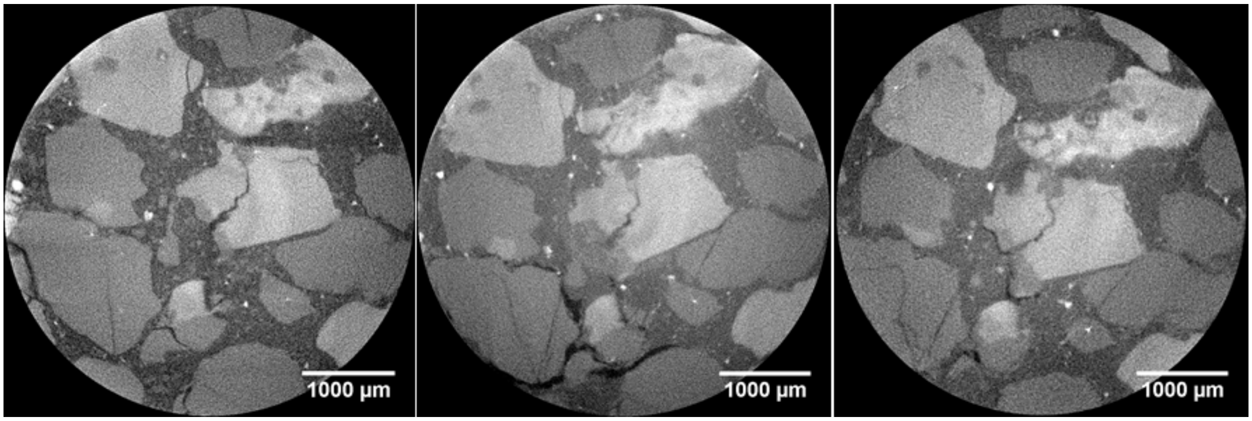

Figure 26: µCT images during first confining pressure increase to 13.8 MPa (2000 psi) (left), after subsequent decrease to atmospheric pressure (middle) and at atmospheric pressure after second confining pressure increase to 13.8 MPa (right). We observed the formation of void spaces especially at quartz grain surfaces (lower half of middle image). As the sample was confined, the clay in the pore spaces was compressed resulting in a volume reduction. The sample expands again after decreasing the confining pressure while the clay stays compacted resulting in voids in the pore space.

2. Seismic Velocity and Attenuation Measurements

Ultrasonic Velocity Experimental Methods

The basic principle of ultrasonic velocity measurements is to send an acoustic signal through the sample and measure the signals travel time through the sample. The setup of a sample with an ultrasonic transducer at each end is illustrated in Figure 27.

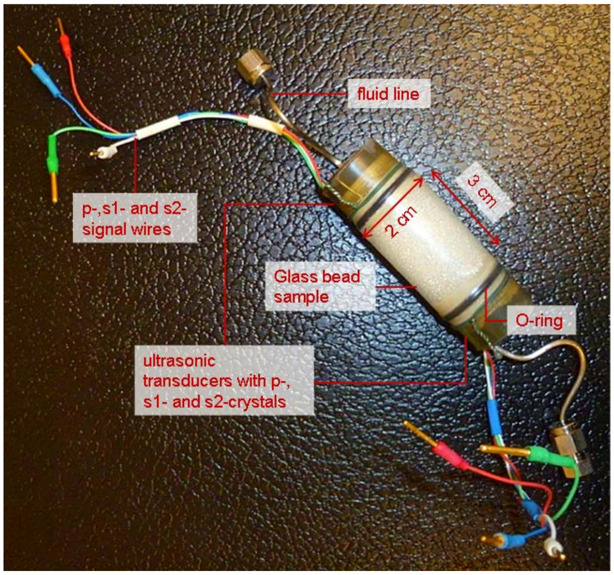

Figure 27: Sample for ultrasonic velocity measurements

The transducer contains piezoelectric lead zirconate titanate (PZT) crystals for each wave: P, S1 and S2. S1 and S2 are S-waves polarized orthogonal to each other. The signal is excited by a pulser which sends an electric impulse to the ultrasonic transducer. The electric impulse generates a mechanical strain. The mechanical strain is an ultrasonic signal with a frequency of about 1 MHz that propagates through the sample and is recorded by a transducer at the other end of the sample and then visualized on a digital phosphor oscilloscope. The samples have a total volume of 9.4 ml and are composed similarly to the ones used for MXCT measurements.

The ultrasonic experiments were performed in a pressure vessel (Figure 28). Two thermocouples recorded the temperature inside the pressure vessel but outside of the sample at its top and bottom. The pressure vessel was encased by a cooling coil connected to a cooling bath for regulating the temperature of the sample. THF-water-barium-chloride mixture was pumped in the sample at a pore pressure of 100 psi. The confining pressure was increased to 535 psi. The resulting differential pressure was 435 psi (3 MPa). Measurements were conducted on samples with THF-hydrate saturations of 40%, 60%, 80% and 100%.

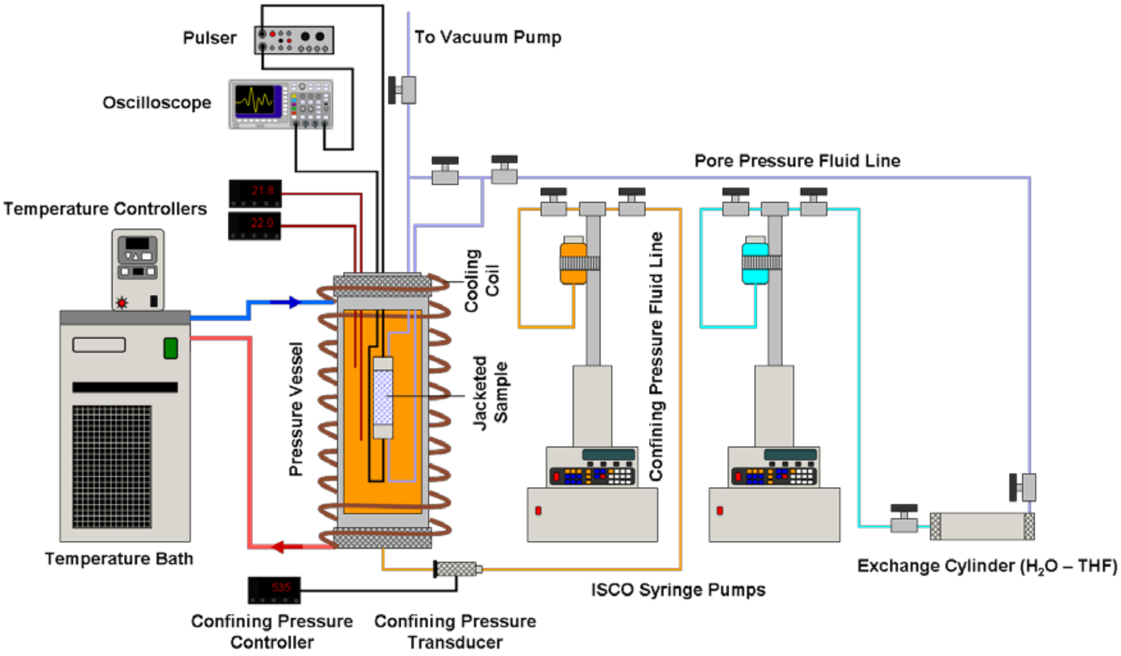

Figure 28: Experimental setup for ultrasonic velocity measurements, modified from Rydzy and Batzle, 2011

Ultrasonic Attenuation Method

The first cycle of the p-wave arrival was also analyzed for its frequency content using Fast Fourier transform. Ultrasonic attenuation was calculated with the spectral ratio method (Toksöz et al., 1978). Briefly, the amplitude spectrum of the first cycle of a waveform propagating through the sample is divided by a similar wave propagating through a standard sample. Aluminum was used as a standard material in this study. Both, the sample and the standard, were measured with the same transducers and had the same geometry. The slope of the frequency spectra ratio (Figure 29) is related to the quality factor Q (inverse of attenuation, Q^{-1}) by:

$$Q = \frac{\pi * l}{\gamma * v} \qquad (1),$$

where Q is the quality factor [unitless], l is the length of the samples [in m], γ is the slope of the frequency ratios [in s], and v is the measured velocity [in m/s].

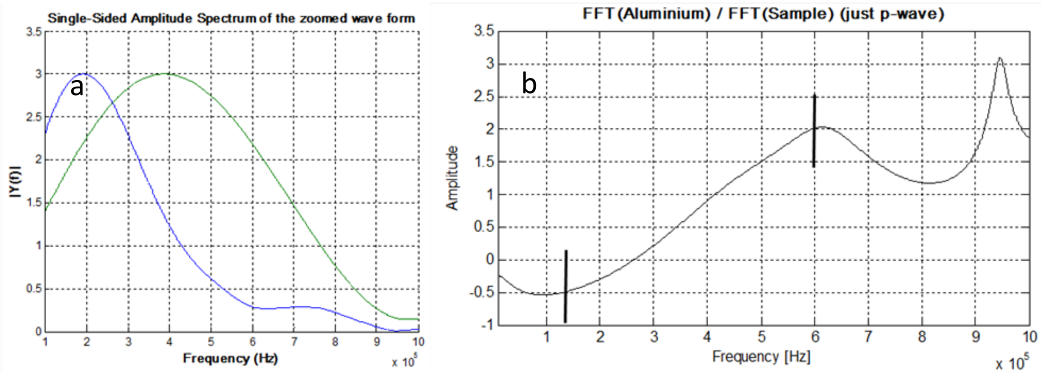

Figure 29: a) Normalized frequency content of a p-wave (blue) and aluminum standard (green), b) ratio between frequency content of aluminum and sample, the slope between the two black bars is γ.

Low-frequency System

Calibration of Low Frequency System:

The low frequency system measures the amplitude and phase of deformation of a sample using strain gages. The sample is in line with an aluminum standard and direct comparison with the aluminum eliminates much of the noise. An example of the acquired data is shown in Figure 30. For each gage pair, or channel, both amplitude and phase are measured. In reality, at each specific frequency three measurement cycles are made. The reported values are the average amplitudes and phases. Since three set of data are collected, the procedure also allows us to calculate the standard deviation (SD) of these values. This SD gives us a straight forward method to ascertain the quality of any given data point.

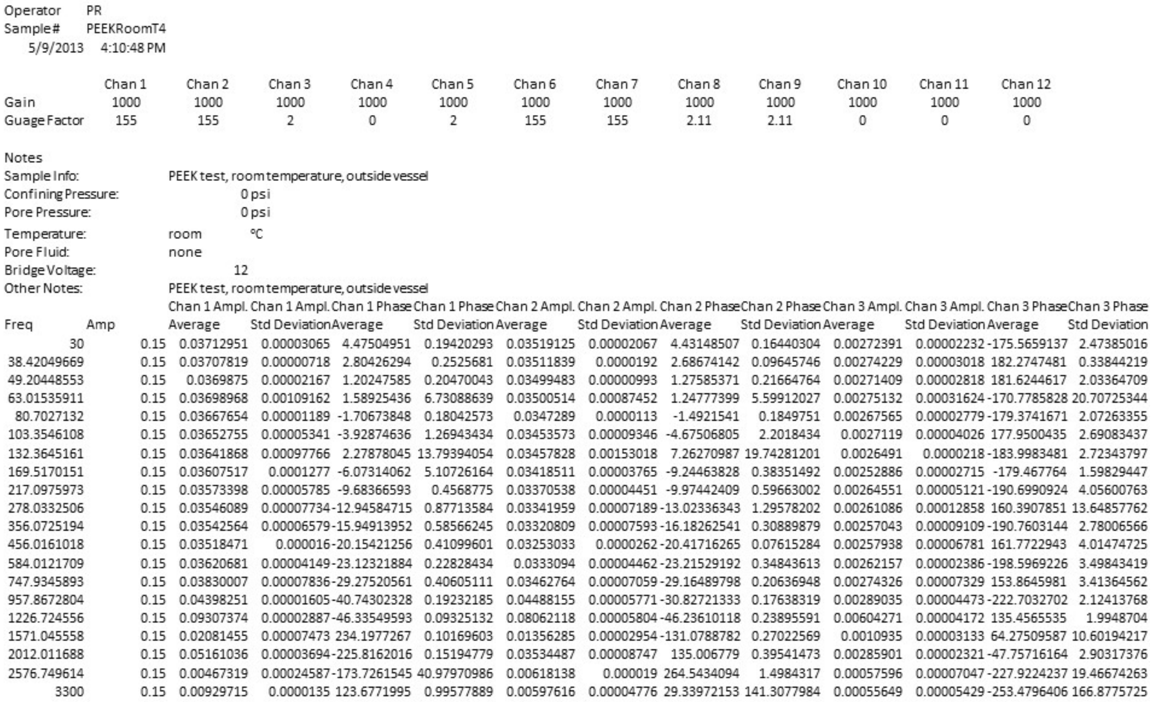

Operator PR
Sample# PEEKRoomT4
5/9/2013 4:10:48 PM

	Chan 1	Chan 2	Chan 3	Chan 4	Chan 5	Chan 6	Chan 7	Chan 8	Chan 9	Chan 10	Chan 11	Chan 12
Gain	1000	1000	1000	1000	1000	1000	1000	1000	1000	1000	1000	1000
Guage Factor	155	155	2	0	2	155	155	2.11	2.11	0	0	0

Notes
Sample Info: PEEK test, room temperature, outside vessel
Confining Pressure: 0 psi
Pore Pressure: 0 psi
Temperature: room °C
Pore Fluid: none
Bridge Voltage: 12
Other Notes: PEEK test, room temperature, outside vessel

		Chan 1 Ampl.	Chan 1 Ampl.	Chan 1 Phase	Chan 1 Phase	Chan 2 Ampl.	Chan 2 Ampl.	Chan 2 Phase	Chan 2 Phase	Chan 3 Ampl.	Chan 3 Ampl.	Chan 3 Phase	Chan 3 Phase
Freq	Amp	Average	Std Deviation	Average	Std Deviation	Average	Std Deviation	Average	Std Deviation	Average	Std Deviation	Average	Std Deviation
30	0.15	0.03712951	0.00003065	4.47504951	0.19420293	0.03519125	0.00002067	4.43148507	0.16440304	0.00272391	0.00002232	-175.5659137	2.47385016
38.42049669	0.15	0.03707819	0.00000718	2.80426294	0.2525681	0.03511839	0.0000192	2.68674142	0.09645746	0.00274229	0.00003018	182.2747481	0.33844219
49.20448553	0.15	0.0369875	0.00002167	1.20247585	0.20470043	0.03499483	0.00000993	1.27585371	0.21664764	0.00271409	0.00002818	181.6244617	2.03364709
63.01535911	0.15	0.03698968	0.00109162	1.58925436	6.73088639	0.03500514	0.00087452	1.24777399	5.59912027	0.00275132	0.00031624	-170.7785828	20.70725344
80.7027132	0.15	0.03667654	0.00001189	-1.70673848	0.18042573	0.0347289	0.0000113	-1.4921541	0.1849751	0.00267565	0.00002779	-179.3741671	2.07263355
103.3546108	0.15	0.03652755	0.00005341	-3.92874636	1.26943434	0.03453573	0.00009346	-4.67506805	2.2018434	0.0027119	0.00004026	177.9500435	2.69083437
132.3645161	0.15	0.03641868	0.00097766	2.27878045	13.79394054	0.03457828	0.00153018	7.26270987	19.74281201	0.0026491	0.0000218	-183.9983481	2.72343797
169.5170151	0.15	0.03607517	0.0001277	-6.07314062	5.10726164	0.03418511	0.00003765	-9.24463828	0.38351492	0.00252886	0.00002715	-179.467764	1.59829447
217.0975973	0.15	0.03573398	0.00005785	-9.68366593	0.4568775	0.03370538	0.00004451	-9.97442409	0.59663002	0.00264551	0.00005121	-190.6990924	4.05600763
278.0332506	0.15	0.03546089	0.00007734	-12.94584715	0.87713584	0.03341959	0.00007189	-13.02336343	1.29578202	0.00261086	0.00012858	160.3907851	13.64857762
356.0725194	0.15	0.03542564	0.00006579	-15.94913952	0.58566245	0.03320809	0.00007593	-16.18262541	0.30889879	0.00257043	0.00009109	-190.7603144	2.78006566
456.0161018	0.15	0.03518471	0.000016	-20.15421256	0.41099601	0.03253033	0.0000262	-20.41716265	0.07615284	0.00257938	0.00006781	161.7722943	4.01474725
584.0121709	0.15	0.03620681	0.00004149	-23.12321884	0.22828434	0.0333094	0.00004462	-23.21529192	0.34843613	0.00262157	0.00002386	-198.5969226	3.49843419
747.9345893	0.15	0.03830007	0.00007836	-29.27520561	0.40605111	0.03462764	0.00007059	-29.16489798	0.20636948	0.00274326	0.00007329	153.8645981	3.41364562
957.8672804	0.15	0.04398251	0.00001605	-40.74302328	0.19232185	0.04488155	0.00005771	-30.82721333	0.17638319	0.00289035	0.00004473	-222.7032702	2.12413768
1226.724556	0.15	0.09307374	0.00002887	-46.33549593	0.09325132	0.08062118	0.00005804	-46.23610118	0.23895591	0.00604271	0.00004172	135.4565535	1.9948704
1571.045558	0.15	0.02081455	0.00007473	234.1977267	0.10169603	0.01356285	0.00002954	-131.0788782	0.27022569	0.0010935	0.00003133	64.27509587	10.60194217
2012.011688	0.15	0.05161036	0.00003694	-225.8162016	0.15194779	0.03534487	0.00008747	135.006779	0.39541473	0.00285901	0.00002321	-47.75716164	2.90317376
2576.749614	0.15	0.00467319	0.00024587	-173.7261545	40.97970986	0.00618138	0.000019	264.5434094	1.4984317	0.00057596	0.00007047	-227.9224237	19.46674263
3300	0.15	0.00929715	0.0000135	123.6771995	0.99577889	0.00597616	0.00004776	29.33972153	141.3077984	0.00055649	0.00005429	-253.4796406	166.8775725

Figure 30. Example data sheet for the low frequency measurements. Note that standard deviations are collected along with the measurements of amplitude and phase.

As described previously, the experimental procedure we use is an extensional stress-strain measurement. If the assumption of isotropic, homogeneous materials is valid, then we need collect only two independent elastic parameters. In our apparatus, we do not measure displacement (as do most other experimental setups) but the strain on the sample surface. The axial strain, ε_{33}, under our boundary conditions is given by

$$\varepsilon_{33} = \frac{\partial u}{\partial x} = F \cos\left(\sqrt{\rho/E} \times \omega x\right)\sin(\omega t) , \tag{1}$$

where u is displacement, x is location, ω is frequency, ρ and E are density and Young's modulus respectively, and F is an elastic constant defined by the geometry. From the horizontal strain we can extract Poisson's ratio, ν, where the superscript '*rx*' refers to the rock value.

$$\nu^{rx} = -\frac{\varepsilon_{11}^{rx}}{\varepsilon_{33}^{rx}} . \tag{2}$$

Axial strain measurements are also made on the aluminum standard (superscript '*al*'), and the rock's Young's modulus, E^{rx} is derived from the known Young's modulus of aluminum, E^{al}, and the ratio of the aluminum to rock strain:

$$E^{rx} = E^{al} \frac{\varepsilon_{33}^{al}}{\varepsilon_{33}^{rx}} \tag{3}$$

Well-known relationships now can be used to calculate all of the remaining elastic properties for an isotopic homogeneous sample.

$$\mu = \frac{E}{2(1+\nu)} \quad .(4)$$

$$K = \frac{E}{3(1-2\nu)} \tag{5}$$

$$V_S = \sqrt{\mu/\rho} \tag{6}$$

$$V_P = \sqrt{(K + 4/3\,\mu)/\rho} \tag{7}$$

Here μ and K are the shear and bulk moduli, and Vs and Vp are the shear and compressional velocity.

In an anelastic material, the deformation will lag in time from the applied stress. For a sinusoidal applied stress, this phase lag (θ) can be described in terms of the complex modulus

$$M^* = \mathrm{Re}[M] + i\,\mathrm{Im}[M] \tag{8}$$

Then, attenuation (1/Q) can be defined as

$Q^{-1} = \mathrm{Im}[M] / \mathrm{Re}[M]$ (9)

and $\mathrm{Im}[M]\ \mathrm{Re}[M] = \tan\theta \approx \theta$. (10)

To obtain the shear-wave attenuation we use the following relation (White, 1965):

$1/Q_S \simeq [(1 + \nu) / Q_E] - \nu \tan\theta_\nu] / (1 + \nu)$ (11)

where θ_ν is the phase lag between the vertical and horizontal strain on the rock sample. Poisson's ratio at seismic frequencies is obtained from the ratio of the horizontal and vertical strain amplitude on the rock. We then estimate the P-wave and the bulk compressibility attenuation from the relations derived by Winkler and Nur (1982):

$(1 - \nu)(1 - 2\nu) / Q_P = (1 + \nu)/Q_E - 2\nu(2 - \nu) / Q_S$ (12)

$(1 - 2\nu) / Q_K = 3 / Q_E - 2(\nu + 1) / Q_S$ (13)

Errors and Noise

When the environment is noisy or the signals have small amplitude, then the errors in estimating either amplitude or phase become large. This translates into large errors in the derivation of moduli and velocities as well as attenuations. The noise depends on several factors including system shielding. The results are also frequency dependent. Figure 31 shows example results for measurements both outside and inside the large pressure vessel. On bench top, or outside the pressure vessel (black points), large noise spikes are seen, particularly at low frequencies. Much of this noise is associated with building equipment (fans, pumps) running nearby. Note also the increased noise at 120 Hz. This is not unexpected, and results from an overtone of standard power.

The good news is that we collect the data with the assembly inside the pressure vessel. This large mass of steel provides an excellent shield and filters out much of the noise. The improvement inside the vessel (blue points) is obvious. Similar observations can be made of the phase measurements. In the example shown in Figure 32, strong noise spikes are seen at 120 Hz and 240 Hz. Again, overtones of our 60 Hz power supply can be detected here.

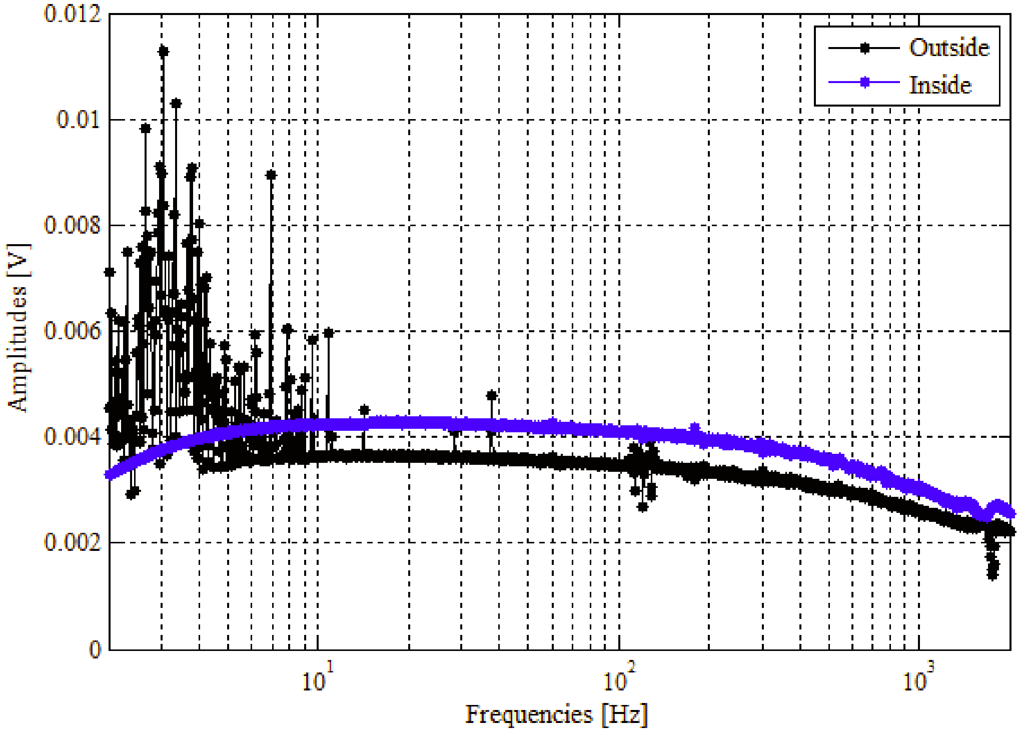

Figure 31. Amplitude of strain signals on a calibration standard collected both 'bench top' or exposed (black), and collected with the assembly inside the pressure vessel (blue). The pressure vessel provides shielding and substantially reduces noise.

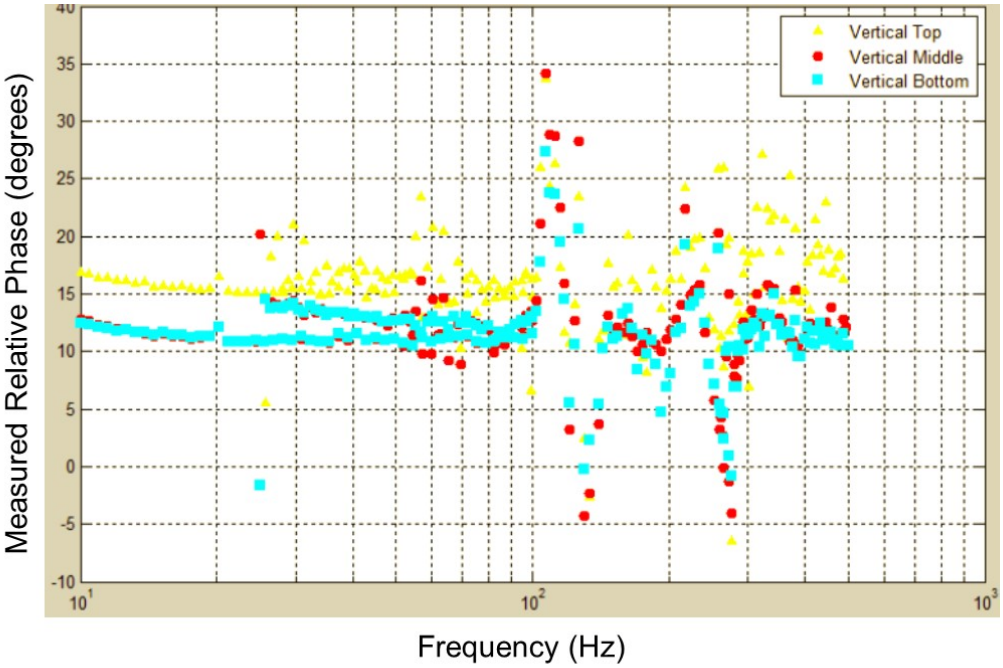

Figure 32. Phase measurements on a PEEK sample. Note the influence of noise or a system resonance at about 120 and 240 Hz (overtones of 60 Hz)

Velocity Measurements of THF hydrate bearing Ottawa Sand

We continued conducting ultrasonic velocity measurements in Ottawa Sand F110 with 60 % and 40 % THF hydrate. As we can see in Figure 33, with lower hydrate saturation the measured compressional and shear wave velocities were lower. An additional increase in velocity was observed after an increase in confining pressure to 2275 psi. After hydrate dissociation (stage 5), the velocities dropped to around the starting velocities (stage 1). An additional increase in confining pressure was performed for after hydrate dissociation (only for samples with 60% and 40% THF-water mixture). Both sets of experiments show the same increase in velocity with elevated pressures to 2275 psi.

Figure 34 shows the average compressional and shear wave ratios for all the sets of experiments. As we can see, after hydrate formation (stage 2) the ratios for the velocities decrease. This is due to the cementation caused by the hydrate and which causes a stronger increase in velocity in the shear wave. However, having a closer look we can clearly distinguish the amount of cementation based on hydrate saturation. We can observe the strongest cementation effect in the 80% hydrate saturated sample. For the 60% hydrate sample we can see an increased vp-vs ratio and an even higher vp-vs ratio for 40% hydrate saturation. This means we observed the weakest cementation effect for samples containing the lowest amount of hydrates. However, after increasing the confining pressure to 2275 psi, we can see a strong decrease in the vp-vs ratio for the 40 % and 60 % hydrate saturated samples. The change in ratio for the 80% hydrate with increased confining pressure is only minimal. This means that the sample containing 80% hydrate must be mainly supported by the hydrate matrix whereas the samples containing 40 and 60% hydrate are both, supported by the hydrate as well as grain matrix. After reducing the pressure back to 435 psi, the vp-vs ratios return to the values they were before increasing the pressure. After dissociation, the vp-vs ratios are lower than at the beginning of the experiments. This indicates a cementation process muss have occurred to the grain matrix – either due to the formation of hydrate or due to the introduced pressure cycle. Another drop in Vp-Vs ratio is seen after the dissociation and applying a pressure of 2275 psi.

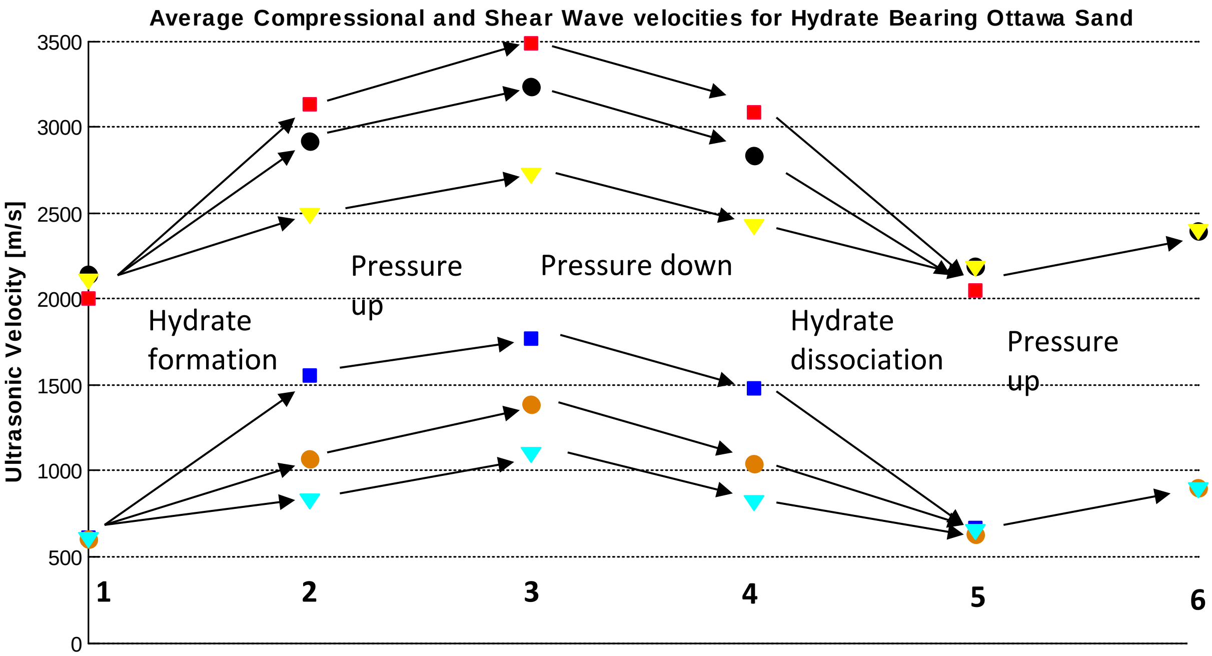

Figure 33: Average ultrasonic velocities for 80% (squares), 60% (circles), and 40% (triangles) THF hydrate bea samples. Numbers are explained in Table 2.

Table 2: Clarification for the numbers used in Figure 33.

Number	Stage	Pressure (psi)	Temperature
1	Saturated, No hydrate	435	Outside Hydrate stability
2	Hydrate	435	Within Hydrate stability
3	Hydrate	2275	Within Hydrate stability
4	Hydrate	435	Within Hydrate stability
5	Saturated, No hydrate	435	Outside Hydrate stability
6	Saturated, No hydrate	2275	Outside Hydrate stability

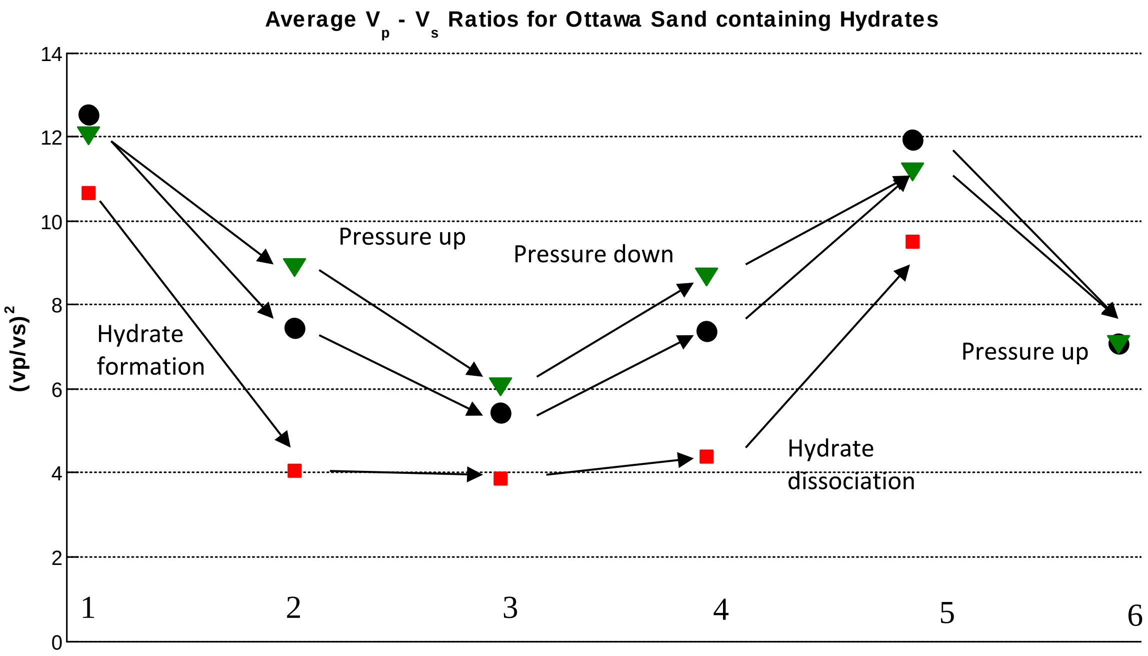

Figure 34: Average Vp-Vs ratios for 80% (squares), 60% (circles), and 40% (triangles) THF hydrate bearing samples. Numbers are explained in Table 2.

Ultrasonic Attenuation Measurements of THF Hydrate-Bearing Sand Packs

We can determine attenuation from ultrasonic waveform measurements by using the spectral ratio method. Measurements have been performed on sand packages containing pure Ottawa Sand F110 which is pure Quartz sand. Furthermore, 10 and 30 wt% of Kaolinite were mixed into the sand to investigate the influence of clay on ultrasonic velocities and attenuation. Figure 35 shows the P- and S-wave velocities measured in Sample 19 for each measurement step.

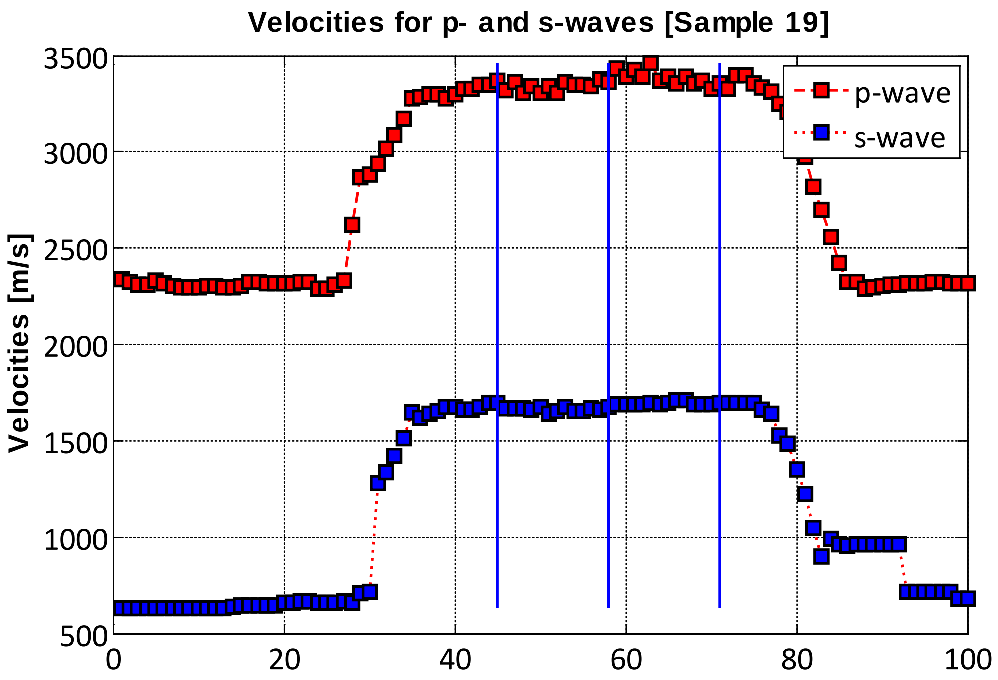

Figure 35. Shows all the calculated velocities for Sample 19. X-axis gives the successive measurement points.

Three sets of measurements were conducted for each sample - first the cooling, second a pressure cycle, and third the heating of the sample. During the cooling, the temperature was lowered so that it was suitable for hydrate formation. During the pressure cycle, the differential pressure of the sample was raised up to 2200 psi and then lowered back to 435 psi. The heating of the sample caused the dissociation of the hydrates. Figure 35 shows the calculated velocities for Sample 19. It can be seen that during the pressure cycle (between measurement points ca. 40 to about 75), the velocities stay the same. This can be explained by the fact that this specific sample had 30 %wt clay and also a low porosity (around 10 %). Additionally, the increase in velocity with hydrate formation (around measurement point 30) indicates that the hydrates are load bearing and cause the sand sample to become stiffer.

Preliminary results have been obtained for the attenuation in these samples. Figure 36 shows the first p-wave arrival for the first part of the pressure cycle (increasing pressure). As it can be seen, the waveforms shift to faster arrival times indicating a faster p-wave velocity. This pressure cycle was taken from a sample containing only quartz. Figure 37 shows the frequency spectra for the waveforms shown in Figure 36. In theory, one would expect a reduction in attenuation when the pressure increases. This can be observed in Figure 37. With increasing pressure we can see that the spectra contain more information in the higher frequencies. Nevertheless this increase in frequency content is relatively small indicating that the attenuation decreases only by a little bit with increasing pressure.

In the future it is planned to evaluate all of the data sets in regard of their p- and s-wave attenuation and to determine the influence of clay.

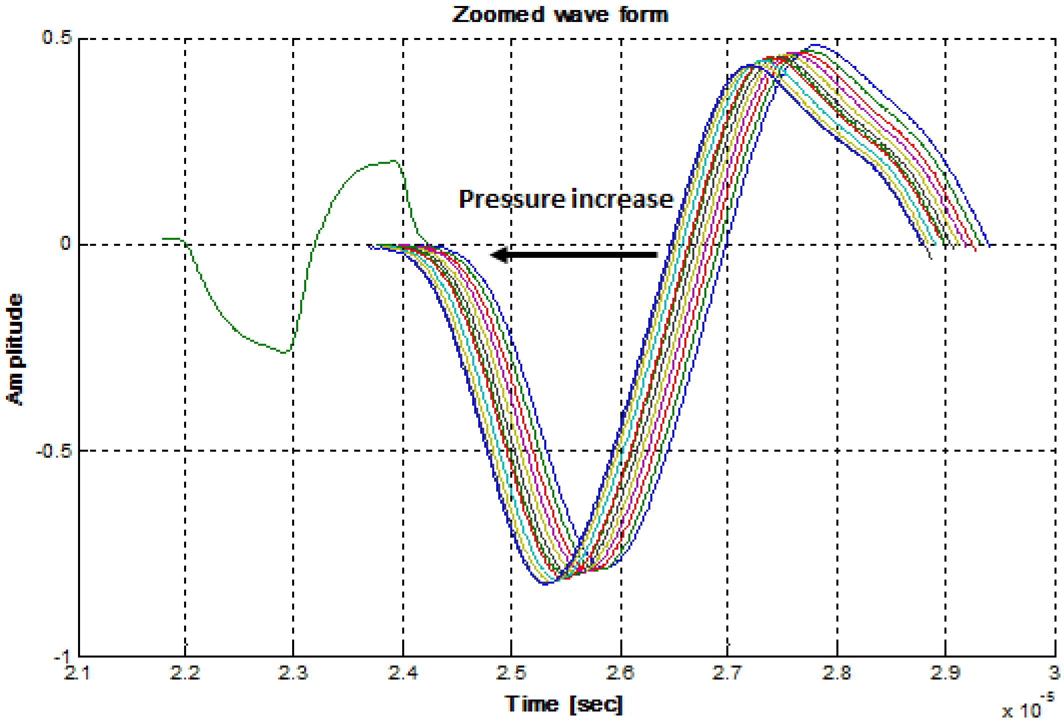

Figure 36. Frequency content of the recorded p-waves during the pressure cycle. As it can be seen, the frequency content increases as the pressure is increased.

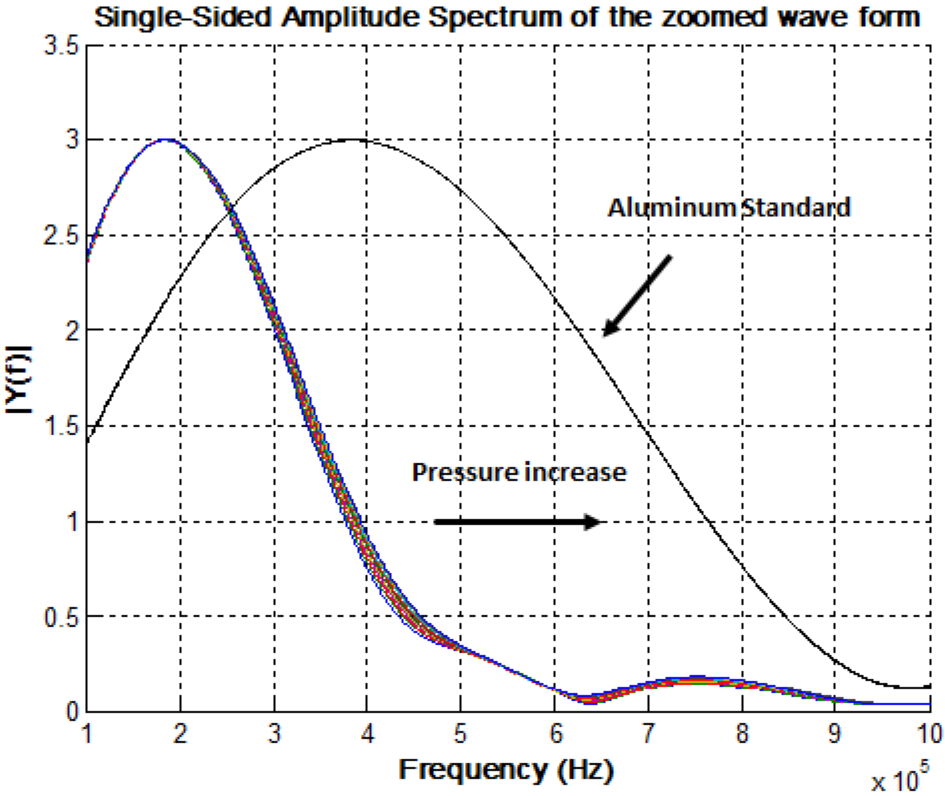

Figure 37. Change in waveforms with increasing confining pressure for a 100 % Ottawa Sand sample containing 80 % THF hydrate in the pore space. The pressure was increased from 435 psi to 2175 psi causing a shift to

the left of the waveform resulting in an increase in velocity. The green waveform on the left is the reference waveform.

We performed ultrasonic attenuation measurements on pure THF-hydrates. The goal was to determine what the attenuation of pure hydrates is in the ultrasonic frequency spectrum. Two main observations were reported: we were seeing a noticeable increase in attenuation after hydrate formation in the frequency spectrum. And after the freezing of the same sample we saw a drop in attenuation again in the frequency spectrum (Figure 38). Additionally, we were seeing an increase in the ultrasonic velocities from the liquid stage to the hydrate stage with an additional increase after the temperature was lowered to -10 °C (Figure 39). This additional increase in velocity led us to the conclusion that the conversion from THF-water to THF-hydrate was not 100 % successful. Furthermore we concluded that residual fluid in the sample was causing the observed attenuation.

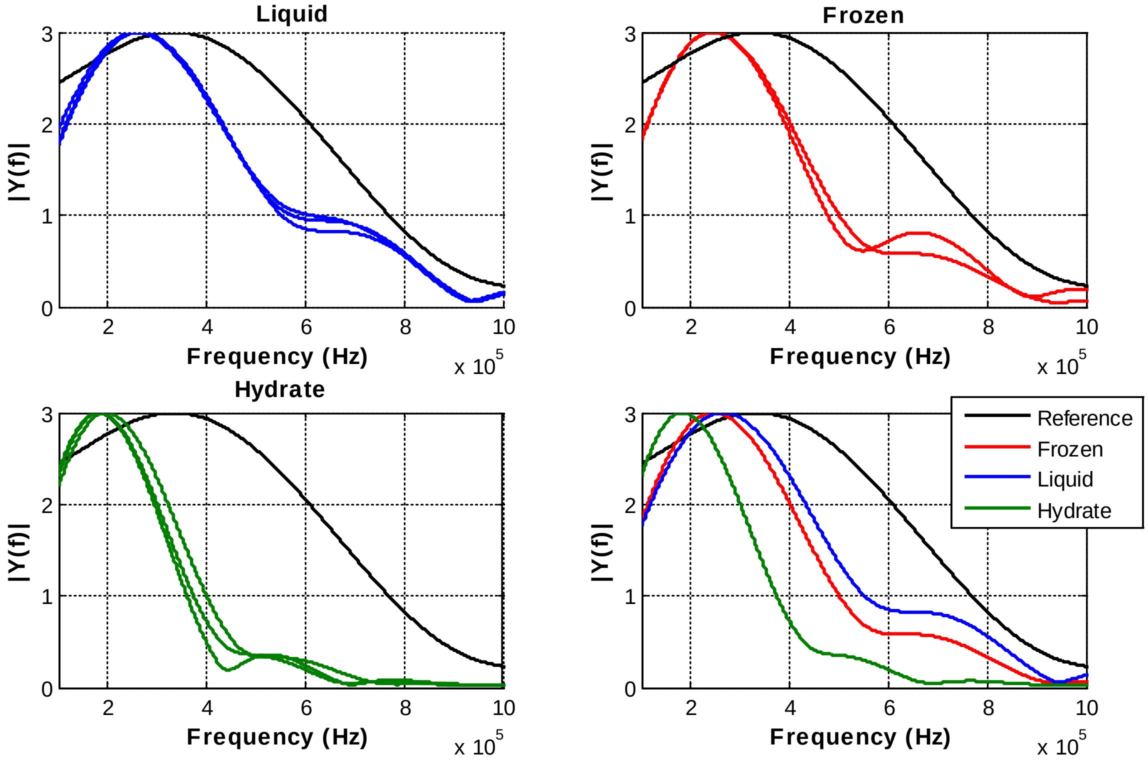

Figure 38: Frequency content of first arrivals. A) Frequency spectrum for water. B) Frequency spectrum for the "100 %" THF hydrate sample. C) Frequency spectrum for the frozen sample. D) Comparison of Liquid, Hydrate, and Frozen frequencies.

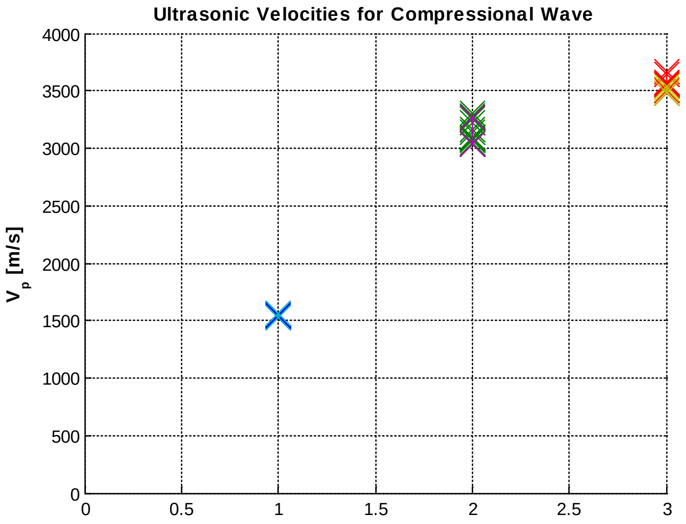

Figure 39: Measured compressional velocities for THF-water samples (Liquid), “100%” THF-hydrate (Hydrate) and the samples at -10°C (Frozen)

Ultrasonic Attenuation of Clay Filled Sand Packs before and after Hydrate Formation

Experiment set up and procedures

For sample preparation, we thoroughly mixed Ottawa Sand F110 (pure quartz sand with 60-280 µm grain size) with a designated amount (0, 10, or 30 wt.%) of kaolinite, a non-swelling clay (Krishna et al., 1993), in a plastic container until the mixture visually appeared to be homogenous. Kaolinite was chosen because it showed the least swelling effects when in contact with water. This results in a texture in which clays will be dispersed and will structurally support some of the load on the frame (see microstructural details from microCT images shown in Figure 40). 16.1 g of the sand-clay mixture was placed into an instrumented sample holder and compacted to a designated volume (2.54 cm diameter, about 2.00 cm length). Exact sample length was measured using X-ray CT scans. The instrumented sample holder was comprised of PEEK (polyether ether ketone) end caps (1-inch diameter) surrounded by Tygon tubing. The end caps contained 500 kHz piezoelectric transducers as well as fluid lines for fluid injection and pore pressure control.

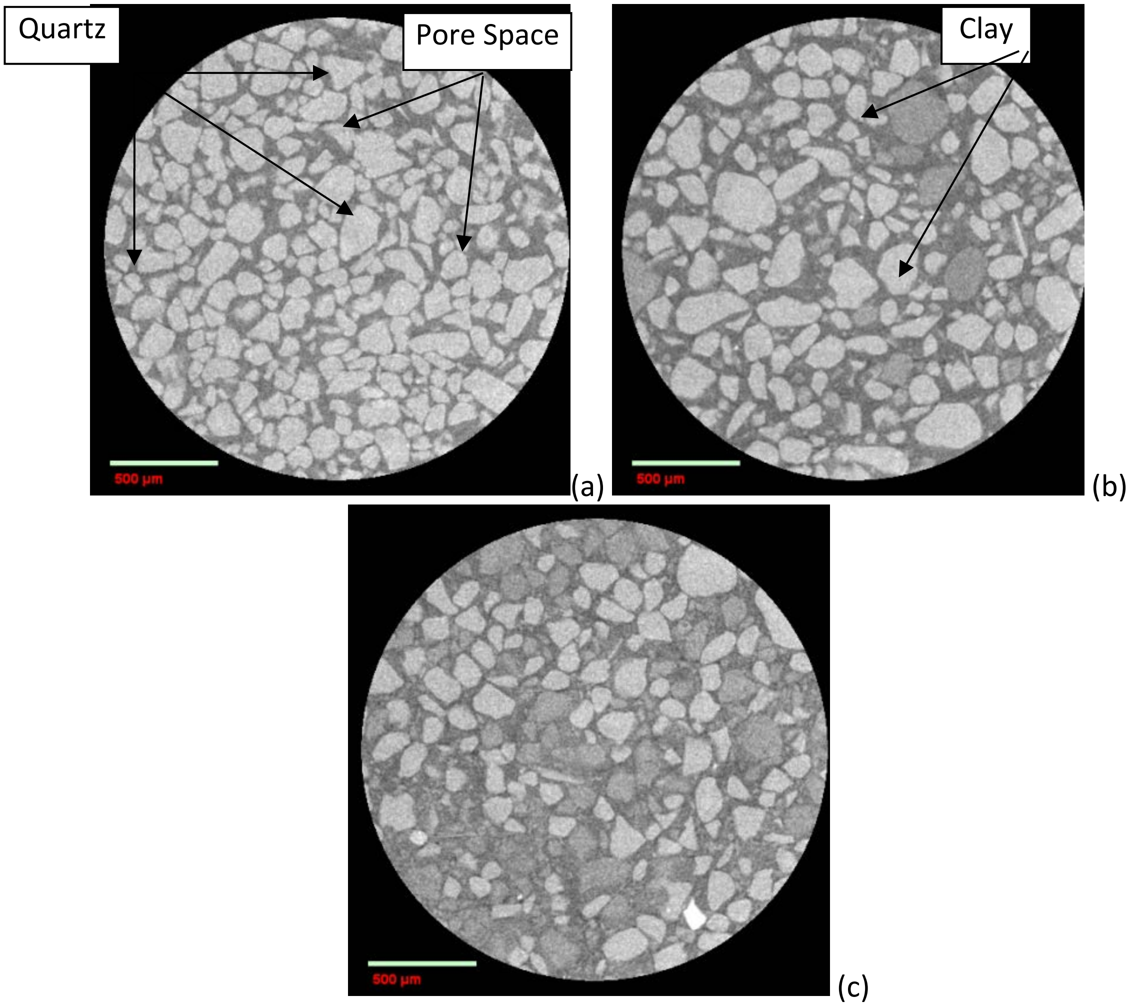

Figure 40: Micro X-Ray CT images of dry Ottawa Sand with 0 (a), 10 (b), and 30 wt% (c) kaolinite

The sample was submersed in a temperature-controlled pressure vessel filled with hydraulic oil to apply hydrostatic confining pressure. Two thermocouples were attached along the jacketed sample and recorded temperatures inside the pressure vessel. The sample was subjected to a confining pressure (Pc) of 535 psi (~ 3.7 MPa). After applying vacuum, a THF – H_2O solution, prepared to yield 80% THF hydrate with residual water, was injected into the sample. Pore pressure (Pp) was kept constant at 100 psi (~ 0.7 MPa) resulting in a differential pressure (Pd) of 435 psi (~ 3 MPa). The pressure vessel temperature was then decreased from room temperature (~ 24 °C) to ~ 1 °C at an average cooling rate of 6.5 °C/h. Ultrasonic P- and S-waves as well as temperature were recorded at regular intervals. Ultrasonic velocities were calculated by dividing the sample length by the travel time of the first break picked from each waveform after correction for the delay time through the PEEK end caps (dead time correction). P- and s-wave velocities could be determined with an error of about 3.5 %. The main source for this error was the uncertainty in picking the correct arrival time. Additionally, we calculated the porosity based on the weight and volumetric dimensions of each specimen prior to hydrate formation. For each composition, the velocities and porosity were measured in at least three samples prepared in the same way to establish degree of repeatability.

Results

Figure 41 shows the calculated attenuation values for (a) the sand packs without clay, the sand packs with 10 wt.% clay, and (c) the sand packs with 30 wt.% clay content. The 1/Qp plot in Figure 41 show a marked difference in attenuation between the original sediment (black symbols) and in the sediment after hydrate dissociation (red symbols): Attenuation is greatly reduced in the sediment after hydrate dissociation as compared to attenuation in the sand pack sample before hydrate formation. This reduction in attenuation can be explained by the compaction process that occurred during the applied pressure cycle. This compaction was also noticeable in the compressional velocities which were slightly higher after than before hydrate formation. 1/Qp increases with increasing clay content (Figure 41 b and c) before hydrate formation (black symbols) and it reaches values of around 3 for the samples with 30 wt.% clay. However, after dissociation, the attenuation values drastically reduce to values between 0.2 and 0.3. A possible explanation could be that the compliant clay particles are present as grains alongside quartz sand in the mixed samples (Figure 40). Hydrate formation is accompanied by a volumetric expansion of around 7% (Lee et al., 2007). This volumetric expansion could cause a collapse of the compliant clay aggregate grains to a denser aggregate or push the clay aggregates against the quartz grains resulting in stronger quartz – clay grain contacts.

The attenuation values for the samples containing hydrates seem to be independent of the presence of clay. However, 1/Qp and 1/Qs are observed to increase with the presence of hydrates. As we have reported in the past, the hydrate itself has only a minimal attenuation; we have also reported that small amounts of free water can cause a drastic increase in attenuation. We make the same observation in our new experiments: After forming 80 % hydrate in the available pore space, the effective porosity is being reduced to 20 % of its original value. Additionally, the pore throat size is also being reduced and, in some cases, being potentially plugged. This could cause an increase in attenuation due to squirt flow as well as attenuation caused by scattering from pores that might be isolated and contain residual water.

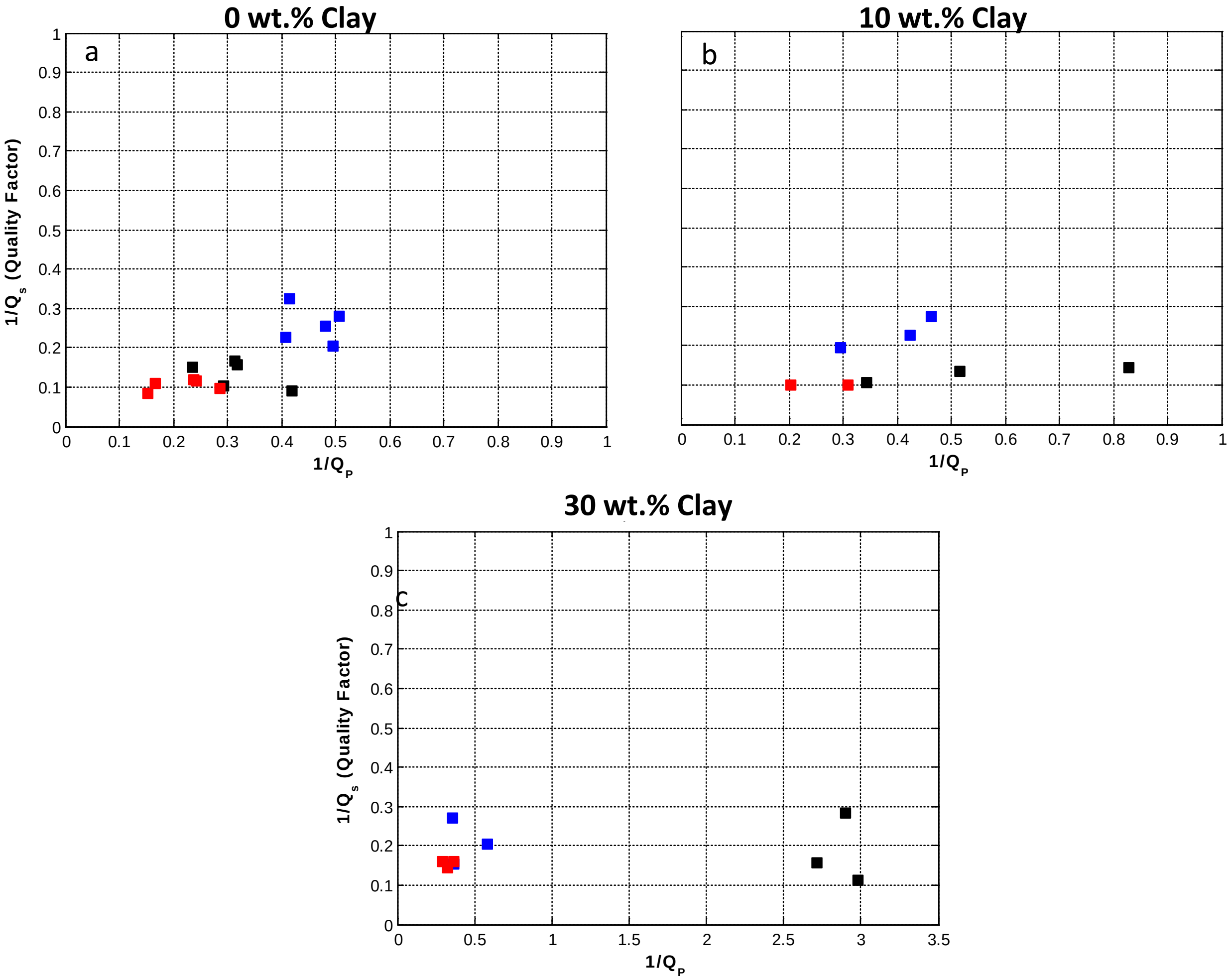

Figure 41: 1/Qs vs. 1/Qp for sand packs with 0 wt.% clay (a), 10 wt.% clay (b), and 30 wt.% clay (c). Black symbols are attenuation values before hydrate formation, Blue symbols are attenuation values with hydrates present in the sample, and Red symbols are attenuation values after hydrates were dissociated.

Loss Diagram for Sand and Sand – Clay Mixtures

We compared ultrasonic velocity measurements of Ottawa sand with 80 % THF hydrate saturation with changing clay content. For samples containing 80% hydrate the data plotted in an area which corresponded to sand samples that were measured under dry conditions. A compilation of data from Priest et al. (2006) and Guerin and Goldberg (2006) allowed us to construct a loss diagram (Figure 42) comparing two different methods to form methane hydrates – excess gas and excess water. Hydrates form along grain surfaces in the excess gas method (Figure 42 – black dots) and lead to a noticeable increase in velocity at low hydrate saturations. The excess water method (Figure 42 – green dots) forms hydrates in the pore space. Here, higher amounts of hydrate are required to increase velocities. With increasing hydrate saturation, the Vp-Vs ratio decreases for the excess water method. However, this decrease occurs at hydrate saturation of above 30 %. For the excess gas method, hydrate saturations of only 3 % cause Vp-Vs ratio to reach ~5, which changes a only little with increasing hydrate saturation. Two data points are not following the observed trend and show higher Qp-Qs ratios – these two data points fall within the area of well log data from Guerin and Goldberg.

Figure 43 shows agreement in the loss diagram between data from Priest et al. (2006) and from this study; reducing the hydrate saturation leads to increase in Vp-Vs ratios. THF and methane hydrates formed with the excess water method show similarities (Figure 43). Lower hydrate saturations change Vp-Vs ratio only a little while higher hydrate saturations decrease vp-vs ratios significantly. Increasing confining pressure to 2275 psi causes the Vp-Vs ratio for 60% and 40% to reduce even more; as also observed by Prasad (1991). Most likely, this increase in confining pressure decreases the Vp-Vs ratio due to compaction. We now calculate Qp and Qs values for our experiments to provide absolute values instead of the bars seen in Figure 43.

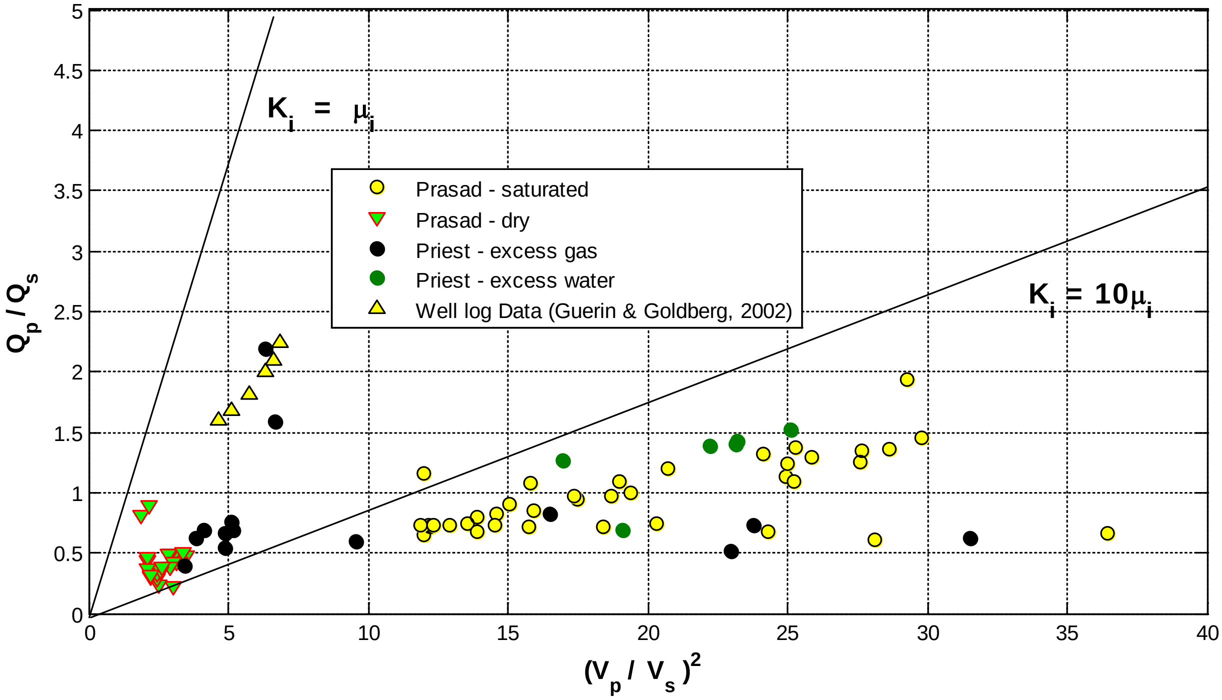

Figure 42: Loss diagram with data provided from Priest as well as well log data from Guerin & Goldberg

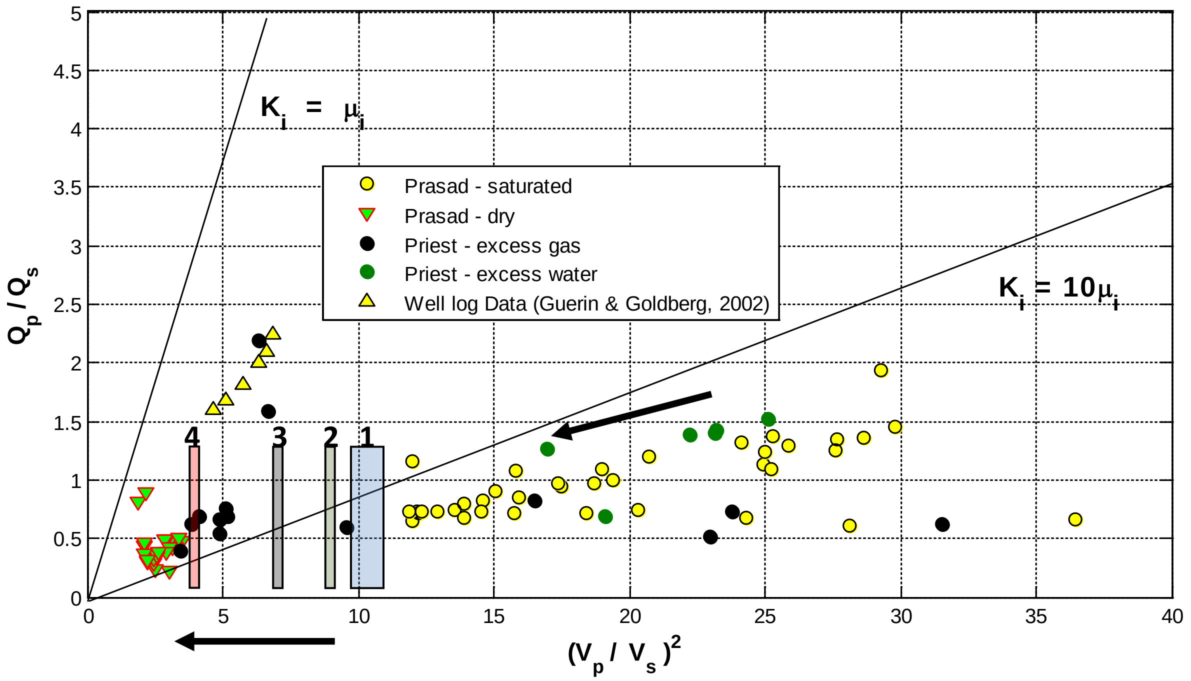

Figure 43: Loss Diagram with our obtained average vp-vs ratios for 80% (4), 60% (3), and 40% (2) THF hydrate in Ottawa sand and our samples containing THF-water mixture (1). The arrows indicate increase in hydrate saturation.

Hydrate formation in Bentheim Sandstone

Bentheim sandstone is a relatively clean sandstone (>90% quartz) which further contains feldspar (<5%) and kaolinite (<5%). It typically shows high porosities of 20-25% (Stanchits et al., 2009) and high permeabilities of 1-2 Darcy (Stevens et al., 2007). 25±4 % porosity was determined from CT scans of our samples (Figure 44). Ultrasonic P and S-wave velocity variations were recorded during the cooling of Bentheim sandstone samples saturated with a water-THF mixture at Sh = 60% (Figure 45) and Sh = 80% (Figure 46). Hydrate formation is indicated by an increase in velocities. Hydrates started to form around -1°C for the sample with 60% hydrate saturation and at 3°C for the sample with 80% hydrate saturation. This difference in formation temperatures is mainly attributed to differences in cooling rate.

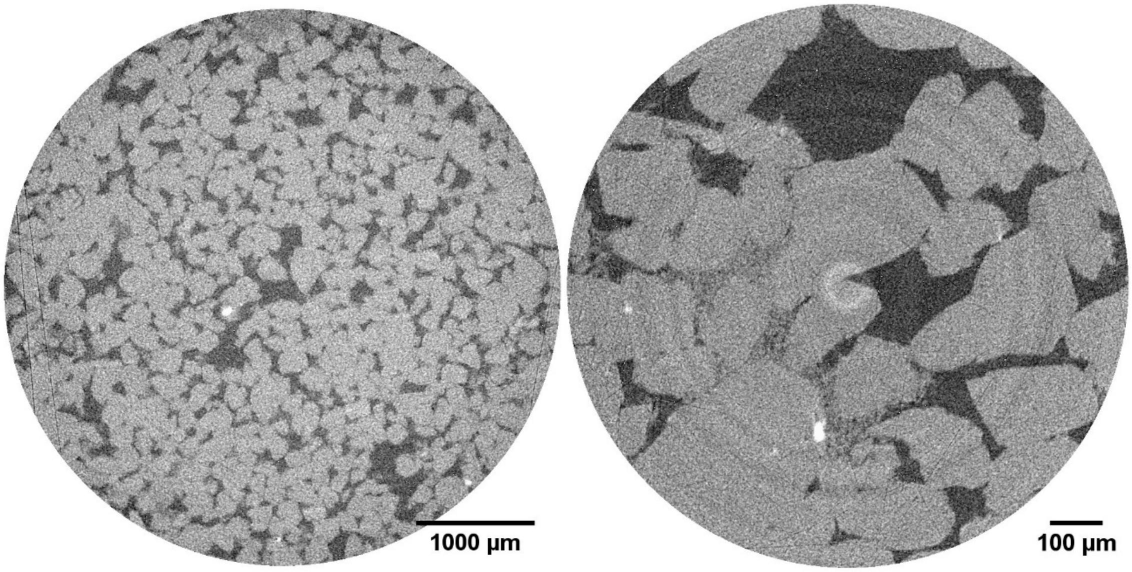

Figure 44: CT scans of Bentheim sandstone at 0.5X magnification (left) and 20X magnification (right). The clearly distinguishable grains in both images are quartz grains, the material which fills the pore space in some areas is believed to be clay (kaolinite) and the very light dots indicate grains of pyrite

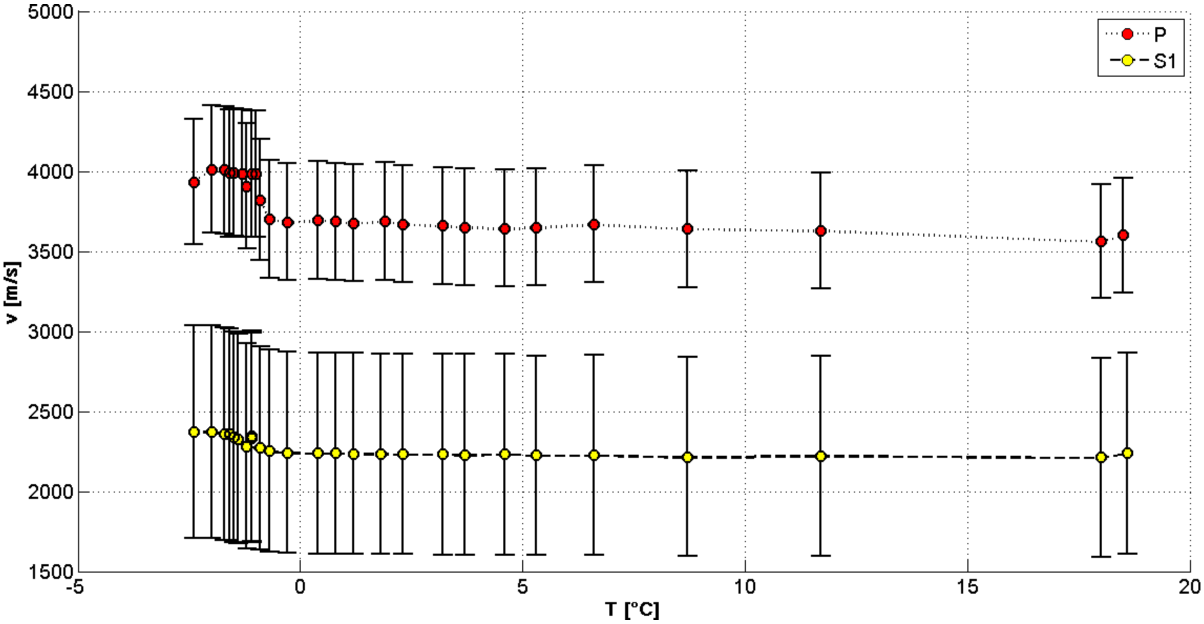

Figure 45: Ultrasonic velocities during cooling of Bentheim Sandstone sample with Sh=60%

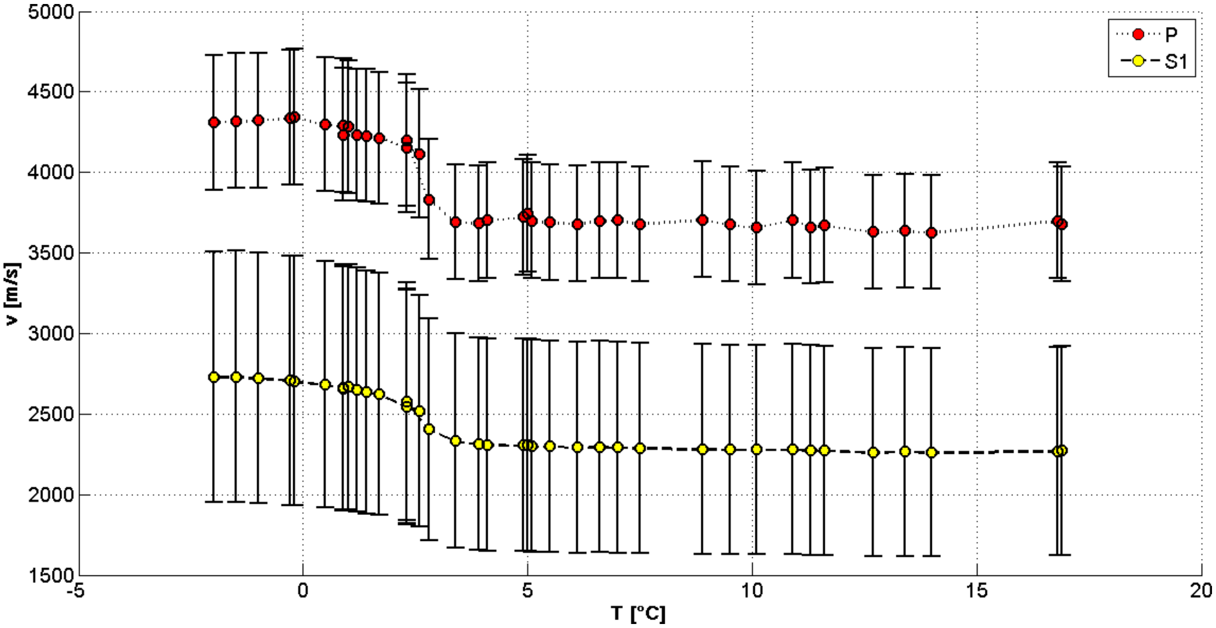

Figure 46: Ultrasonic velocities during cooling of a Bentheim Sandstone sample with Sh=80%

The resulting P- and S-wave velocities and Vp-Vs ratios before and after hydrate formation are compared to effective medium models by Ecker et al. (1998) and Helgerud et al. (1999) (Figure 47, Figure 48, and Figure 49, respectively).

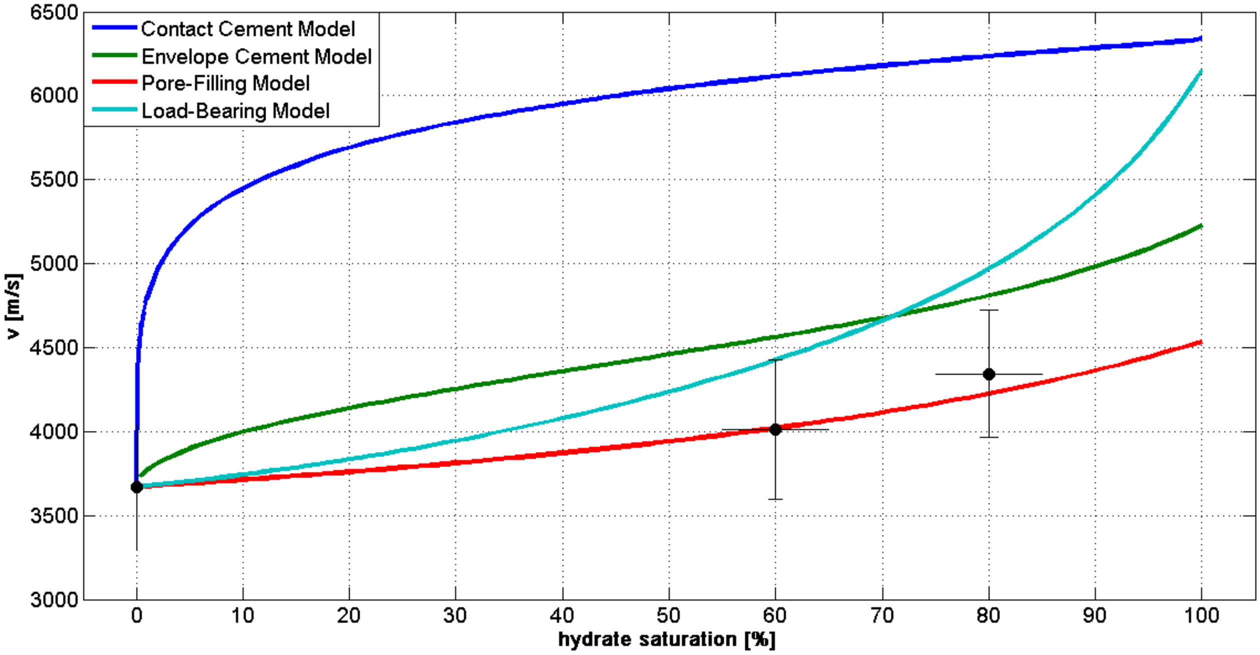

Figure 47: P-wave velocities for Bentheim sandstone samples with different hydrate saturations in comparison with effective medium model after Ecker et al. (1998) and Helgerud et al. (1999)

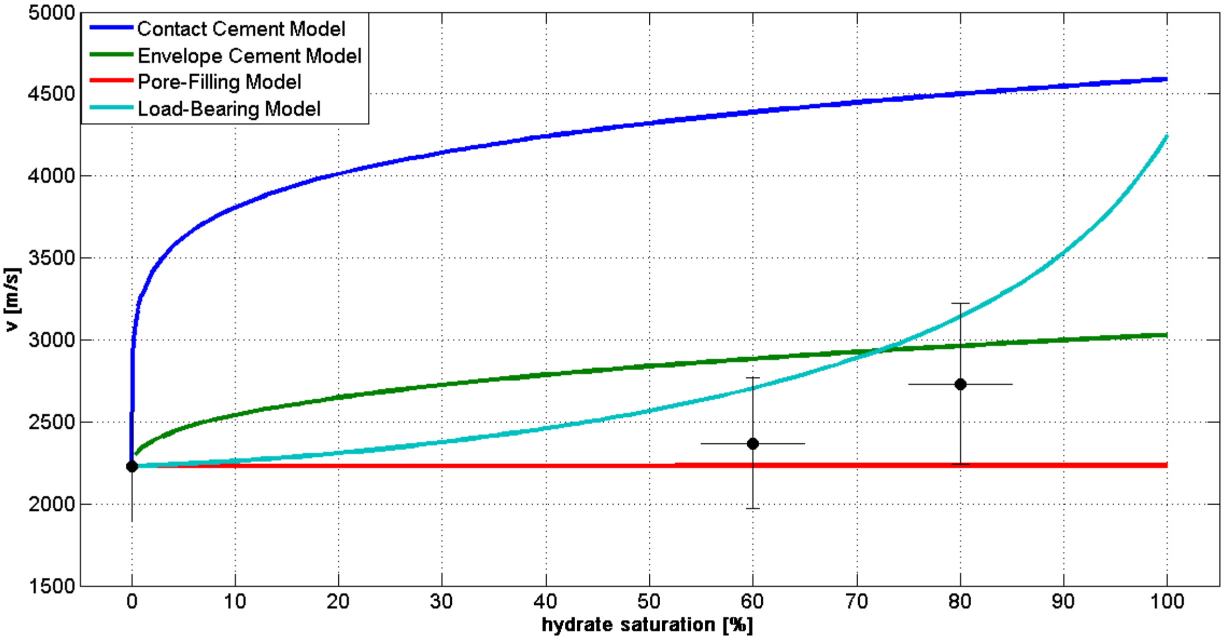

Figure 48: S-wave velocities for Bentheim sandstone samples with different hydrate saturations in comparison with effective medium model after Ecker et al. (1998) and Helgerud et al. (1999)

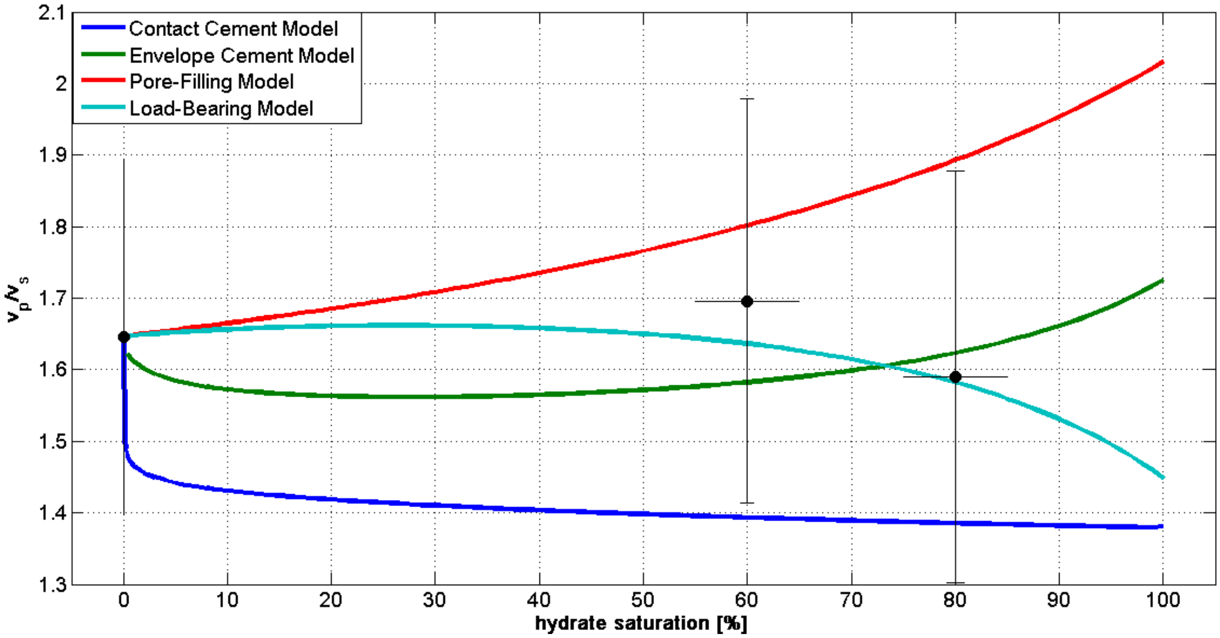

Figure 49: vp/vs ratio for Bentheim sandstone samples with different hydrate saturations in comparison with effective medium model after Ecker et al. (1998) and Helgerud et al. (1999)

The P-wave velocities coincide well with the pore-filling model while the S-wave velocities and the v_p/v_s ratio, respectively, are not conclusive yet. The data points lie between the envelope-cementing, pore-filling and load-bearing model.

Figure 50 shows the raw waveforms of the measured samples. The waveforms for the sample only containing water were taken at room temperature. Their corresponding velocities are shown in Table 3. The samples that contained a “100 %” hydrate were taken at 1 °C and are shown in green. It is noticeable that we have a velocity increase by a factor of 2 compared to the water samples. Also the peak to peak amplitude dropped. Cooling the sample further down to -10 °C resulted in another velocity increase as well as an increase in the peak to peak amplitude. This additional increase in velocity suggests that there is residual water in the sample that is now converted into ice causing an additional stiffening of the sample. Even though THF has a stochiometric relationship with water it is almost impossible to mix a mixture that results in 100 % THF hydrate. The reason for that is that THF is extremely volatile and during the mixing process of water and THF some of it evaporates leaving a mixture that results in a sample that contains excess water after hydrate formation. The waveform of the aluminium can be seen in Figure 50. The velocity calculation for its first arrival corresponds with literature values (Internet1).

Using those first arrivals and analyzing them regarding their frequency content is shown in Figure 51. It can be seen that the aluminum standard has much higher frequency content than the samples itself, as expected. Furthermore, the shape of the frequency curves is similar for each set of samples, showing that the measurements, especially for the hydrate bearing case, were reproducible. Now, comparing the peak frequency of the water samples with the frozen samples shows that they are fairly similar and also the shape of the curves show the same frequency content (Figure 51 d). On the other hand the "pure" THF hydrate samples have lower peak frequencies as well as a much faster decay or a lesser amount of higher frequencies in the frequency spectrum. This indicates that the wave propagating through the sample gets attenuated. From the waveforms we already concluded that there is residual water in the sample. This water is the cause of the attenuation that we observed because it is being squirted through the pore space causing a loss in energy (Johnston et al, 1979). However, after freezing the sample, the residual water turns into ice. The fact that the frequency spectrum of water is comparable with the one of the frozen sample is so similar leads to the assumption that the hydrate itself has no to very little attenuation.

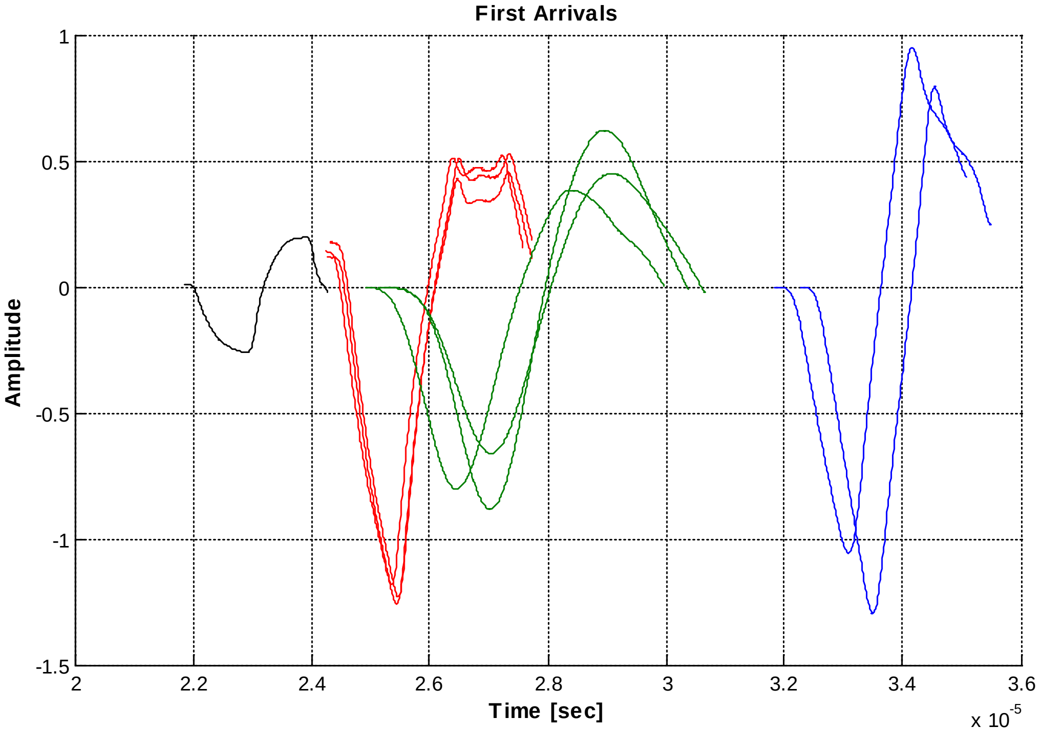

Figure 50: Raw waveforms for the first arrivals for the p-wave, aluminium standard (black), frozen sample (red), only hydrate bearing (green), and water (blue)

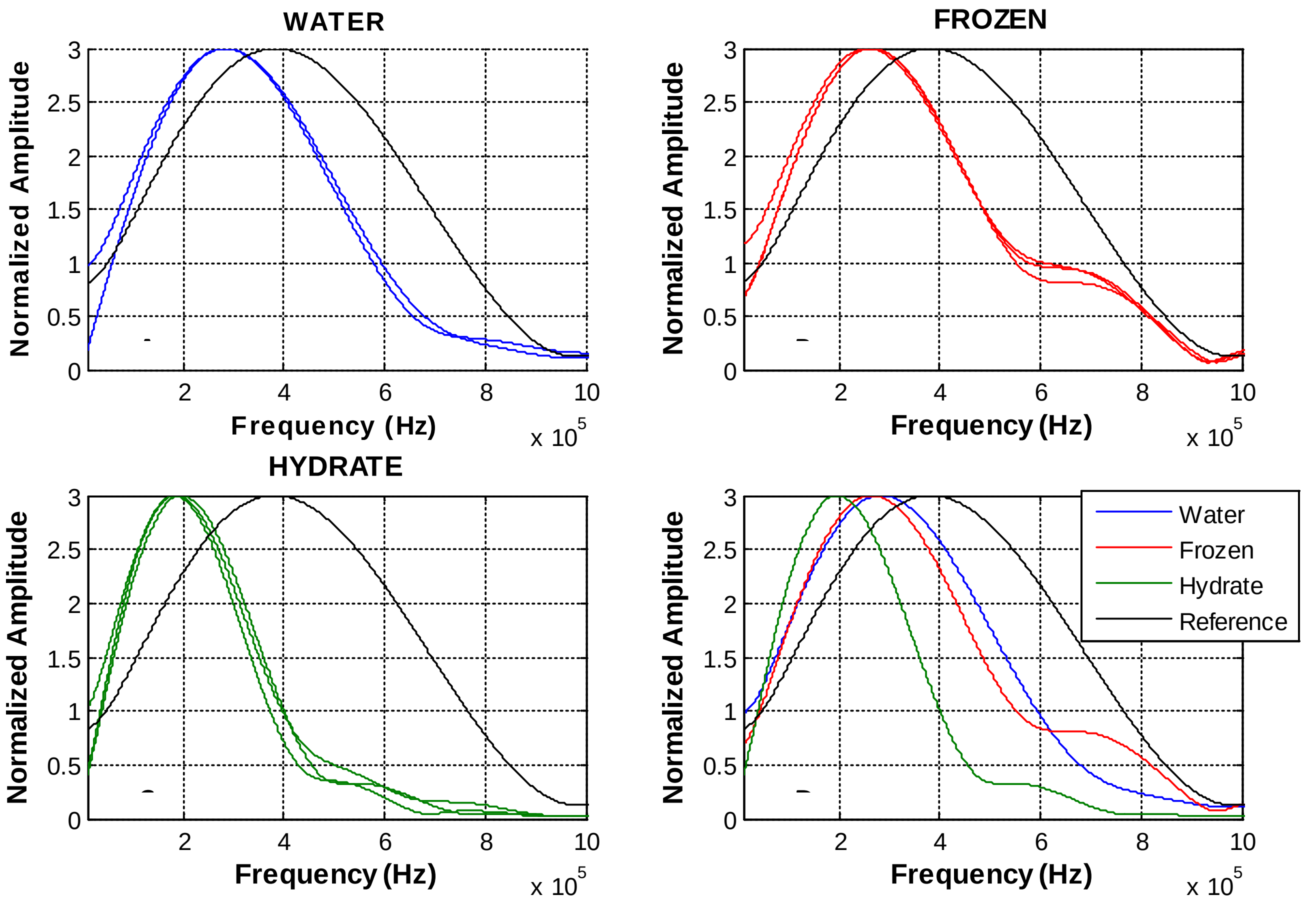

Figure 51: Frequency content of first arrivals. A) Frequency spectrum for water. B) Frequency spectrum for the frozen sample. C) Frequency spectrum for the "100 %" THF hydrate sample. D) Comparison of Water, Frozen, and Hydrate frequencies.

Table 3: Summary of calculated velocities, peak frequencies, and peak to peak amplitudes for all the samples.

Sample	Velocity (m/s)	Peak Frequency (kHz)	Peak-Peak
Water I	1527	285.8	2.0082
Water II	1558	281.1	2.0875
Frozen I	3484	276.0	1.6919
Frozen II	3544	264.1	1.6920
Frozen III	3556	269.9	1.7380
Hydrate I	3257	198.4	1.5037
Hydrate II	3090	183.9	1.1843
Hydrate III	3140	188.1	1.1101
Aluminium	6030	388.1	0.4617

Results from the Resonant Bar Experiment

These experiments were performed in collaboration with Lawrence Berkeley National Laboratory (Seiji Nakagawa and Timothy Kneafsey). The apparatus used was a Split Hopkinson Resonant Bar (SHRB). In the following, the data are referred to as SHRB data.

Figure 52, Figure 53, and Figure 54 show the inverted resonant bar data over the course of the entire experiment. During the first 37 hours of the experiment, the sample was partially water saturated and did not contain any gas hydrates. A confining pressure cycle was performed from 0 - 1 hours after the start of the experiment. The pressure was increased from 0.34 MPa to 15.6 MPa and decreased to 0.34 MPa again. At 11.5 hours the confining pressure was permanently increased from 0.34 MPa to 15.6 MPa resulting in an increase in moduli (Figure 52), velocities (Figure 53) and Poisson's ratio (Figure 54) and a decrease in attenuation (Figures 5 and 6). After 37 hours methane gas was injected into the sample at a pore pressure of 4.83 MPa. A strong increase in moduli, velocities and Poisson's ratio and a decrease in attenuation indicated the formation of methane hydrates between 40 and 42 hours after the start of the experiment (Figures 5, 6 and 7). The pore pressure was decreased to methane hydrate equilibrium after 109.5 hours. The partial dissociation of methane hydrate resulted in a decrease of moduli, velocities, Poission's ratio and an increase in attenuation (Figure 52, Figure 53, and Figure 54).

The injection of CO_2 and N_2 gas into the three-phase system of water, methane gas and methane hydrate started at 159 hours. The injection is accompanied by an increase in moduli, velocities and Poisson's ratio and a decrease in attenuation (Figure 52, Figure 53, and Figure 54). A hydrate blockage formed in the sample shortly after the injection of CO_2 and N_2 gas was started. The hydrate blockage caused a pore pressure gradient from the upstream end to the downstream end of the sample. In order to dissociate the blockage, the temperature of the sample was increased by 30-second heat pulses starting at 159.5 hours. Since the gas hydrate blockage could not be dissolved, temperature was increased until the end of the experiment after 211 hours. The increase in sample temperature results in a dissociation of gas hydrate in the pore space indicated by a decrease in moduli, velocities and Poisson's ratio as well as an increase in attenuation (Figure 52, Figure 53, and Figure 54).

For a more detailed analysis, we will refer to Young's modulus and shear modulus and their corresponding attenuations since the error introduced to P- and S-wave velocities during the inversion are greater. Figure 55 shows a CT image of the partially water saturated sample. The sand is packed inhomogeneously in layers. Darker colors indicate less densely packed areas. The average density of the sample before hydrate formation was 1.8 g/cm^3.

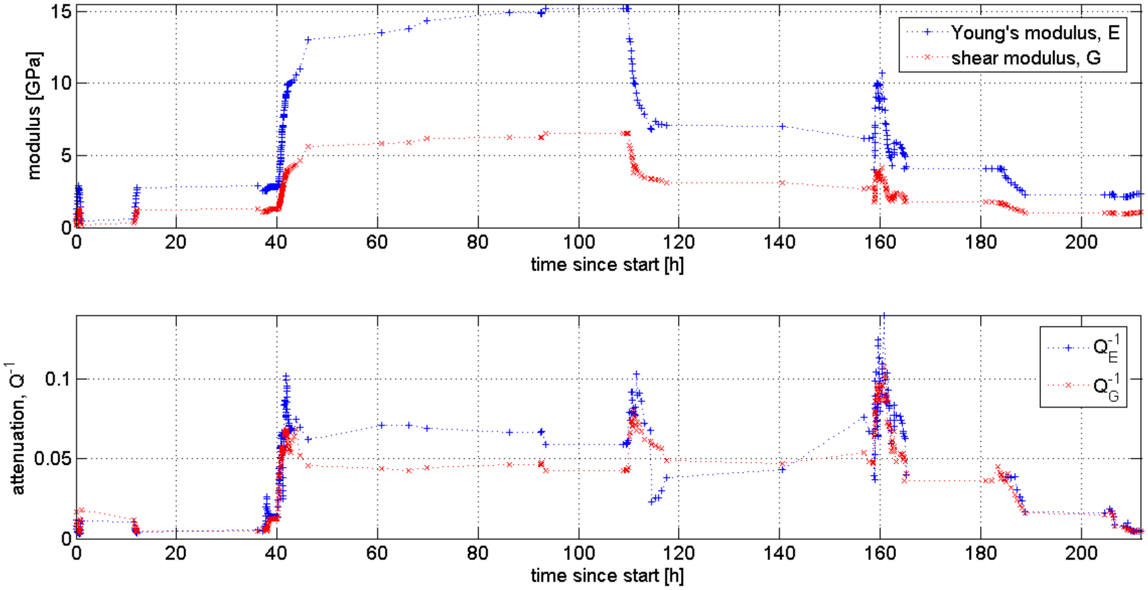

Figure 52. Inverted Young's modulus and shear modulus with corresponding attenuations from SHRB data

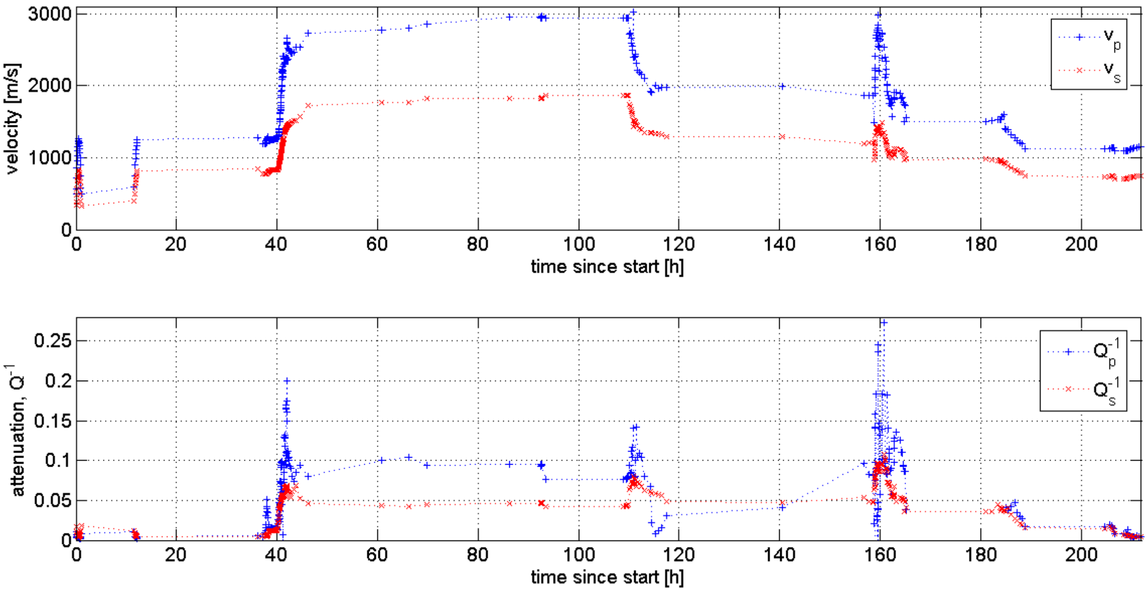

Figure 53. Inverted P- and S-wave velocities and corresponding attenuations from SHRB Data

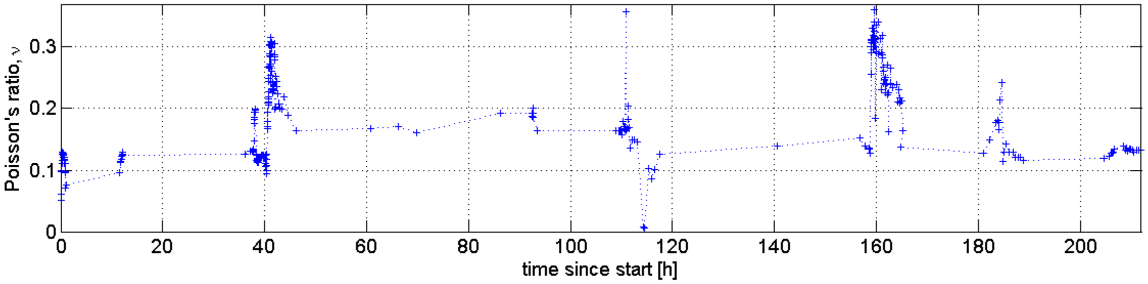

Figure 54. Poisson's ratio obtained from inverted SHRB data

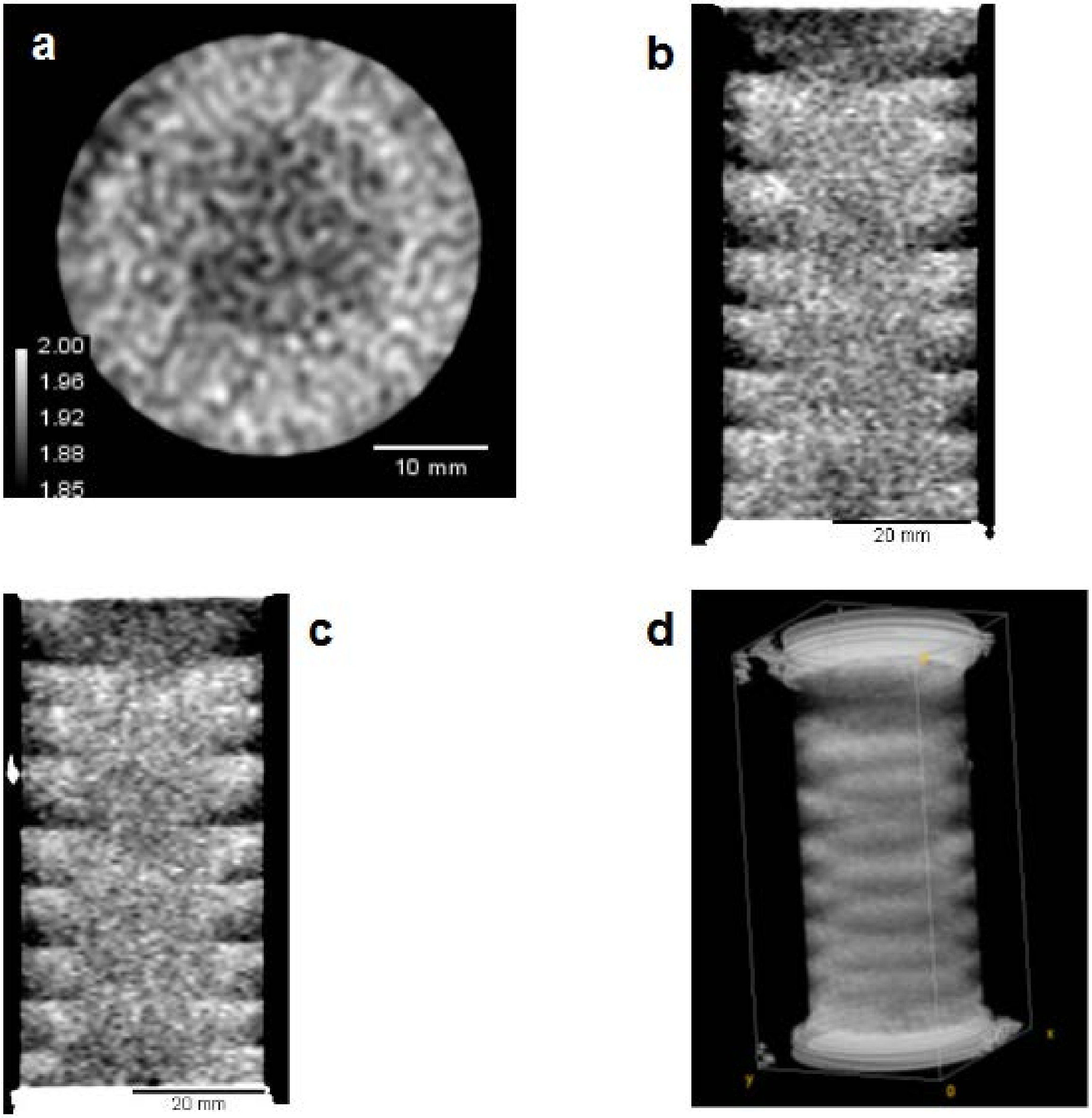

Figure 55. CT images of partially water saturated sample before hydrate formation

The CT image of the wet sample was used as a standard for further CT scans: subtracting the gray scale values (or densities) of the wet sample CT image from a CT image of a hydrate-bearing sample, results in positive and negative density differences. Positive density differences represent gas-hydrate filled sediment; negative density differences represent areas which were water-filled before and are now dry since the water has been used for gas hydrate formation.

Experimental Phase 1: Methane Hydrate Formation

After methane gas was injected into the sample 37 hours after the start of the experiment, no immediate effect was visible in the SHRB data. About 40 minutes after the methane injection started, a slight increase in Young's modulus occurs (Figure 56). An increase in extensional attenuation occurs at the same time. After the initial increase in extensional attenuation, the attenuation value decreases again but both - Young's and shear attenuation remain at a higher level. CT images taken at the same time indicate that a bulk body of methane hydrate has formed on the wall of the sample (Figure 57).

At 40.2 hours Young's modulus, shear modulus and the corresponding attenuations start to increase drastically. CT images taken at the same time indicate a movement of the hydrate-formation front from the surface of the initial hydrate body towards the opposing wall of the sample and the ends of the sample (Figure 58). The increase in both moduli continues until 42 hours and then remains at a stable value. The attenuations increase until 41.8 hours and then decrease again. Shear attenuation increases steadily whereas for extensional attenuation periods of increase and decrease occur resulting in an overall increase (Figure 60). After 42 hours no further change in CT images was visible indicating that the hydrate formation slowed significantly by that time. By the end of the methane hydrate formation process the area of the initial hydrate body appears to be free of hydrate (Figure 58).

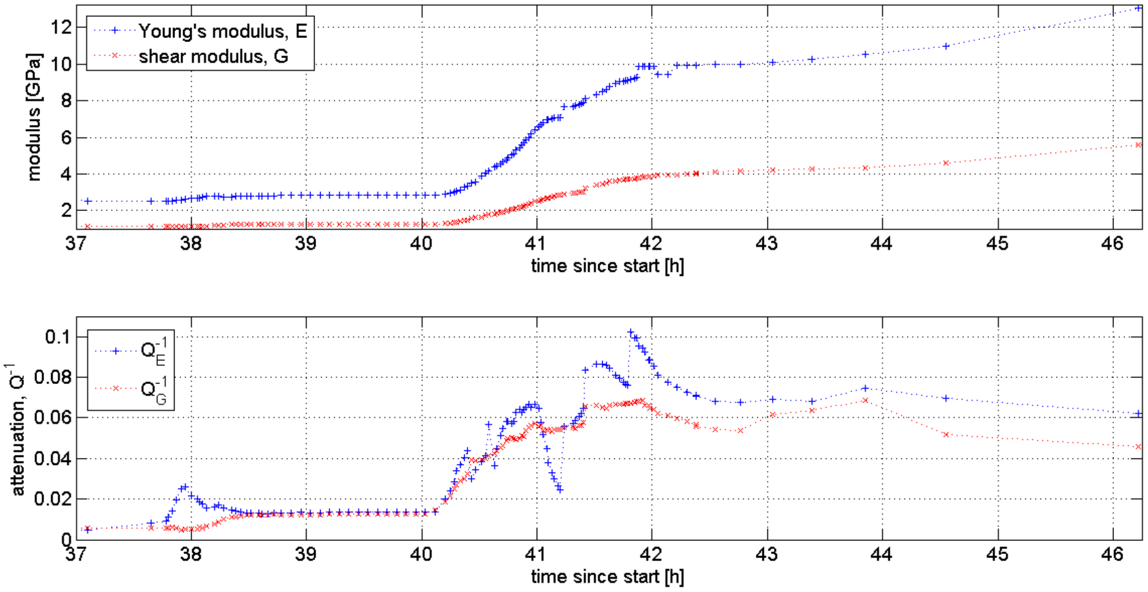

Figure 56. Inverted Young's modulus and shear modulus with corresponding attenuations from SHRB data recorded during methane hydrate formation. Methane injection was started at 37 hours; the initial methane hydrate formation lasted until approximately 42 hours.

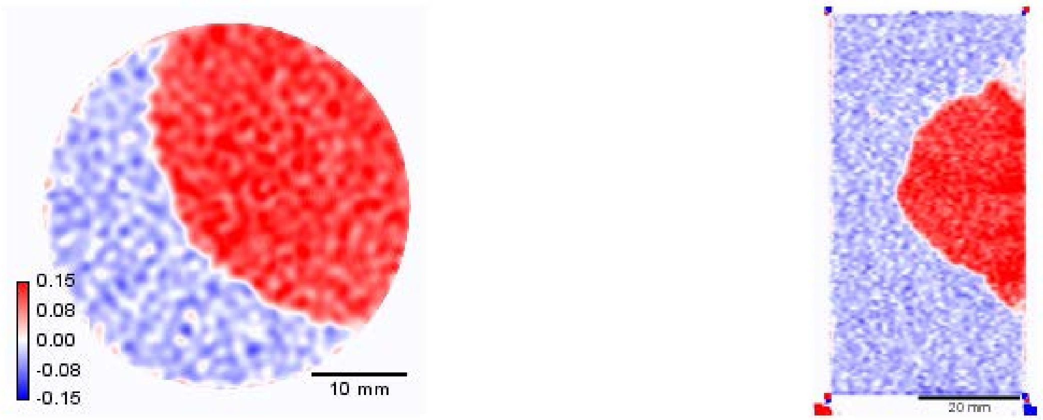

(a) xy slice (b) xz slice

(c) yz slice (d) 3D view

Figure 57. Change in density obtained by subtracting CT image of partially water saturated sample from CT image after initial methane hydrate formation (38 hours after start of experiment)

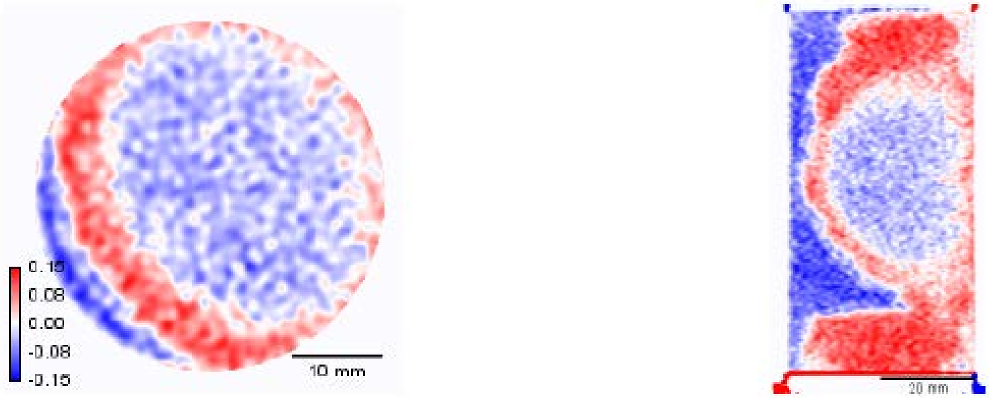

(a) xy slice (b) xz slice

(c) yz slice (d) 3D view

Figure 58. Change in density obtained by subtracting CT image of partially water saturated sample from CT image after continued methane hydrate formation (42 hours after experiment started)

Experimental Phase 2: Pore-Pressure Decrease to Equilibrium

After nearly all water in the pore space was converted to methane hydrate, the pore pressure was decreased from 4.82 MPa to 3.90 MPa resulting in a three phase system of methane, water and methane hydrate in the pore space. The decrease in pore pressure to methane hydrate equilibrium conditions resulted in a decrease in compressional and shear velocities (Figure 59). The values of both moduli remain above the initial values before methane hydrate was formed indicating that there is still methane hydrate left in the pore space. The attenuations react to the decreased pore pressure with an initial increase followed by a decrease. Extensional attenuation remains at a value higher than for the hydrate-free, partially water-saturated sample but lower than the value after full conversion to methane hydrate. Shear attenuation appears to be higher than in the previous phase of the experiment (Figure 60). The extension mode resonance peak was distorted between 110.8 hours and 156.9 hours by a strong bending mode interference. The torsion mode resonance frequency appeared to be split into two small peaks between 144.4 hours and 117.5 hours. This behavior is likely to cause great errors in attenuations thus the different behavior of Young's and shear attenuation in this phase of the experiment should not be interpreted.

No visible changes in the CT images occured during the second stage of the experiment but when comparing the average density values for each slice before and after the pore pressure decrease, an overall negative change is observed. This decrease in density is attributed to a partial dissociaton of methane hydrate during this stage.

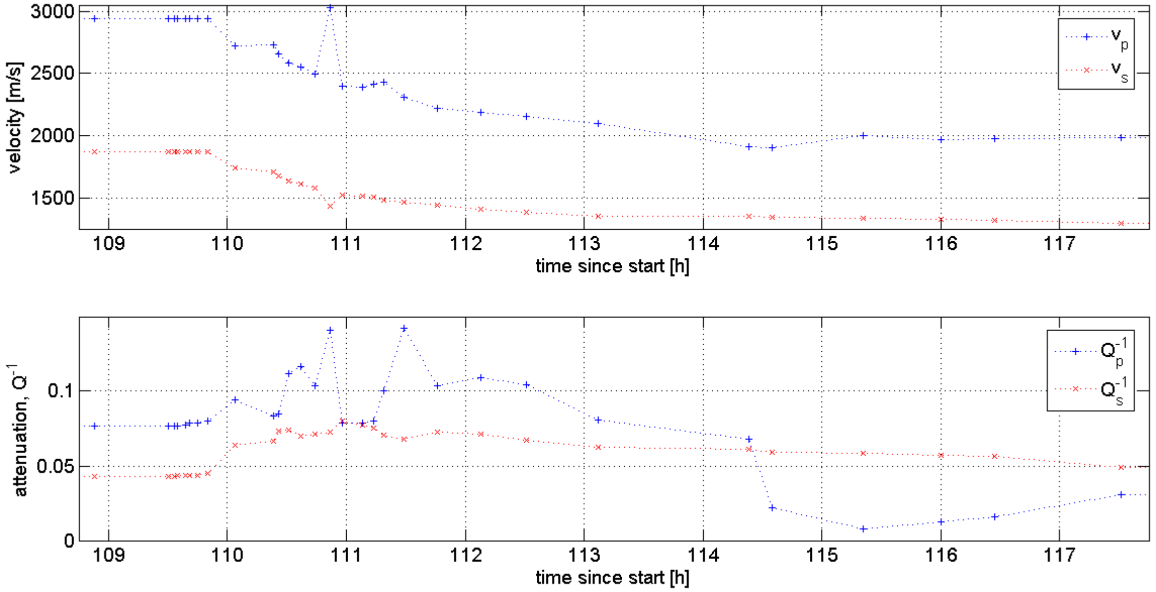

Figure 59. Compressional and shear velocity with pore pressure decrease

Experimental Phase 3: CO_2/N_2 Gas Substitution

A CO_2 and N_2 gas mixture was flowed through the sample at a pore pressure of 9.6 MPa. Young's and shear modulus all show significant increases upon gas injection followed by a decrease due to heating of the sample (Figure 59). Due to the hydrate blockage in the sample, gas hydrate formation is stopped before full conversion of all water and CO_2/N_2 gas in the sample is reached. That results in lower values for Young's modulus and shear modulus than after methane hydrate formation in Phase 1. Both attenuations increase upon gas injection and then periodically increase and decrease with each heating cycle.

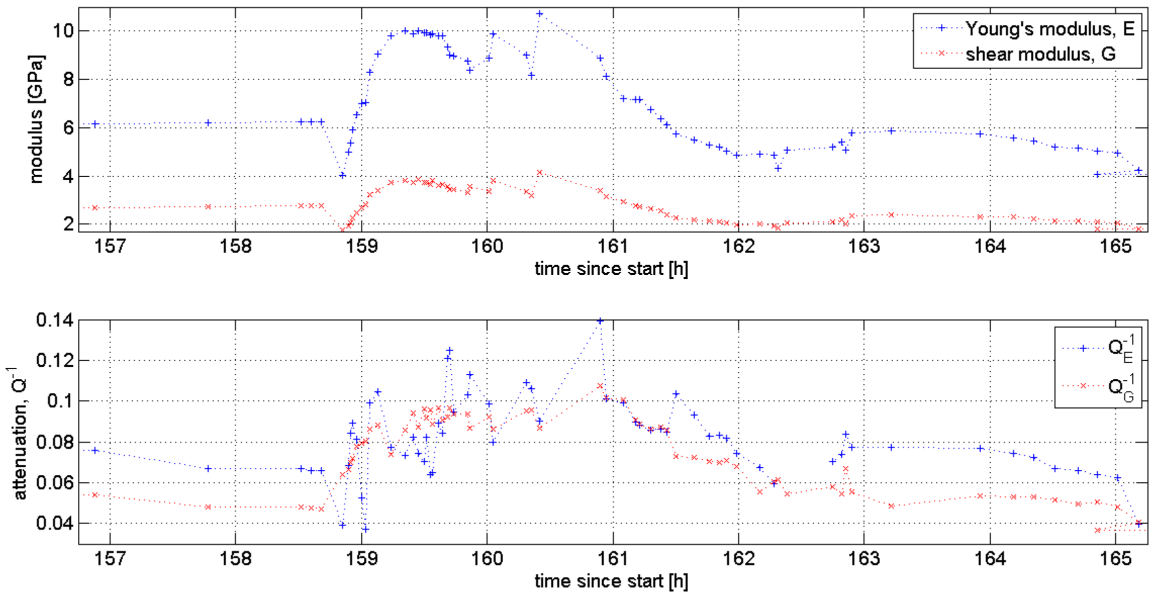

Figure 60. Inverted Young's modulus and shear modulus with corresponding attenuations from SHRB data recorded during partial dissociation of methane hydrate due to CO_2/N_2 injection and temperature changes.

3. Complex Resistivity of Methane-Hydrate Bearing Samples

Samples Used

We prepared nine cores (Figure 61) for our measurements: three Foxhill sandstone samples, three Castlegate sandstone samples, and three Bishop Tuff samples were cut into one inch diameter and two inch length cylinders with holes drilled to host electrodes.

Figure 61: Sample overview for complex resistivity measurements. (A) Bishop Tuff, (B) Castlegate Sandstone, and (C) Foxhill Sandstone

We covered the ends of the core samples with conducting epoxy and attached wires to the surfaces. After the samples are fully prepared and oven dried, they are kept in a desiccator at 100% humidity to allow a thin layer of water to cover the grain surfaces. Over time the sample saturate fully with water vapor that can be confirmed by periodic measurements of the sample weight. Once the weight is stabilized, the samples are put into the pressure vessel, pressurized with methane, and cooled below the methane hydrate stability temperature. In theory, the hydrates will start forming at the gas – water interface and over time the hydrates will grow towards the grain surfaces. The formation of hydrates will cause a change in resistivity and a drastic velocity increase according to the envelope cementing model.

Experimental Description and Procedure to form Methane Hydrate Sediments

In this work, an experimental setup to study methane hydrate formation in sediments was designed and constructed. The setup is capable of operating at high pressures (approximately 1500 psi or 10.34 MPa) and over a range of temperatures (from -5 °C to 20 °C). The setup consists of (1) a high-pressure ISCO pump (1000 HL series with a maximum operating pressure of 2000 psi), (2) a stainless steel experimental reactor cell, 170 ml in volume, (3) an external refrigerated, recirculating chiller, and (4) a cooling bath for fine temperature control. The setup is constructed and installed (Figure 62) and can be used for future hydrate experiments.

Figure 62 shows the schematic diagram of the experimental setup. The schematics in Figure 62 and the image in Figure 63 shows the setup consists of a high-pressure ISCO pump, a stainless steel experimental cell, a chiller and a cooling bath. The experimental cell is placed in the cooling bath to control the temperature of the system. In this setup, a coolant (glycol) is circulated into the cooling bath using the chiller to control the temperature. The experimental cell is also connected to the ISCO pump to maintain the pressure of the system at up to 1500 psig (103.4 bar). Currently, the pressure cell comprises two different outlet lines. The first outlet line connects to an outlet valve that is used to vent the system. The second outlet line connects to a pressure relief that will open if the pressure of the cell exceeds a certain set pressure. Additionally, the setup is connected to a gas cylinder that is located in a gas cabinet.

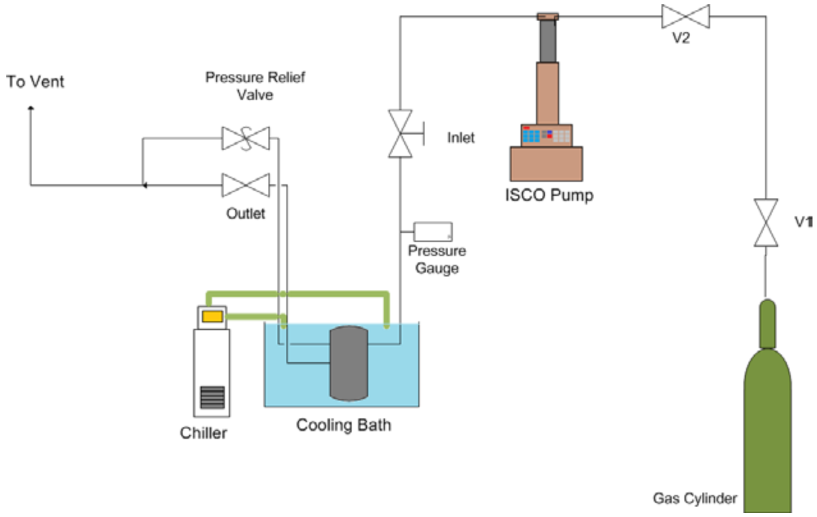

Figure 62: Schematic diagram of the experimental setup of the system.

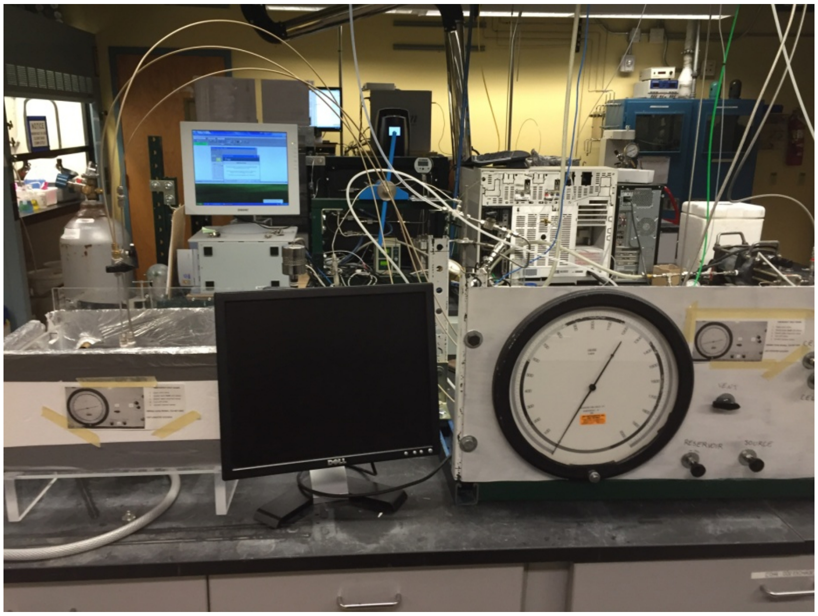

Figure 63: Image of the pressure controls in the experimental setup.

Sample Preperation

The experiments comprise electrical measurements before, during, and after hydrate formation in three different rock samples. The purpose of this research is to experimentally observe the change in resistivity due to hydrate formation. In total, nine samples have been prepared – three Castlegate Sandstones, three Fox Hills Sandstones, and three Bishop Tuff samples. All samples were cut into cylinders with one inch diameter and two inches length. After the samples were prepared they were placed into a vacuum oven to completely dehydrate the samples.

The first experiments are conducted when the samples are dry. These first measurements are taken as a baseline and are compared with the measurements after hydrate formation to determine full conversion of water into methane hydrates.

After the samples are measured dry they are placed into a desiccator with 100% humidity. The samples absorb the moisture. This absorption is monitored by measuring the relative weight gain for each sample (Table 4).

All the measurements mentioned before are performed at room temperature and atmospheric pressure. To initiate hydrate formation, the samples are placed into a pressure vessel equipped with wire feed-throughs which allow us to perform the electrical measurements under pressure. After the sample is placed into the vessel and connected to the electrical wires it is pressurized with methane up to 1200 psi. Once the pressure is reached the samples will be measured again. The pressure vessel is submerged in a cooling bath for temperature control. To induce hydrate formation the temperature is decreased to 1 °C. Once the temperature and pressure conditions are suitable for hydrate formation, continuous measurements are conducted to record the change in resistivity due to hydrate formation.

Complex resistivity in sandstones was measured before, during and after hydrate formation. We report here results for the Castlegate sandstone samples (CG1). The measured conductivity (real and imaginary part) for one frequency is shown in Figure 67 for the whole length of the experiment. The experiment procedure can be divided into 4 stages.

Stage 1: Pressurization and Cooling

The prepared sandstone was taken out of the desiccator where it had been exposed to humidity until it reached full saturation. The sample was placed into the pressure vessel and measured for the first time at atmospheric pressure (Figure 67). The second measurement was conducted after applying methane with a pressure of 1500 psi onto the sample. As we can see, the conductivity value between the first and the second measurement does not vary. After the second measurement, the cooling of the sample started. Measurement 3 and 4 only show small changes in conductivity (Figure 68) which is due to the change in temperature. Once within the hydrate stability temperature we observed a drop in conductivity between measurement 4 and 5 which indicated the start of the hydrate formation within the sandstone. We continued measuring at 1 hour intervals for the next 6 hours and observed a further decrease in conductivity due to further hydrate formation.

Stage 2: Stabilization

During this stage we kept the temperature constant (~3.5 °C) and continued measuring for about 2 weeks. We saw no changes occurring in the real part of the conductivity values during this period of time indicating that the conversion of water and methane to hydrate must have stopped. However, looking at the imaginary part shows a continuous drop of conductivity over time (Figure 68).

Stage 3: Freezing

To insure complete conversion of water to hydrate, we lowered the temperature to below the freezing point of water (~-2 °C). As we can see, we have another sharp drop in conductivity once the sample is below 0 °C indicating that in the sample was residual water present. Also, over time the conductivity value is dropping and not reaching a constant value. During this stage we also observed a power outage which lasted for about 2 hours causing the cooling bath to stop working. During these two hours the sample warmed up to about 4 °C which is still within the hydrate stability temperature but above the freezing point of water causing the sample to start thawing. After the power was back the sample was brought back to ~-2°C.

Stage 4: Thawing

In this stage the temperature was brought back to about the temperature value we had before Stage 3 causing existing ice to melt. Even though the cooling bath was set to the same temperature we had during stage 2, the temperature inside the vessel did not go above 2°C. Therefore we had to increase the cooling bath temperature step by step to reach a value of about 3.5 °C. With the same temperature conditions, we are now able to compare our measured conductivities from stage 2 with stage 4. As we can see, the real part of the conductivity is about the same value whereas the imaginary part shows a much larger difference.

Micro Structure of Complex Resistivity Samples

Castlegate Sandstone is a fluvial sandstone consisting mainly of quartz with a porosity of 21% (Figure 64) and permeability around 1 Darcy. Fox Hills Sandstone is a deltaic sandstone with significant clay content. Its porosity is around 28%, however, the permeability is lowered to around 50 mD due to the clay content (Figure 65).

Bishop tuff is a volcanic ash deposit with varying porosity. Near the top of the deposit porosities are as high as 37% towards the bottom (120 m burial depth) porosities decrease to 4%. The CT images reveal that this rock is more heterogeneous than the two sandstones (Figure 66). Grain size is highly variable with a lot of very fine grained material limiting pore connectivity and indicating low permeability. We will determine the exact porosities of the samples with specialized core methods used to measure porosity in shales and mudrocks (gas adsorption, NMR, water immersion).

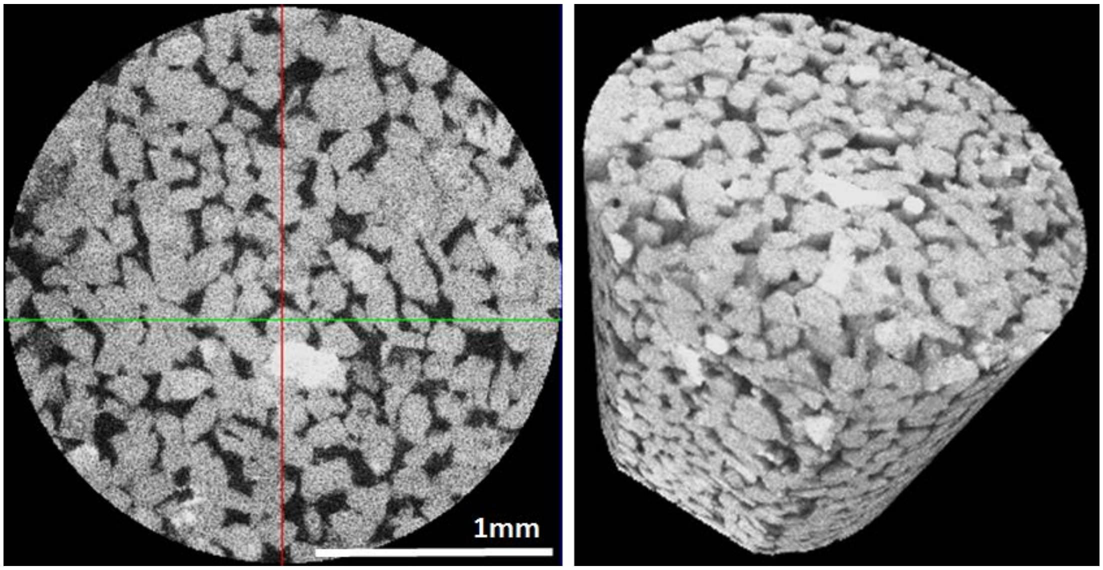

Figure 64. Micro CT image of Castlegate Sandstone- cross sectional view and 3D view

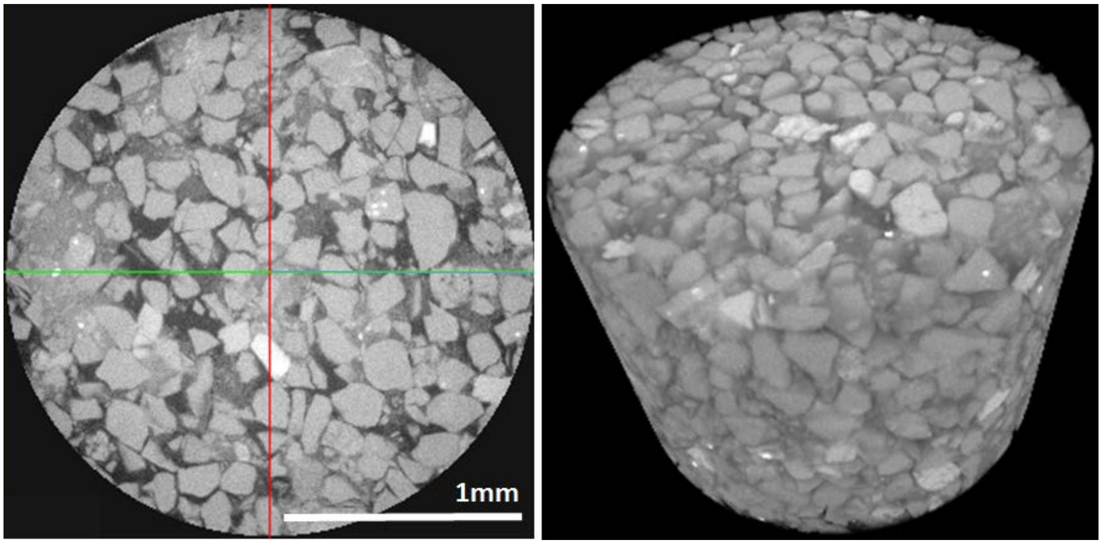

Figure 65. Micro CT images of Fox Hills Sandstone – cross sectional view and 3D view

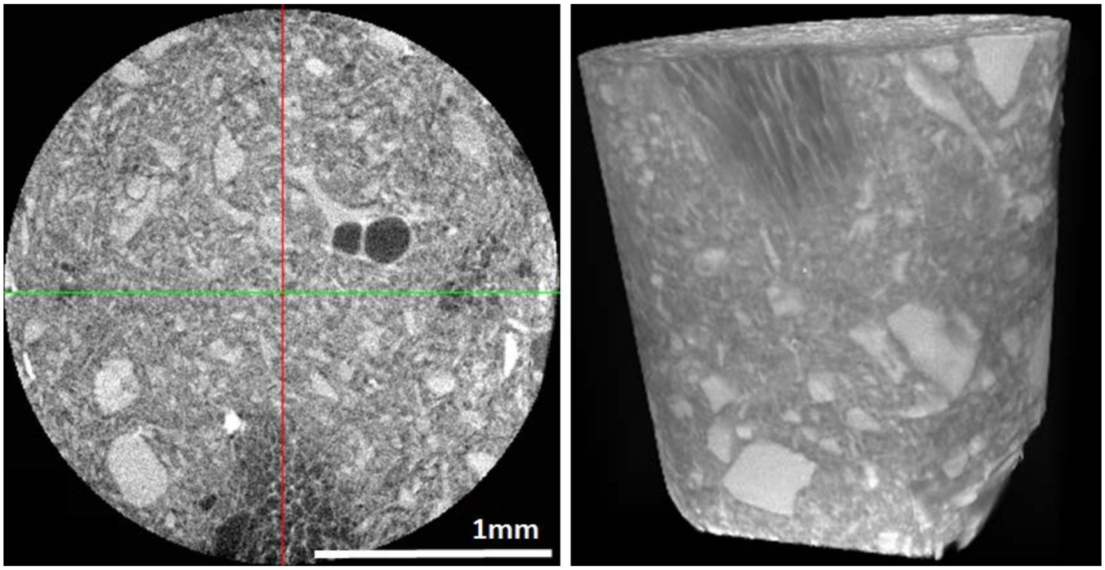

Figure 66. Micro CT images of Bishop Tuff – cross sectional view and 3D view

Results

With the measured conductivity we can distinctively determine when hydrate formation started and when it ended, as well as that not all of the water was converted into hydrate (Figure 67 and Figure 68). Additionally, we showed that forming ice underneath the hydrate layer caused it to break up and making more water available for hydrate formation after thawing the ice.

Interpretation

Lowering the temperature to below the freezing point of water caused any available water to freeze. This was observed by an additional drop in conductivity. As a result of the formation of ice the hydrate layer was broken off and after thawing the ice back to water, that water formed more hydrate. This additional formation of hydrate can be seen in the imaginary part of the conductivity. To understand this, we have to understand what the real and imaginary part of the conductivity mean. The real part of the measured conductivity can be seen as the bulk property of the rock whereas the imaginary part measures the conductivity along the grain surfaces of the rock. Even though the water contained in humidity is deionized the grains themselves have cations which become part of the water – the water naturally becomes more conductive. During the second hydrate formation in stage 4 the residual water becomes less but charged with more ions therefore the imaginary part of the conductivity is higher than during the 2 stage.

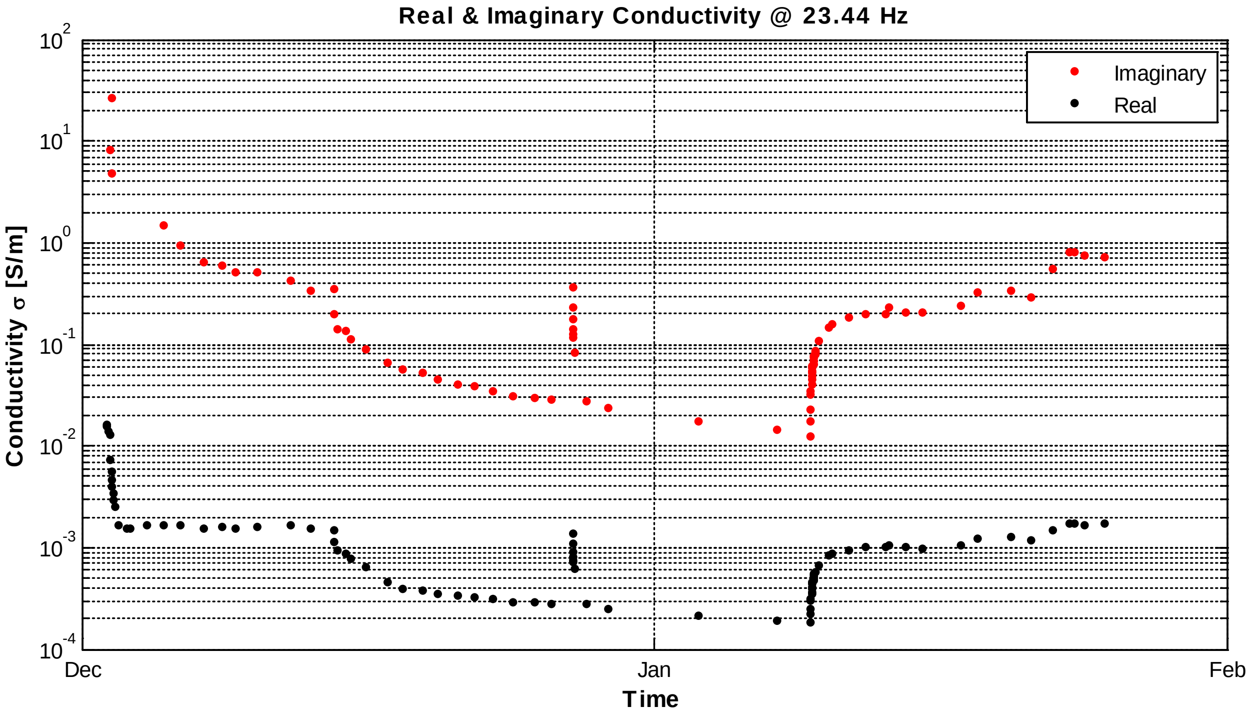

Figure 67: Real and imaginary conductivity for all 92 measurements of the experiment for one frequency

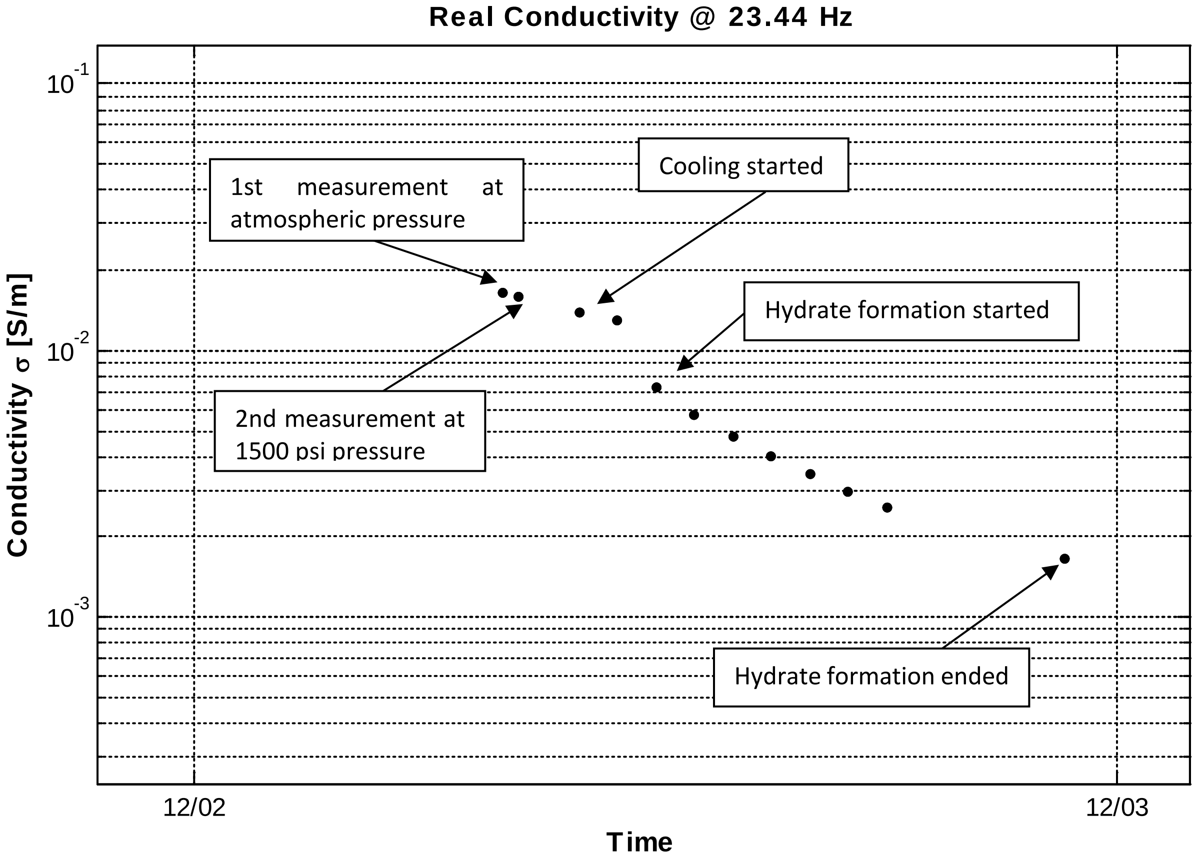

Figure 68: Stage 1 of the experiment - Cooling.

Estimated Water and Methane-Hydrate Saturations

The samples were humidified at 100% humidity for several days to weeks. For the calculations of water saturation and hydrate saturation shown in Table 5 we used a sample volume of 25.74 cc, the measured weight difference between wet and dry samples, a density of 0.9 g/cc for methane hydrate, 21% porosity for Castlegate sandstone and 28% porosity for Fox Hills sandstone. For the Bishop tuff samples the lower and upper limit of the porosity were used (4% and 37%). The hydrate saturation values are based on the assumption of full conversion of all present pore water.

Due to the large uncertainty in pore volume, water and hydrate saturation estimations for the Bishop tuff samples (VA1, VA2, VA3) vary by one order of magnitude. The amount of water absorbed by the tuff samples was small compared to the two sandstones which can be caused by low permeability or comparably lower porosity. Porosity measurements will restrain the saturation values.

Table 4: List of complex resistivity samples

sample	mass [g]		Vwater [cc]	Swater[%]		Shydrate [%]	
	dry	wet					
CG1	51.71	52.19	0.48	8.88		11.39	
CG2	53.48	54.48	1	18.50		23.74	
CG3	49.3	50.12	0.82	15.17		19.47	
FH1	56.21	57.31	1.1	15.26		19.59	
FH2	56.92	58.02	1.1	15.26		19.59	
FH3	49.25	50.19	0.94	13.04		16.74	
				for Φ=4%	for Φ=37%	for Φ=4%	for Φ=37%
VA1	40.25	40.42	0.17	16.51	1.79	21.19	2.29
VA2	40.66	40.86	0.2	19.43	2.10	24.93	2.69
VA3	39	39.15	0.15	14.57	1.58	18.69	2.02

Complex Resistivity Data for Sample VA2

We measured complex resistivity on 2 cores but had to abort one of the experiments due to a leak in the pressure cell. Thus, we are presenting data for one sample of Bishop tuff (VA2).

Table 5: methane pump volume and calculated hydrate volume, the volume number represents the experimental stage

Sample #	Volume [cc]	Temperature [°C]	Volume of Hydrates [cc]
4	756.71	25	0
5	755.35	15	0
6	753.22	10	1.121
7	751.52	5	2.016
8	750.47	2.5	2.568
9	749.6	1	3.026
10	749.24	1	3.216
11	749.24	1	3.216

12	749.31	1	3.216
13	751.18	1	3.216
14	751.19	1	3.216
15	751.18	1	3.216
16	751.16	1	3.216

Figure 69, Figure 70, and Figure 71 show real conductivity, quadrature conductivity and real resistivity during the entire experiment for one frequency. Complex resistivity was first measured at room temperature and atmospheric pressure outside of the pressure vessel. The sample was then placed in the pressure vessel and complex resistivity was measured again at room temperature and atmospheric pressure. It was then pressurized with methane gas to 1200 psi. To reach hydrate stability conditions the sample needed to be cooled below 14 °C. The temperatures are measured outside of the pressure vessel in the cooling bath since our setup does not contain enough electrical wire feed-throughs to include a thermocouple in the pressure cell.

A drop in both real and quadrature conductivity was observed as the temperature was decreased below hydrate stability. The conductivities stabilized upon reaching 1 °C and continued to decrease slowly over time as the sample was left at constant pressure and temperature conditions. This slow decrease in conductivity (from stage 9 to stage 21) can be attributed to the ongoing conversion of water into methane hydrate. The variation of conductivities in these stages is possibly caused by temperature fluctuations.

During the temperature increase back to room temperature we observed an increase in conductivity which can be attributed to the dissociation of hydrate and the related increase of the amount of water in the pore space.

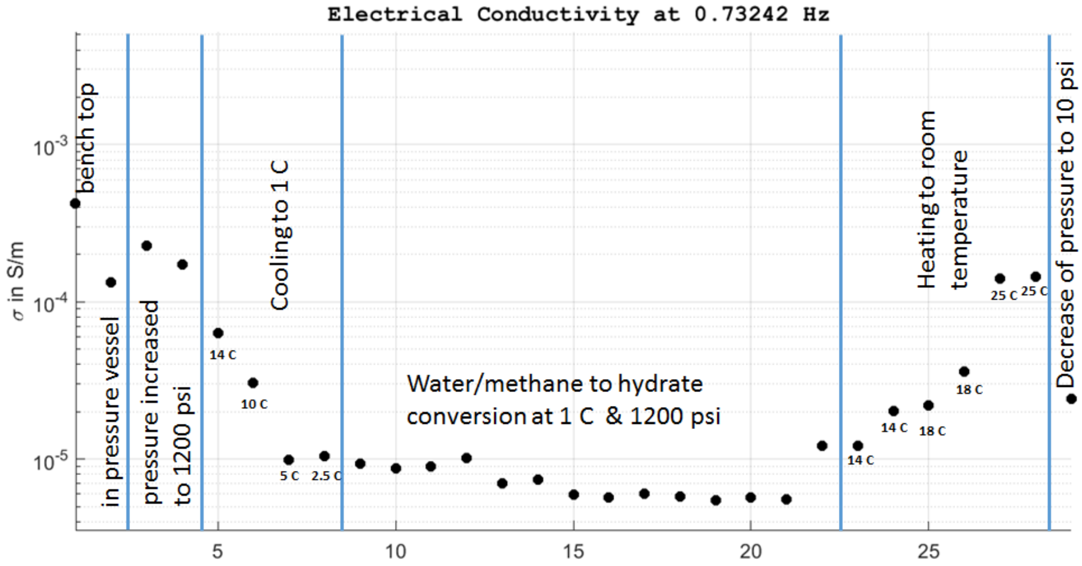

Figure 69: Real electrical conductivity for all 29 stages of the experiment including pressurization, cooling, hydrate formation, heating and depressurization at one frequency.

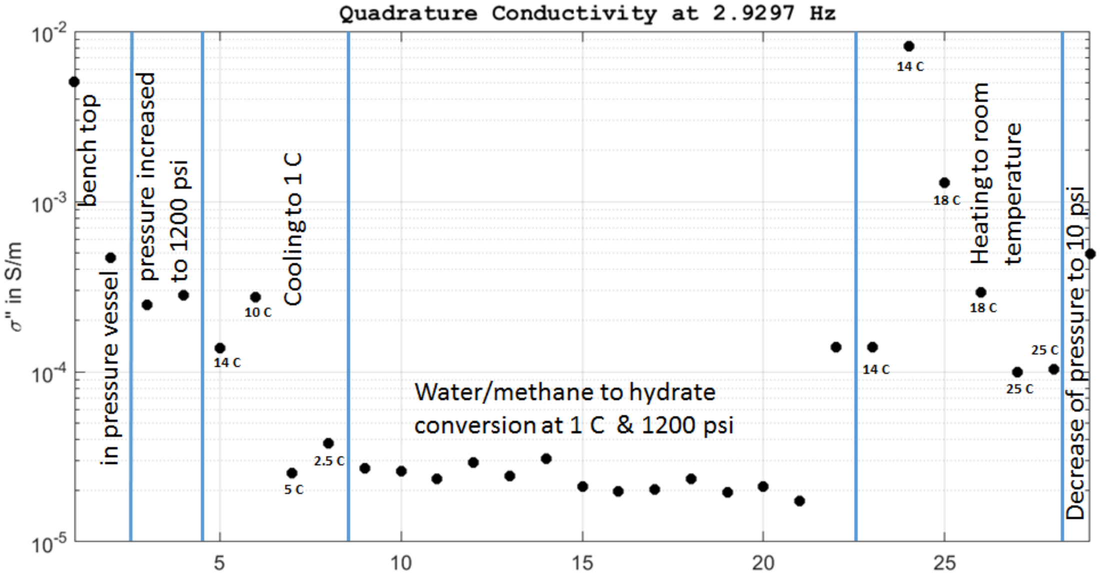

Figure 70: Imaginary (quadrature) electrical conductivity for all 29 stages of the experiment including pressurization, cooling, hydrate formation, heating and depressurization at one frequency.

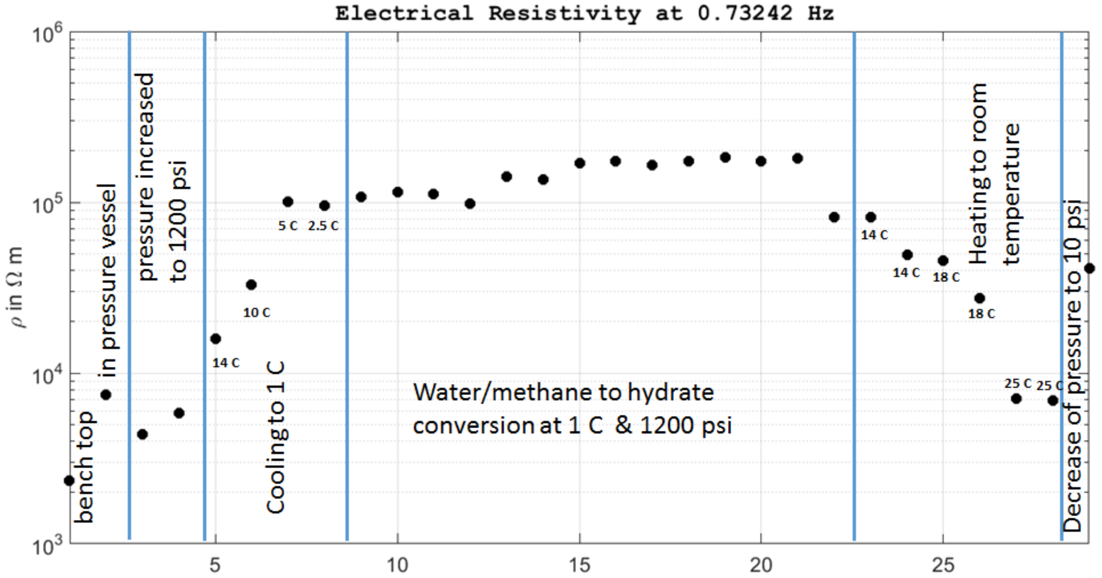

Figure 71: Real electrical resistivity for all 29 stages of the experiment including pressurization, cooling, hydrate formation, heating and depressurization at one frequency.

Figure 72 and Figure 73 show real and quadrature conductivity as a function of frequency. Real conductivity increases with increasing frequency (Figure 74) while quadrature conductivity shows a local maximum at 0.1 Hz, then decreases and increases with increasing frequency for values higher than 10 Hz. This behavior is in agreement with data and models described by Revil et al. (2014) describing how conductivity varies with frequency due to different physical processes dominating at different frequencies.

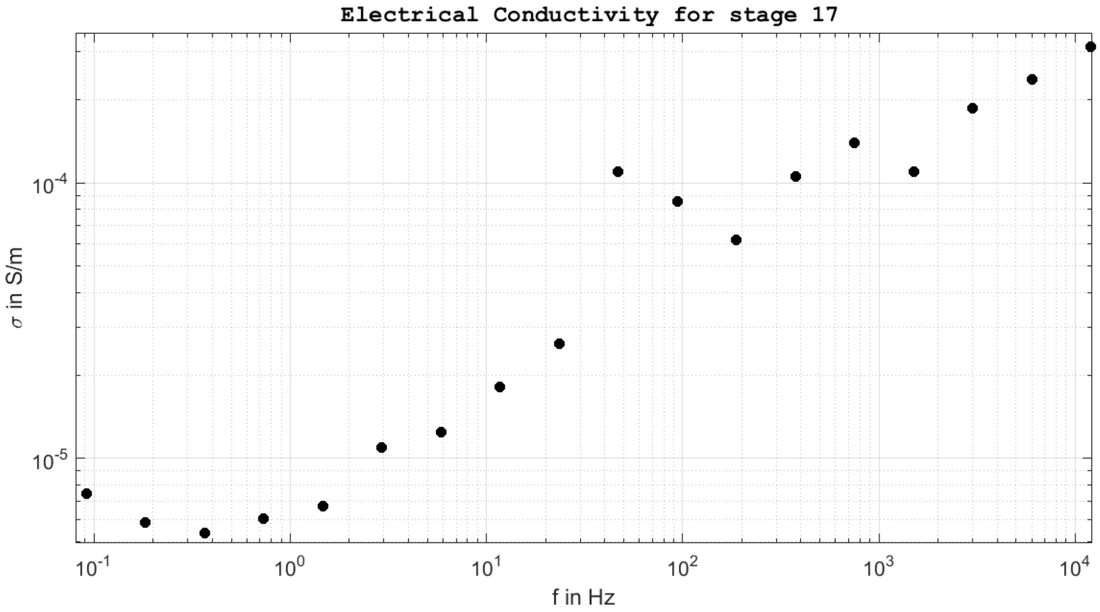

Figure 72: Real electrical conductivity for all 18 frequencies, shown for 1 experimental stage (1200 psi, 1 C)

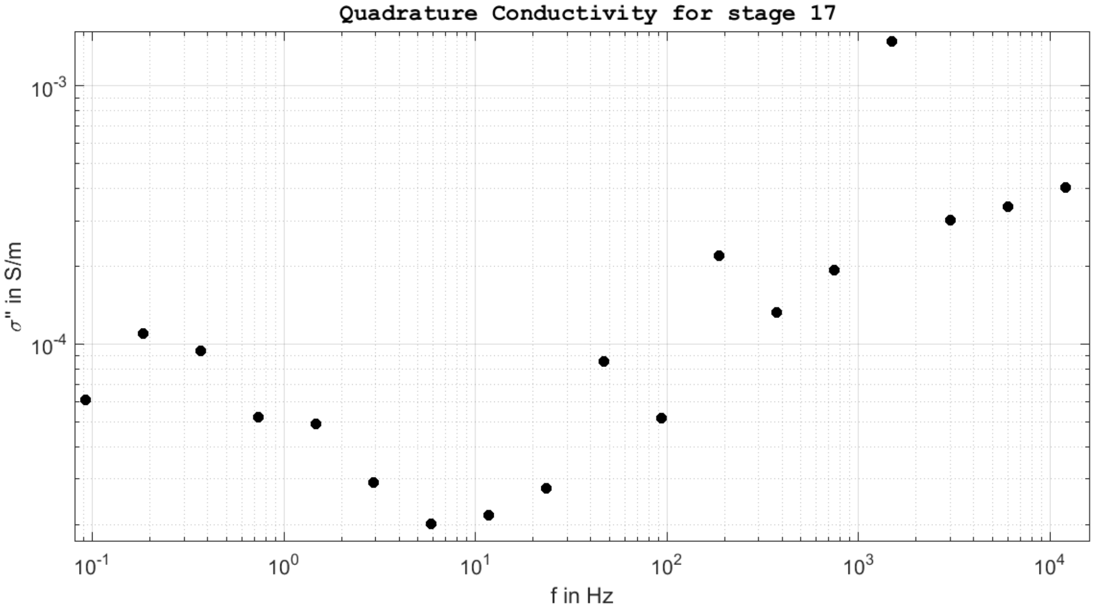

Figure 73: Imaginary (quadrature) electrical conductivity for all 18 frequencies, shown for 1 experimental stage (1200 psi, 1 C)

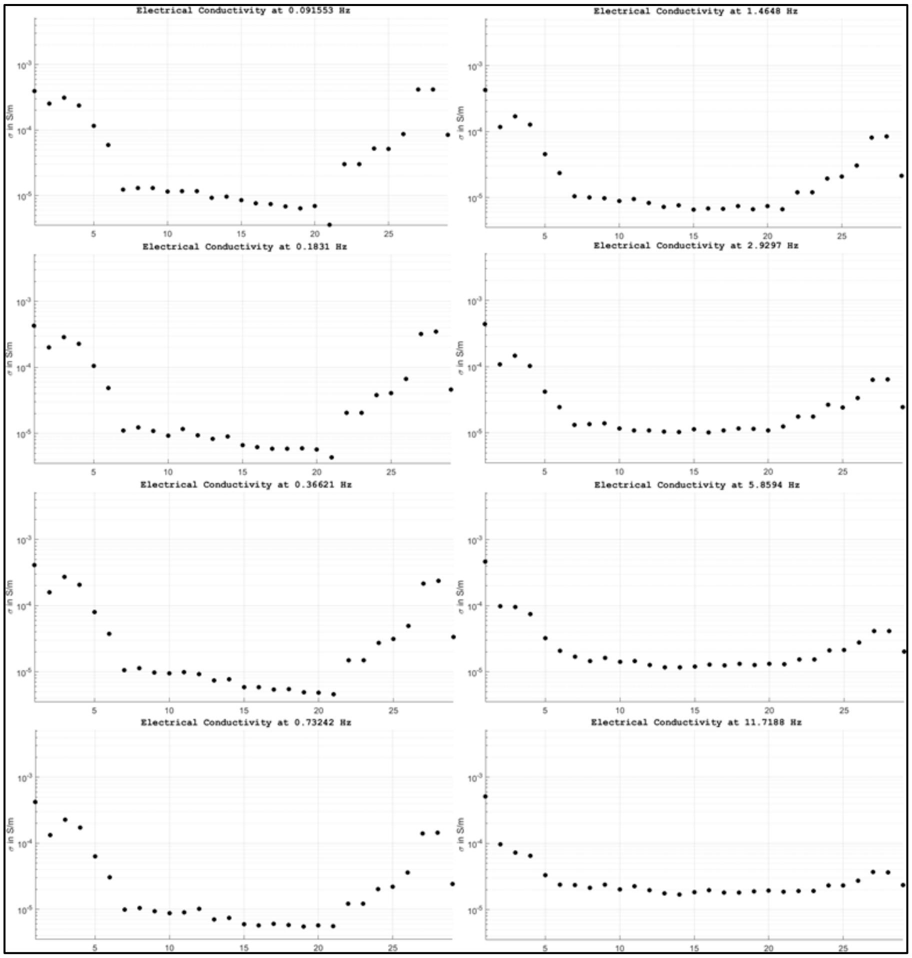

Figure 74: Real electrical conductivity for all 29 experimental stages, shown for 8 frequencies between 0.09 Hz (upper left) and 11.7 Hz (lower right)

4. NMR studies

Integrating High-Field NMR, Low-Field NMR and MXCT Data

A collaborative effort between Carolyn Koh's hydrate group and Manika Prasad's rock physics group allowed us to combine seismic measurements with methane formation and dissociation in natural sediments. We adapted the high pressure synthesis apparatus developed by Gupta (2007) to measure the dissociation of methane hydrate in sediment systems (Figure 75).

The experiments (Gupta, 2007) show that methane formation and dissociation in natural sediments show distinct peaks for methane in different cages (Figure 76). The high-field NMR data show the decay of peaks due to methane in the large and small cages, and the increase in the methane gas peak (Figure 77). Similar variations were observed in low-field NMR and acoustic waveform data during dissociation of THF hydrates in sediments.

The adaptations included construction of a vessel to make larger methane-hydrate bearing sediment samples while performing acoustic, low-field NMR, and CT imaging during the formation and dissociation process (Figure 78 and Figure 79).

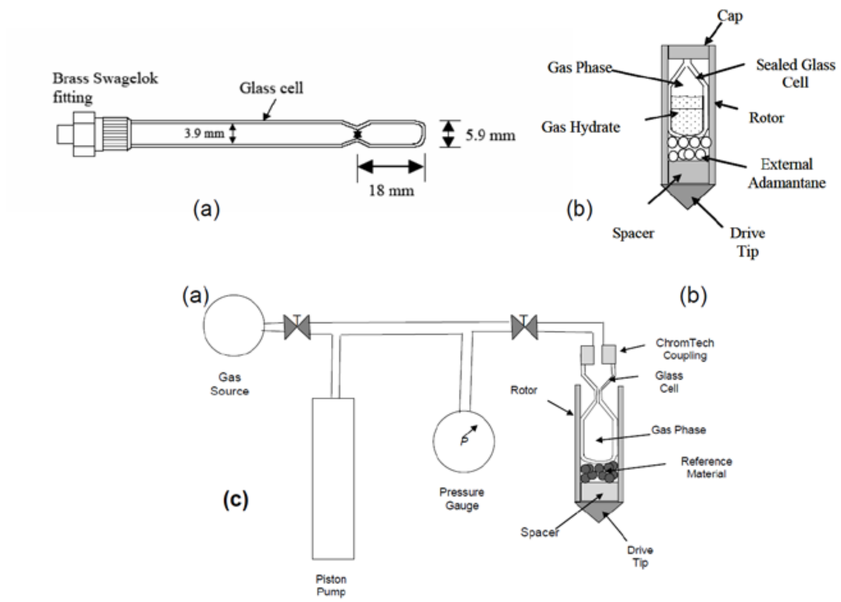

Figure 75. (a). The pyrex glass tube with a brass fitting used to prepare the NMR sample. (b). Zirconium rotor and sealed glass sample cell assembly. (c). Non-spinning sample cell connected to pressure gauge.

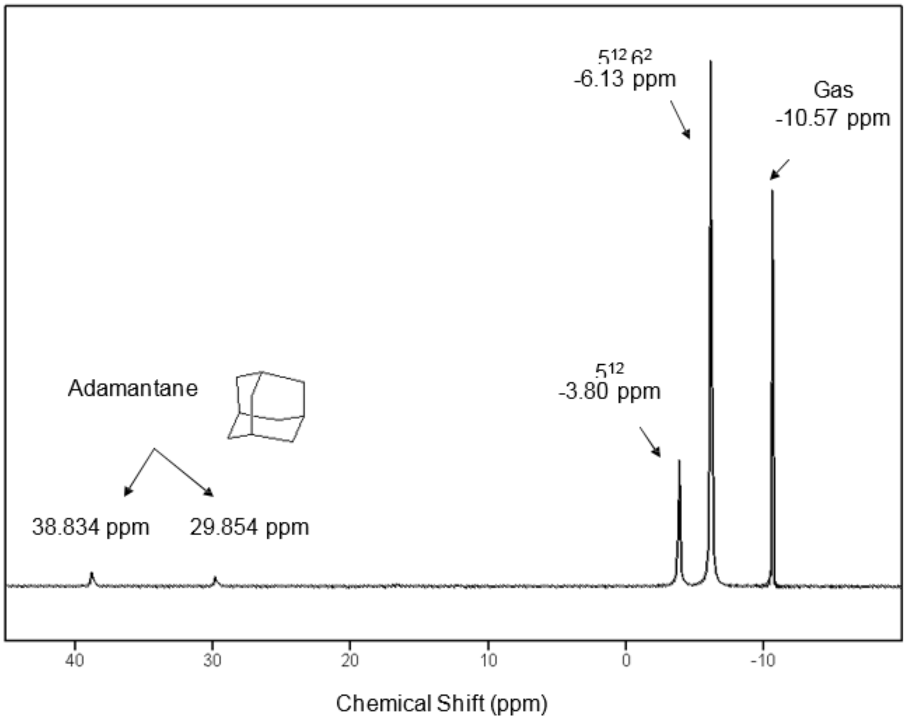

Figure 76. 13C methane hydrate NMR spectrum at 253 K.

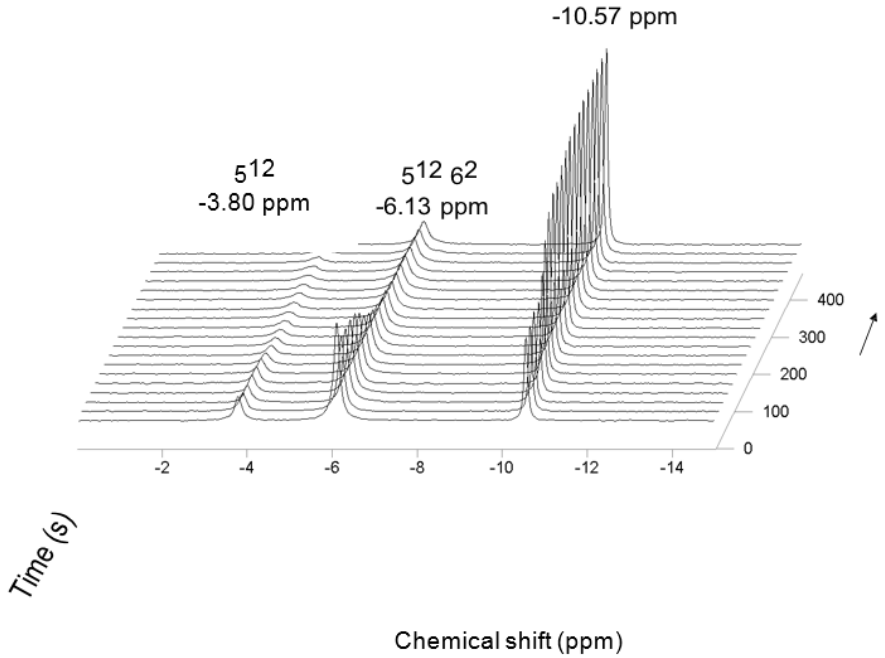

Figure 77. 100.5 MHz time-resolved 13C MAS NMR of sI methane hydrate dissociation during the temperature ramp from 269 K to 271 K. Time-resolution was 5.2048s but only every fifth spectrum is plotted here.

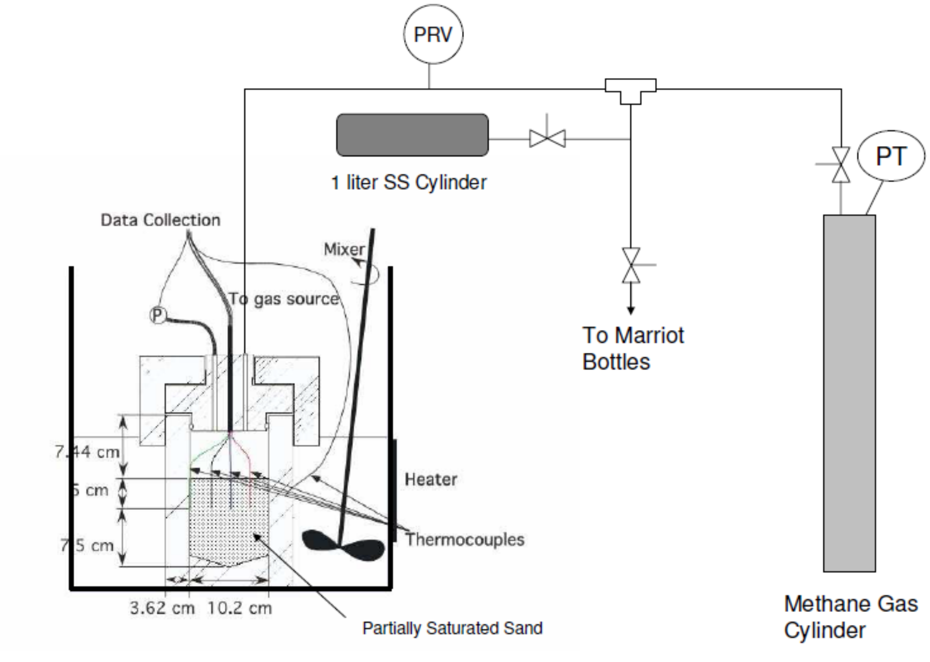

Figure 78. Pressure vessel and experimental setup.

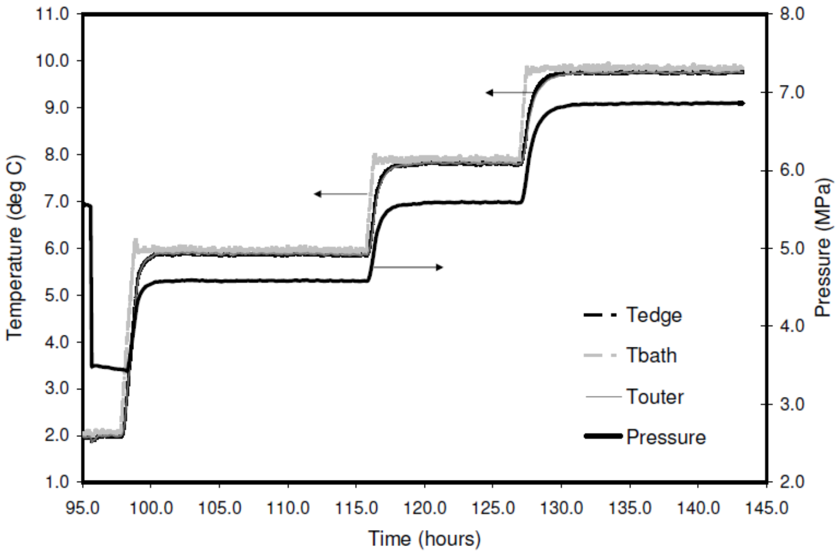

Figure 79.Pressure and temperature during temperature induced hydrate dissociation.

Measurements of Cyclopentane Hydrate Dissociation in NMR

Currently, Nuclear Magnetic Resonance (NMR) is available for classification of fluids in our laboratory. The NMR setup is a low-field 2 MHz Magritek NMR with a magnetic field of 0.05 Tesla. Transverse relaxation (T2) spectra are collected using CPMG sequences. The goal of this work was to record dissociation of a cyclopentane hydrate performed within the NMR in order to test for memory effect of hydrate formation. This was accomplished by first establishing an NMR reading for samples of pure liquid cyclopentane to capture the expected T2 response of these bulk fluids in their dissociated state (Figure 80).

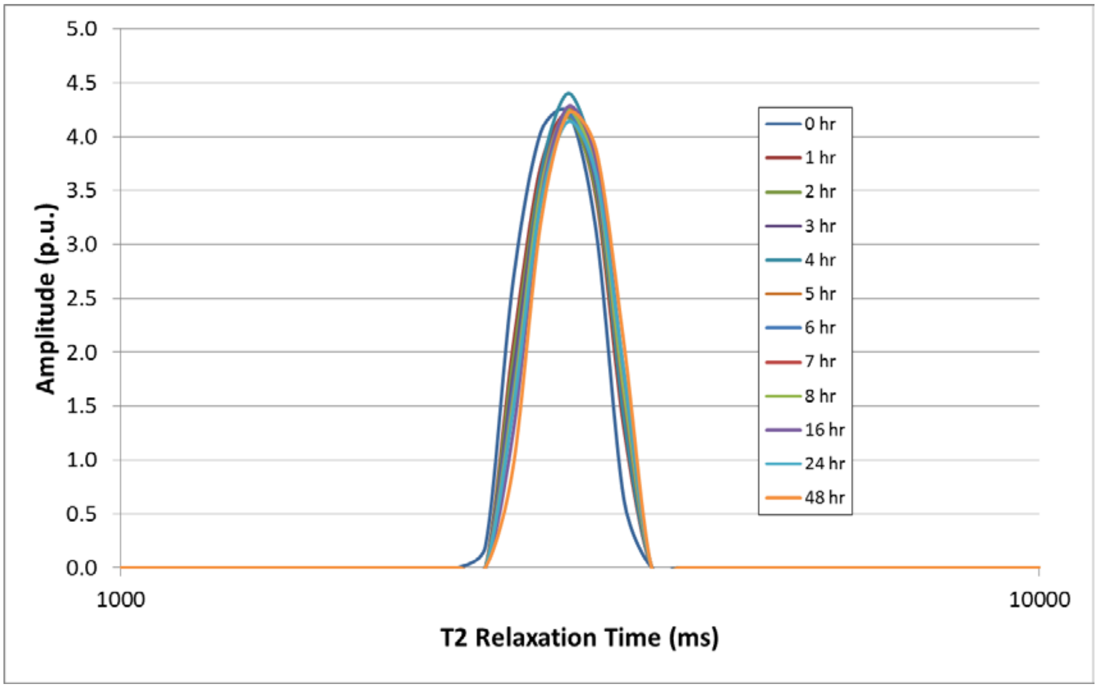

Figure 80: Collected T2 Spectra of liquid cyclopentane over 2 days to establish a baseline in NMR response for bulk cyclopentane fluid in our laboratory conditions.

Hydrate dissociation was then allowed to occur within a vacuum sealed vial of cyclopentane hydrate. A batch process of NMR experiments were collected at 15 minute intervals for an hour, followed by measurements performed at 1 hour intervals for the next 24 hours during dissociation of the hydrate species. Corresponding NMR spectra were then plotted to see respective changes in NMR response during this dissociation (Figure 81).

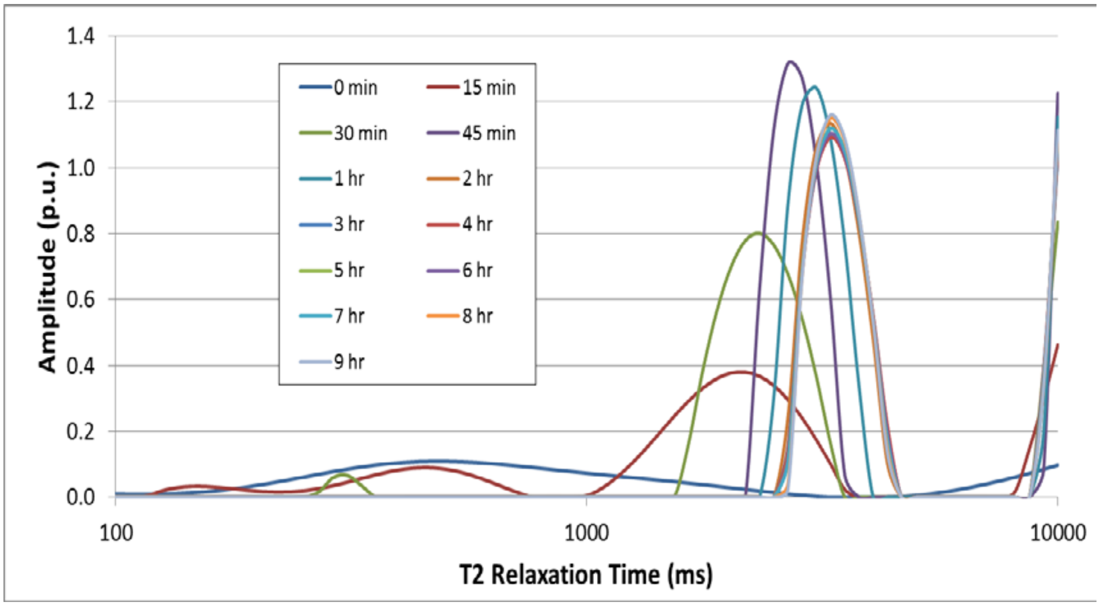

Figure 81: Collected T2 spectra of dissociating Cyclopentane hydrate in a vacuum sealed vial

Upon inversion of the raw T2 relaxation data, we observed that a relaxation peak in the time range greater than 8000 ms grew as the hydrate dissociated. This peak was not observed for the pure cyclopentane liquid sample T2 relaxation data at laboratory conditions which showed a relaxation peak at 3500ms as shown in Figure 80. The dissociated hydrate formed a meniscus between dissociated and undissociated hydrate in the sealed vial (Figure 82). We postulate that the partial pressure from cyclopentane hydrate dissociation might cause resonance at this fluid interface, contributing to the late time response of the NMR hydrate during dissociation.

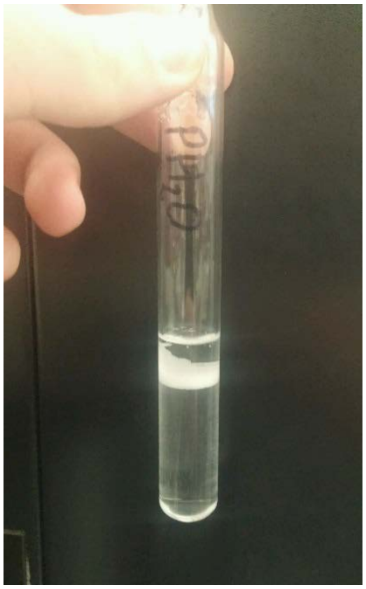

Figure 82: Partially dissociated cyclopentane hydrate. This stable condition is marked by the presence of an interface between two different fluids that might cause the late time responses in recorded NMR T2 spectra.

NMR experiments were then performed at hour intervals for the following 48 hours to record any subsequent change of NMR T2 spectra and to observe if any further dissociation was occurring (Figure 83). We observed that no changes have occurred in the recorded spectra for the partially dissociated, yet stable cyclopentane hydrate. Further studies might explain the causes for this late time response in NMR T2 spectra.

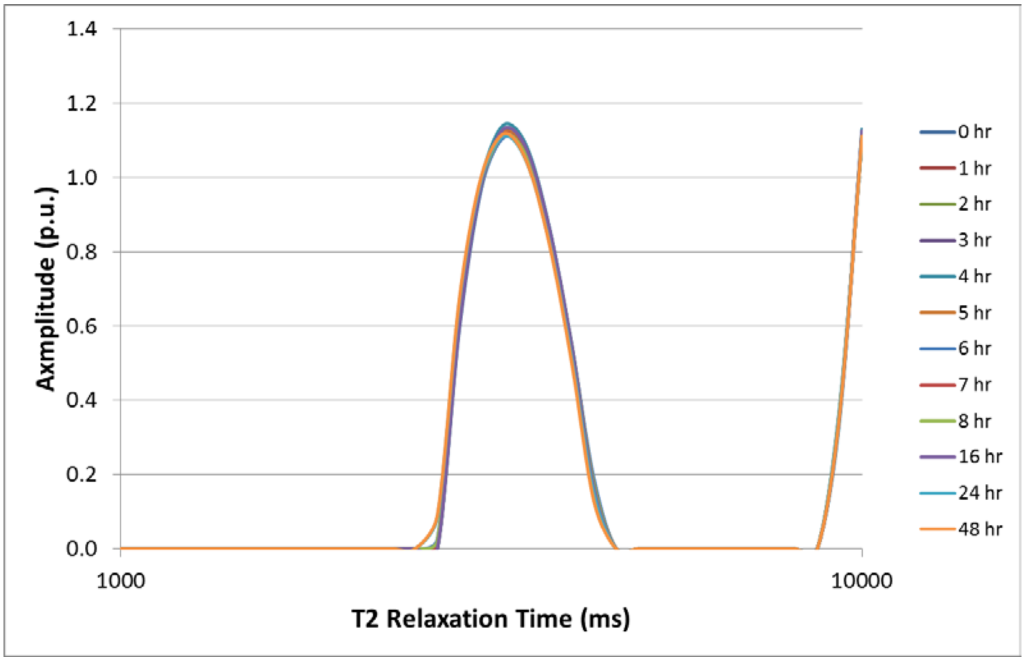

Figure 83: Stable NMR T2 spectra for stable partially dissociated cyclopentane hydrate. The late time peak is believed to be caused by resonance between fluid interfaces, but has not been verified.

Detecting Free Water with NMR T2 Relaxations

As noted previously, the development and calibration of hydrate models relies critically on the knowledge of the content of the pore space. Even small amounts of liquid or gas will have a major impact on the elastic properties. Hence, Nuclear Magnetic Resonance measurements are now being employed to characterize samples.

To initiate our investigation, we measured different types of pure fluids. First of all, we measured pure THF and the inversion results for the spectrum show that THF itself has a very strong signature in NMR measurements. Next we measured the used THF-Water mixture and when we compare it with the pure THF we can see a drop in amplitude and a faster relaxation time (a shift to the left can be seen). In Figure 84 we can see the average echo amplitudes over time recorded for THF, THF-water, and the three THF-hydrate bearing measurements.

First of all, we can see that THF signal needs a much longer time to come to zero compared to all the other samples which means the relaxation for THF compared for all the other measurements is longer. Also, when we look at the three THF-hydrate samples we can see that with increasing dissociation the amplitudes increase which are in a direct relation to the volume of fluid in the sample.

The used THF-Water ratio would, in theory, result in a 100 % THF-hydrate conversion. The reason behind these measurements was to see if we can see residual water or even residual THF within the 100 % THF-hydrate samples. If we are able to pick up a water signal during our experiments we know that not all of water and THF was converted into hydrates and we have small areas between the THF-hydrates where we have trapped water or even THF.

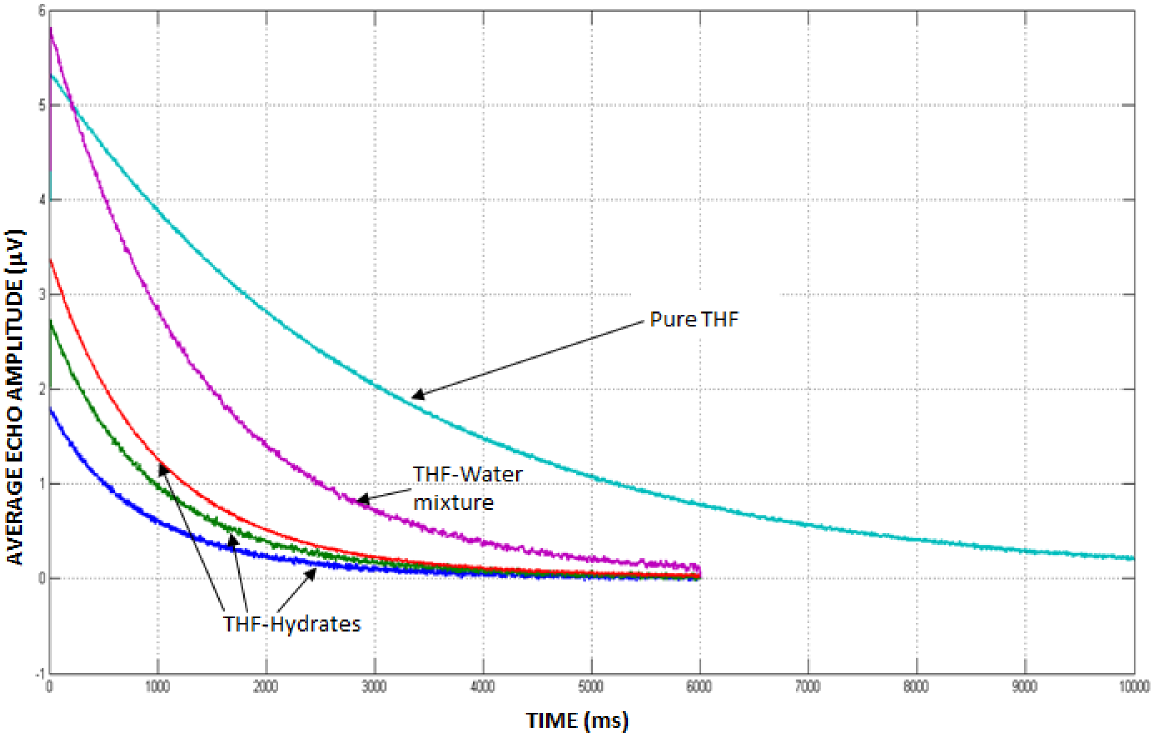

Figure 84: Raw NMR data for THF, THF-water mixtures, and various THF hydrate compounds.

Our first results for the measured hydrate bearing sample show that we have two distinguished peaks in the spectrum. The first measurement of pure THF-hydrate (see Figure 85, RED curve) shows that we have a relatively small amplitude at around 1 sec and another small peak with almost the same amplitude just below 1 ms. In our interpretation the first peak could be the signature of water that is being trapped between the THF-Hydrate crystals. The fast relaxation time can be explained by the fact that the water is in very tiny “pores” and therefore trapped which results in a fast relaxation. The second peak could already be a THF-water mixture. It was observed that the THF hydrates started to dissociate right when they were taking out of the cooling bath. Even though we put them in a cooled container to transport them to the NMR machine, a small liquid phase started to build up.

The result for the light blue line was obtained from the same sample but at a later time (3 min after the first run was done). As we can see the first peak loses amplitude whereas the second one increases in amplitude. This could be simply a result of the dissociation process itself. The THF-hydrate continues to dissociate therefore less water is trapped in between the crystals and we have more THF-water mixture.

The purple line shows the results for a measurement performed after the light blue measurement (5 min after). Again the dissociation process continues which results in a decrease in trapped water (first peak) and an increase in THF-water (second peak). Also we start to see a shift in the second peak toward the complete dissociated sample mentioned earlier. If we would have continued our experiments we would have expected to see a further decrease for the first peak and a continuous increase and shift of the second peak. In the case that all of the THF-hydrates would have dissociated that sample should have looked like the result of the THF-water mixture.

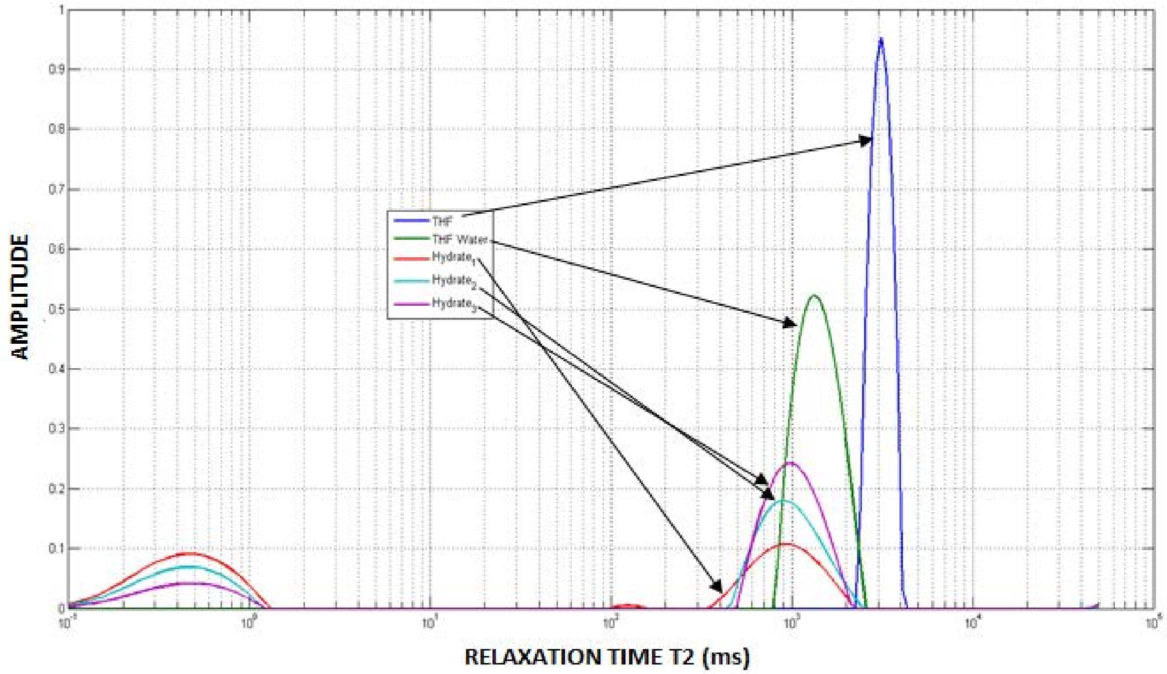

Figure 85. Derived T2 relaxation times for the THF mixtures and hydrate compounds.

NMR measurements are sensitive to free hydrogen. NMR measurements can be used to characterize the residual fluid in the samples because water as well as THF contain hydrogen. Samples were prepared in the same manner as for the ultrasonic measurements. A water to THF ratio of 81:19 wt% was used to form 100 % THF hydrates. The mixture was filled into small ampullae, put into a cooling bath, and slowly brought down to 1 °C by decreasing the temperature. After hydrate formation, a sample was put into the NMR and measured. As it can be seen in Figure 86 the raw data of the first run shows a small amplitude below 500 ms in the relaxation time. Figure 87 shows the inversion of the raw data from the first run (black line). No distinct peak can be examined. Figure 87 also shows an inversion for the same sample at a later stage. In this inversion we can see one peak which is THF-water. The measurements were not performed under temperature controlled conditions. Therefore the hydrates started to dissolve and with continuously measuring the sample we were able to “watch” the hydrates dissociate in the NMR data.

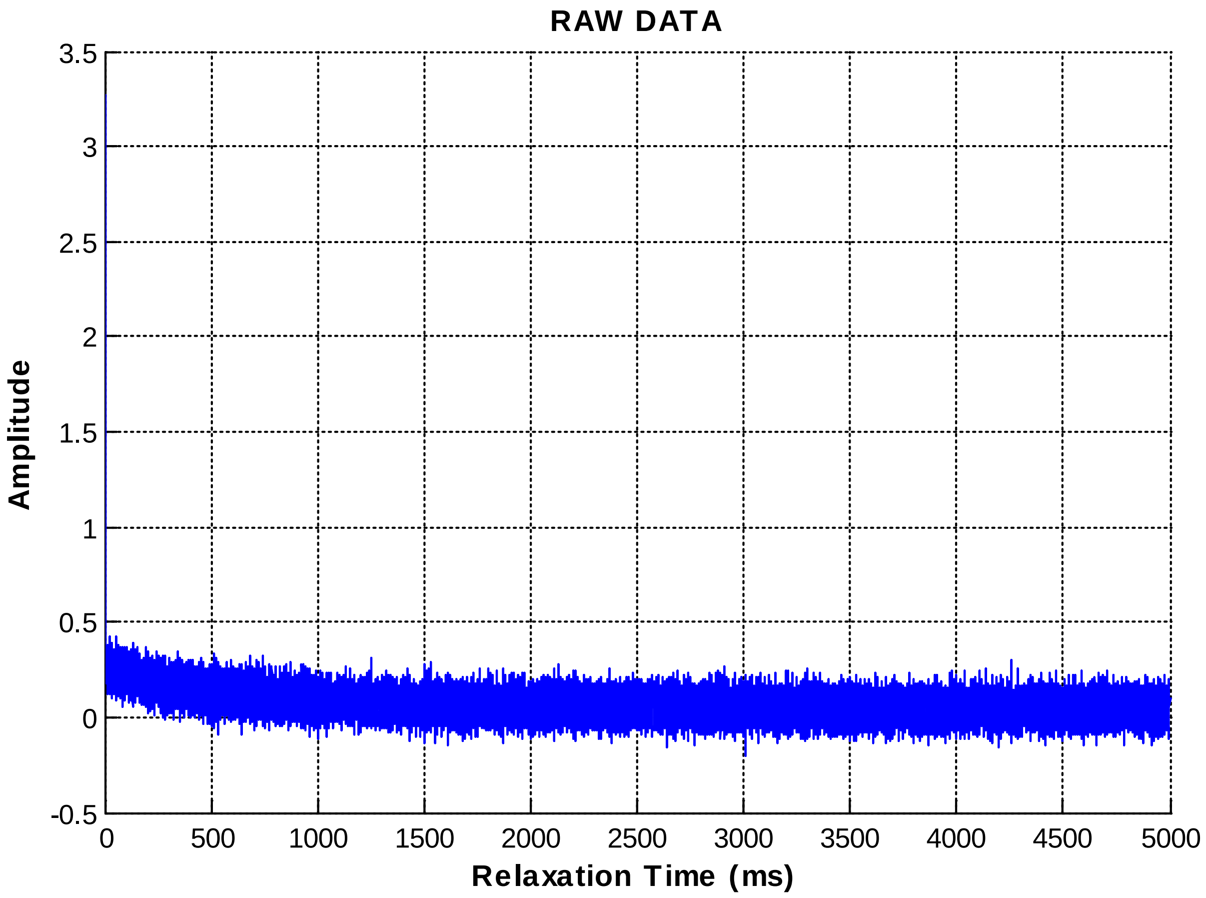

Figure 86: Relaxation Time for the First Run of a sample containing “100%” THF Hydrate at 1 °C.

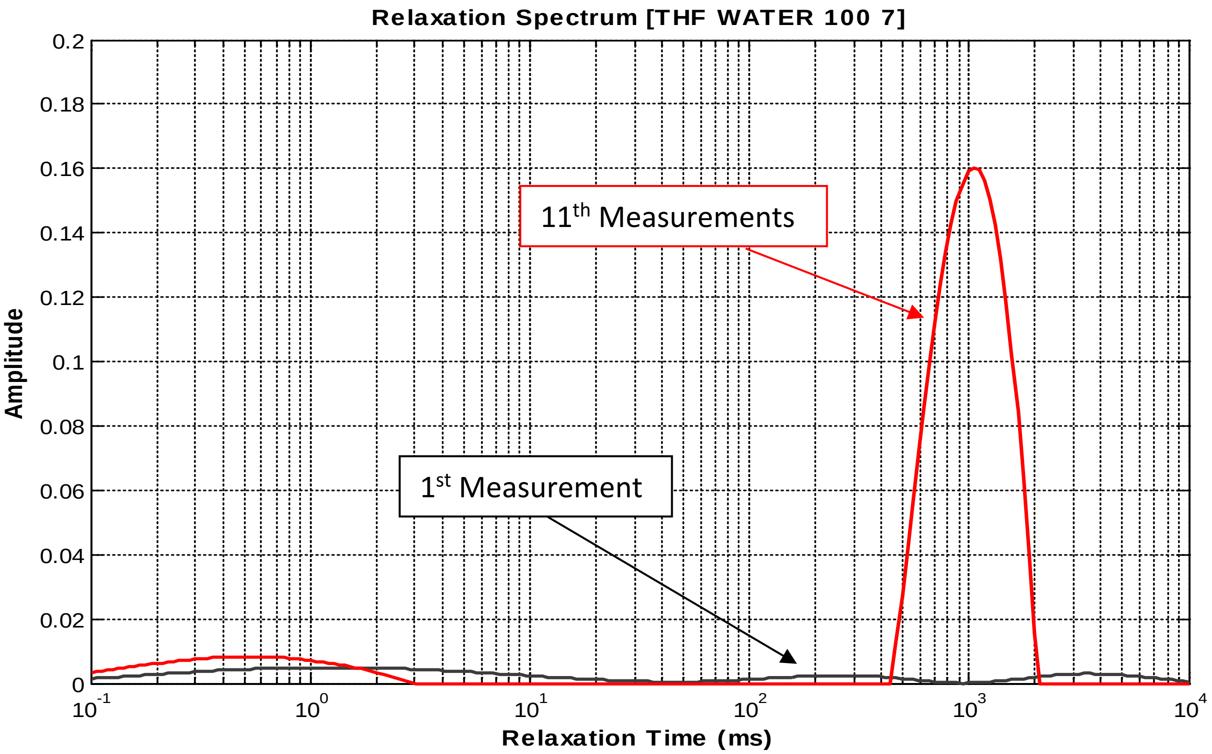

Figure 87: Inversion of a sample containing "100 %" THF hydrate. Comparison of the First Run at 1 °C with a measurement performed later after hydrates started to dissolve.

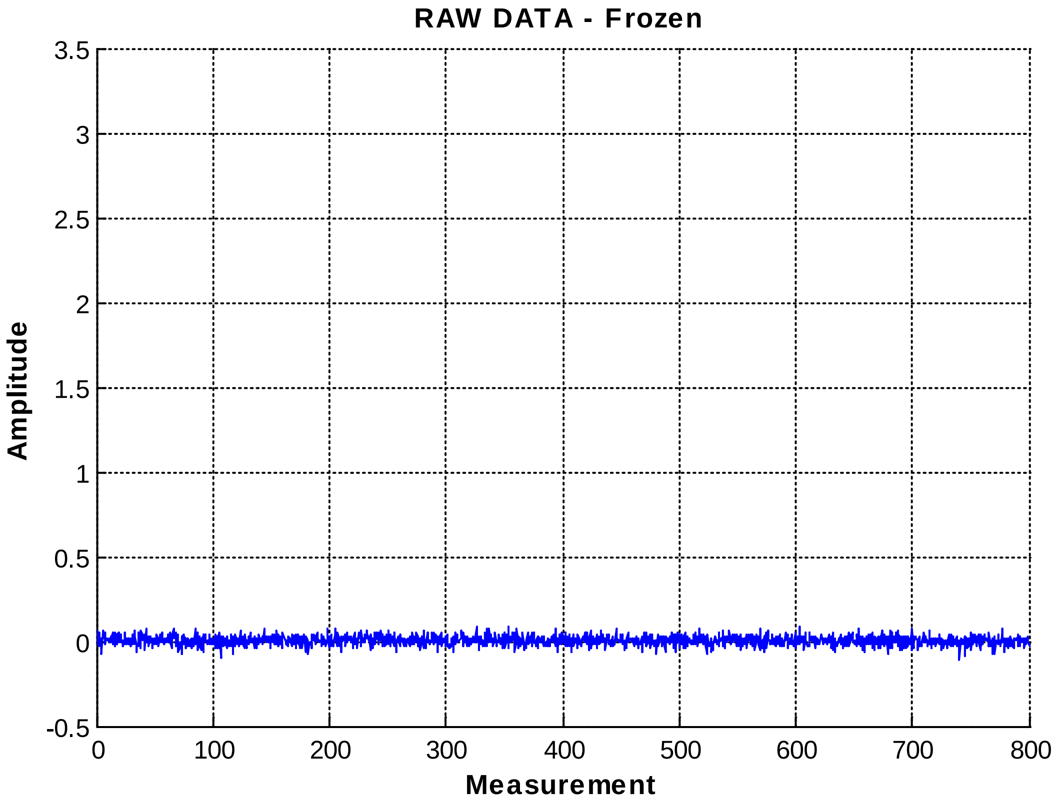

Figure 88: Relaxation Time for the First Run of a sample containing "100%" THF Hydrate at -10 °C.

Next we cooled the NMR samples down to -10 °C to freeze any residual water and we repeated our measurements. By looking at the raw data (Figure 88) we can see that the NMR does not detect any free hydrogen. The NMR T2 relaxation detection of free water provide the explanation for elevated attenuation in the hydrate sample that is missing in the frozen and the liquid hydrate samples (Figure 89).

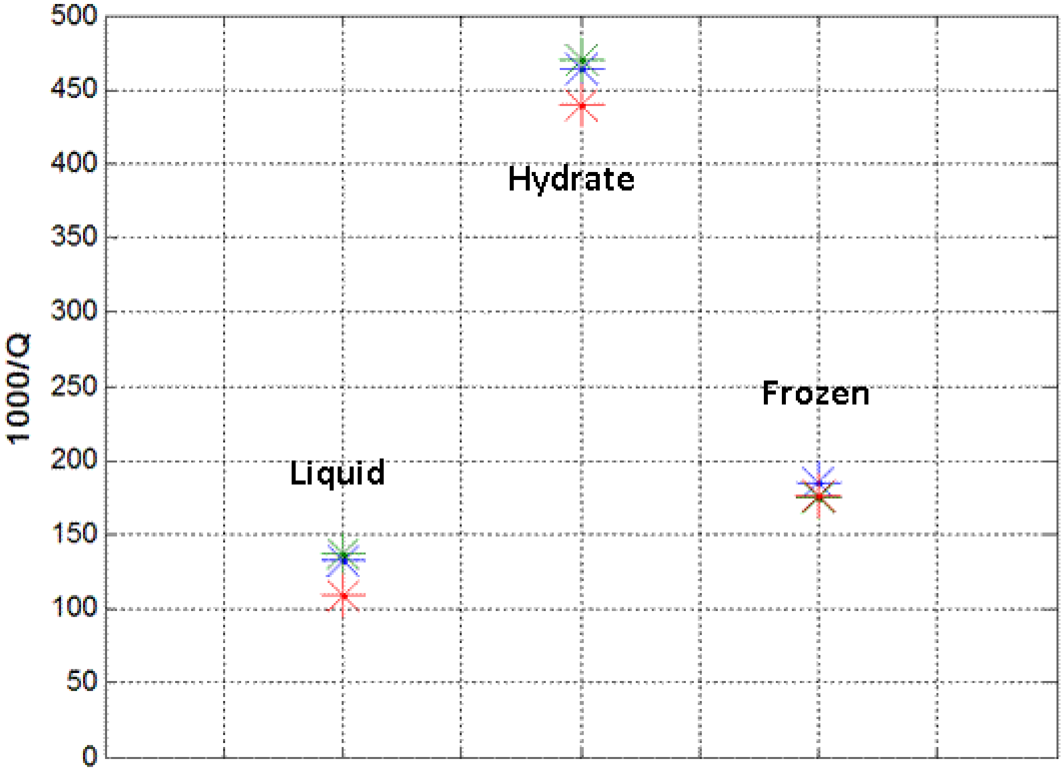

Figure 89: Overview of the calculated attenuation Q for the liquid, hydrate and frozen samples.

5. Theoretical Models

Pore Scale Distribution Models

Theoretical models correlate different pore-scale hydrate distributions and their impact on ultrasonic velocities. One such model is the effective medium theory which was applied to hydrate-bearing sediments by Ecker et al. (1998) and Helgerud et al. (1999).

For reference, Figure 90 shows the four different pore-scale distributions according to the effective medium model for hydrates in sediment: contact cementing, envelope cementing, pore filling and load bearing. The envelope cementing model shows a drastic increase in ultrasonic velocities even for small amounts of hydrate in the pore space whereas hydrate formed according to the pore filling model shows a much smaller influence on the ultrasonic velocities. Hydrate formation from free gas appear to create grain-cementing hydrate (Ecker et al., 1998). Hydrate formed from gas dissolved in water seems to have little or no contact with the sediment grains (Rydzy and Batzle, 2011).

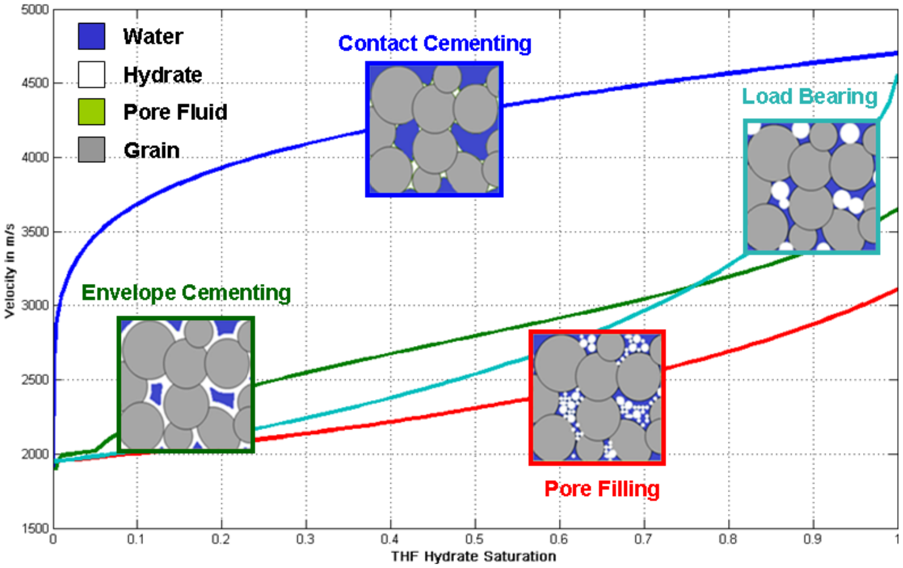

Figure 90: Effective medium theory after Ecker et al. 1998, modified by Helgerud et al., 1999: different distributions of hydrate in the pore space and their influence on ultrasonic velocities, conceptual figures from Rydzy and Batzle, 2011

Including salt (BaCl2) precipitate in effective medium models

A change in the cooling system in the MXCT scanner provided better temperature control. We froze the THF-hydrate bearing samples to -20°C and cooled them with dry ice during the scanning process. With this experimental procedure we observed the precipitation of barium chloride salt which was added to the samples for density contrast. The salt precipitate was expected since the residual pore water which was not consumed for hydrate formation was frozen thus excluding the barium chloride.

A new cooling system (Figure 91) allowed us to keep the sample temperature above 0°C to avoid freezing of the residual pore water. We expected to see two phases in the pore space: THF hydrate and barium chloride brine. Yet, so far all our MXCT images show the precipitation of barium chloride even at low salinities (e.g. 3.2 wt% barium chloride at the beginning of the experiment, increasing to 12.3 wt% after consumption of most water for hydrate formation; the maximum salinity for barium chloride is 23.3 wt%). An example image for a THF-hydrate bearing glass bead sample with barium chloride precipitate is shown in Figure 92. Due to this observation, it becomes necessary to include barium chloride precipitate in the effective medium models for hydrate-bearing porous media.

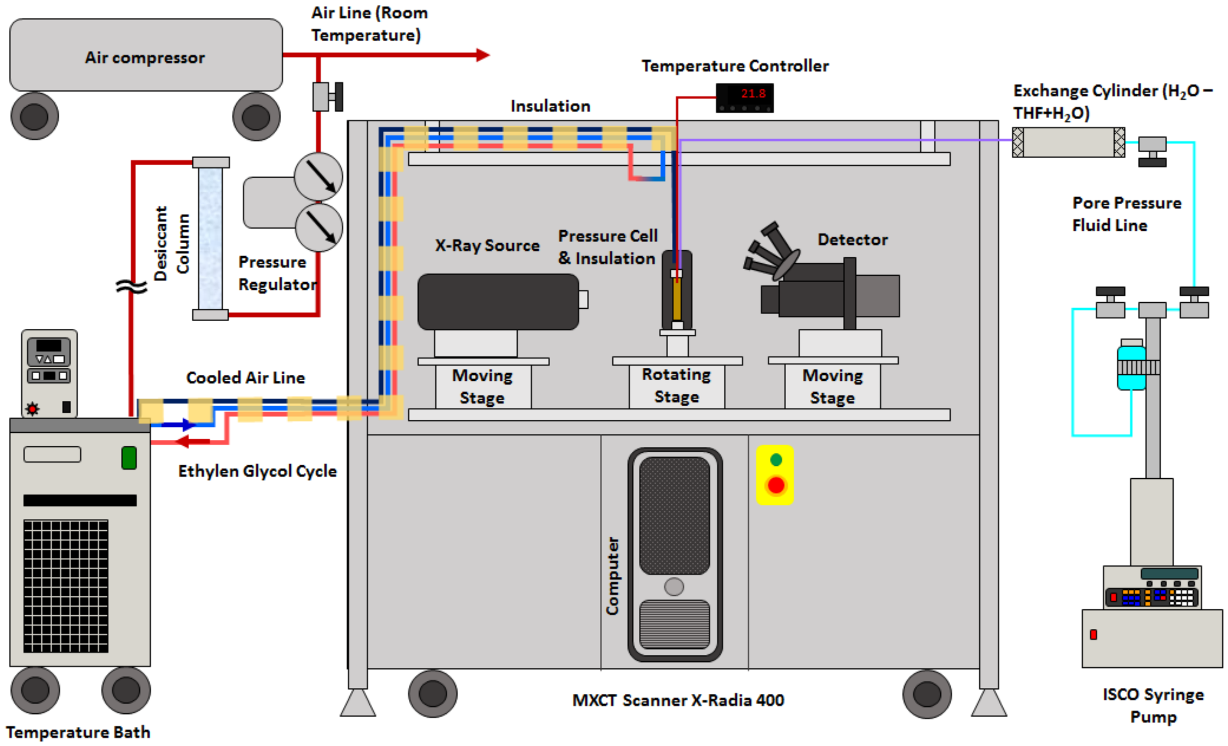

Figure 91: Experimental setup for hydrate experiments in MXCT scanner

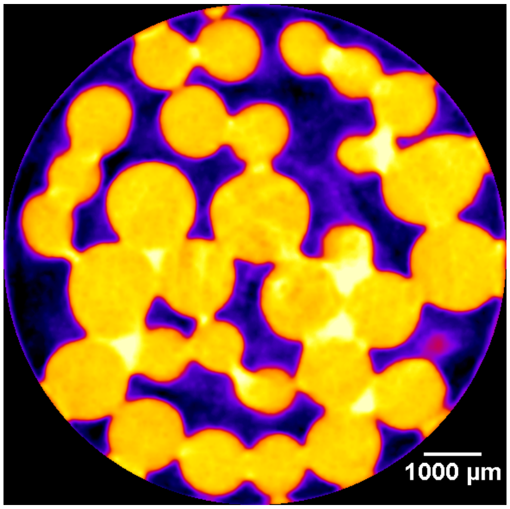

Figure 92: MXCT image at 0.5X resolution (1 pixel = 14.9 µm). Filename: CT_vessel_GB_THF_4. Violet/black: THF hydrate, pink: $BaCl_2$ brine, yellow/orange: glass beads, light yellow: $BaCl_2$ precipitate.

Figure 93 and Figure 94 show the modified models with experimental data. The models are effective medium models for hydrate-bearing sediments developed by Ecker et al. (1998) and Helgerud et al. (1999). The data points show ultrasonic P-wave velocities measured on THF-hydrate bearing glass-bead packs with added barium chloride. The ultrasonic velocity measurements have been described in detail in report Q4.

We included the barium chloride salt as a contact-cementing component together with pore-filling THF hydrate. The pore-filling hydrate model was chosen for the modification since our MXCT images suggest that the hydrate is pore filling. The model with pore-filling THF hydrate and contact-cementing barium chloride fits both P-wave and S-wave velocities well. It should be notes though that the chosen barium chloride concentrations are lower than what we observed in the MXCT images. The MXCT images suggest that 5-7 vol% of the pore space are filled with barium chloride for samples with 60% and 80% hydrate saturation. However, for the model we used barium chloride concentrations of 0.01% (at 0% hydrate saturation) linearly increasing to 1% (at 100% hydrate saturation). This discrepancy indicates that barium chloride may not behave exactly as described by the contact-cementing effective medium model. It is possible that we are dealing with a mixture of barium chloride brine and precipitated barium chloride. Further, the effective medium theory makes the assumption of a homogeneous distribution of each model component throughout the sample (Dvorkin et al., 1999). This assumption is clearly violated in case of barium chloride. Figure 92 shows that barium chloride is distributed patchy: filling entire small pores in some areas while not being present at all in other areas.

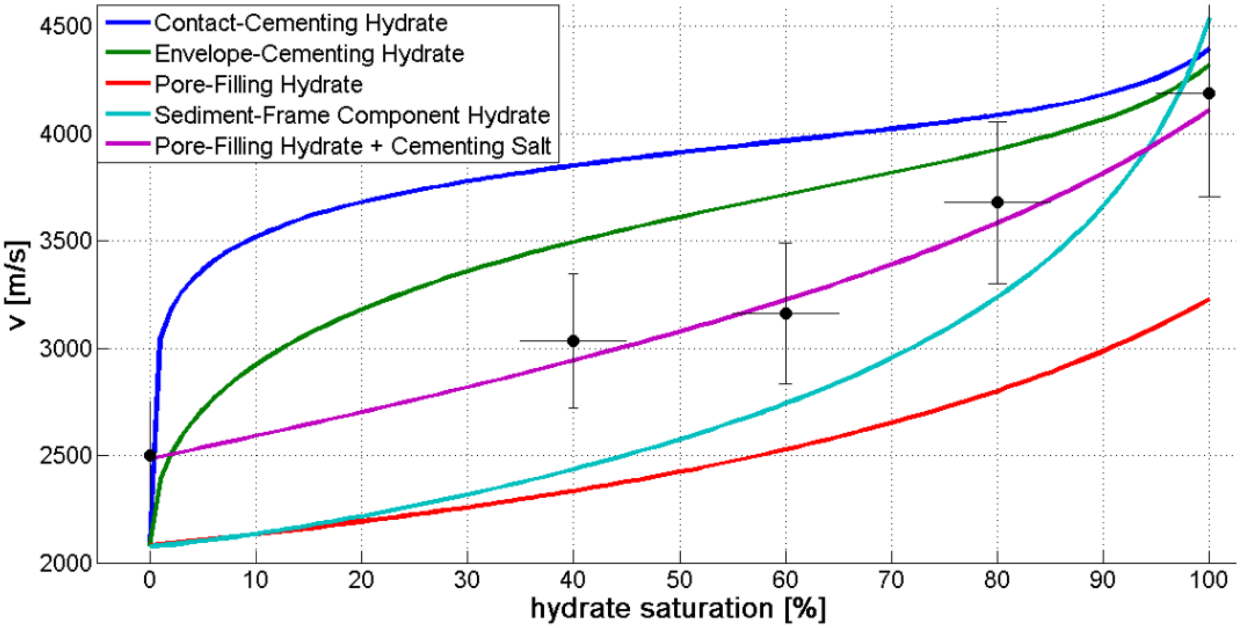

Figure 93: Effective medium models for hydrate-bearing sediments after Ecker et al. (1998) and Helgerud et al. (1999), P-wave. Experimental data shows ultrasonic velocities of THF-hydrate bearing glass-bead packs with initial salt concentration of 5 wt% $BaCl_2$

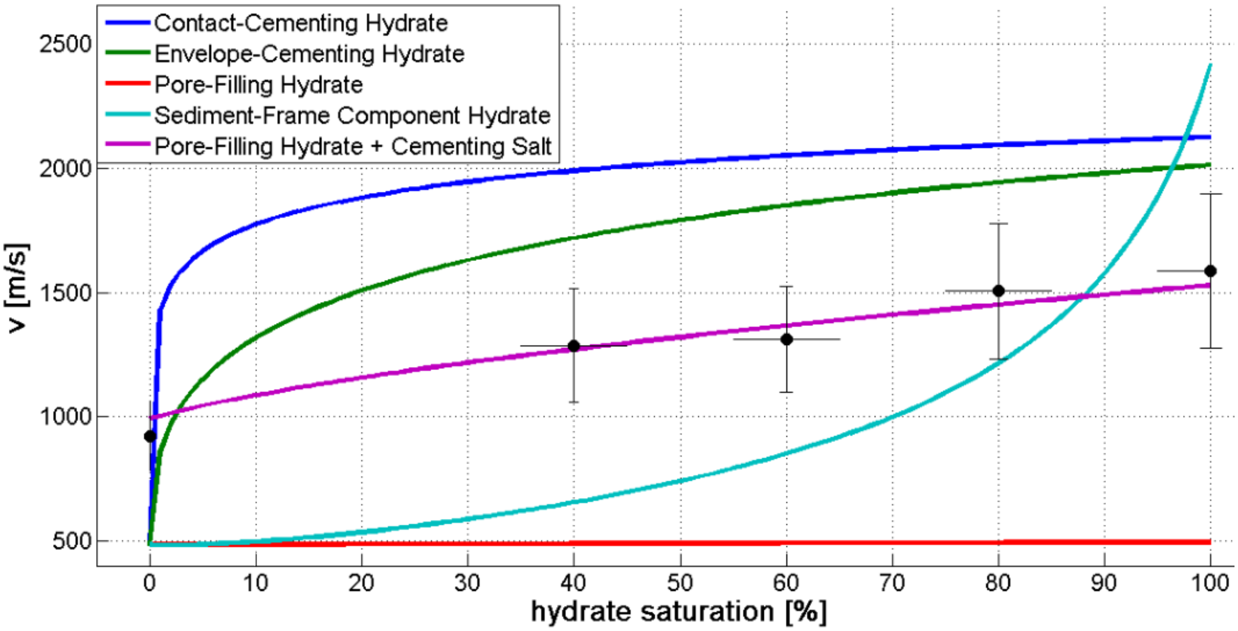

Figure 94: Effective medium models for hydrate-bearing sediments after Ecker et al. (1998) and Helgerud et al. (1999), S-wave. Experimental data shows ultrasonic velocities of THF-hydrate bearing glass-bead packs with initial salt concentration of 5 wt% $BaCl_2$

Our MXCT images have shown that barium chloride is precipitated at concentrations well below the maximum concentration of 23.3 wt%. There may be reasons why barium chloride precipitates at such low concentrations. For example, pockets of residual brine are separated from the rest of the pore space during hydrate formation. Thus, most water may be consumed to form hydrates in most of the pores, pockets with less water consumption might lead to differences in salt concentration. Low concentrations of barium chloride precipitate as a contact-cementing component helps to explain observations in our ultrasonic velocity measurements. Note that salt precipitation in natural occurring hydrate-bearing sediments is rather unlikely due to high flux of pore water; it must be taken into consideration for interpretation of laboratory experiments.

Phase Behavior CH_4 – CO_2 – H_2O system

Thermodynamic modelling provides us with the equilibrium phases at various pressures and temperatures. As is well known, in a water-methane system, will be stable at low temperatures and high pressures. In the more complex CH4 – CO2 – H2O system, the stable region for hydrates are modified as well as the composition. Figure 95 shows the stability regions for mixtures of methane and carbon dioxide. Very small amounts of carbon dioxide (0.5 mole %) will have very little influence (Figure 96).

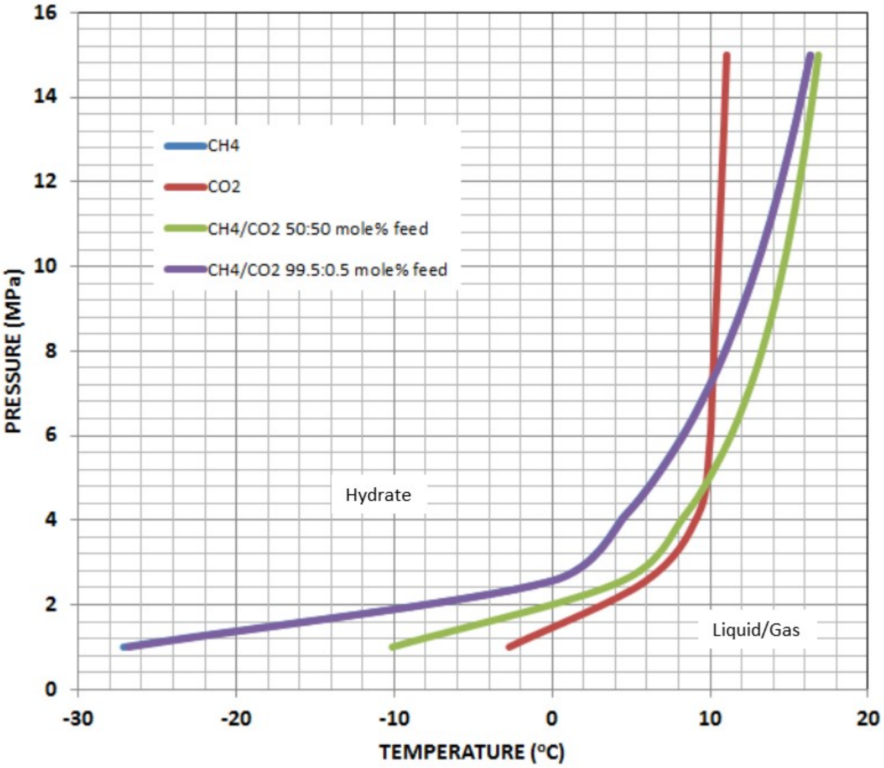

Figure 95: Extended phase relationships for the CH4 – CO2 – H2O system: Blue: CH4 – H2O, Red: CO2 – H2O, Green: 50-50 mixture of CH4 – CO2, Purple: CH4 with small amount of CO2. Note: blue and purple lines almost coincide.

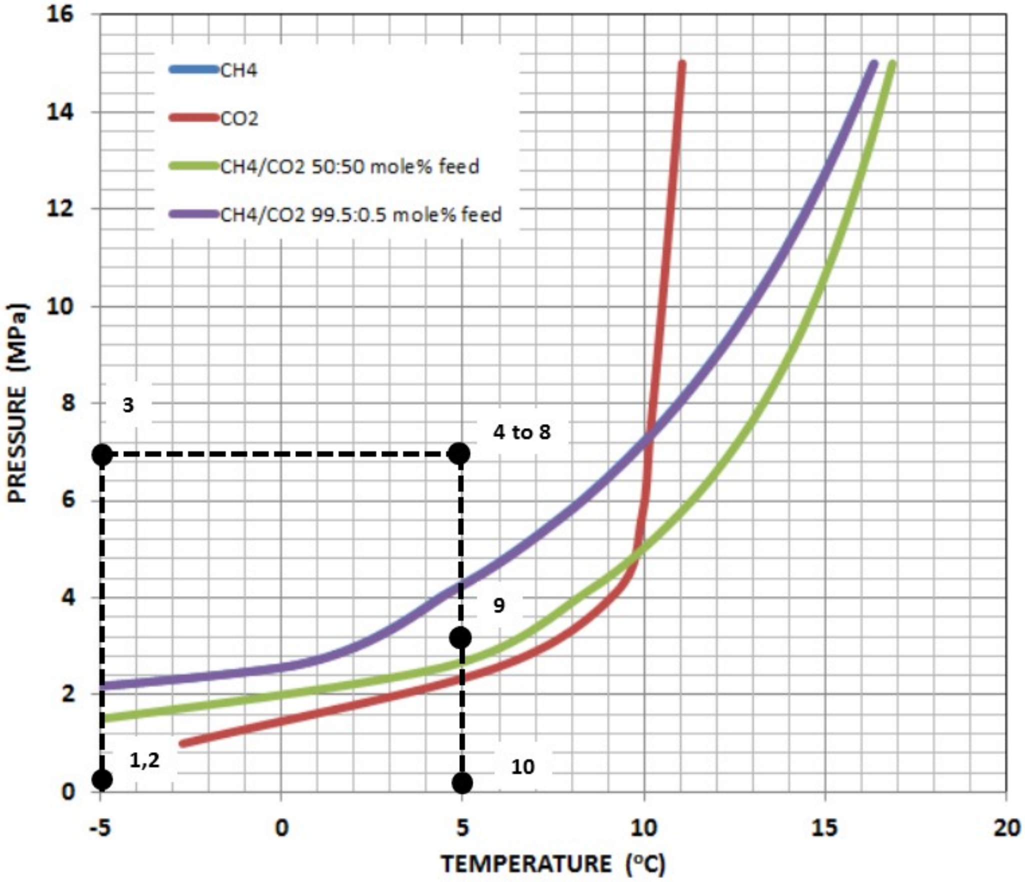

Figure 96. Similar calculations as in Figure 95, but expanded in the near-room temperature region. Dashed line and numbers refer to a proposed experimental path (see text).

These phase calculations allow us to design our various experimental strategies. As an example of a planned procedure:

1. Crushed ice cooled in vessel to – 5°C
2. Vessel vacuumed to remove air
3. Vessel pressure raised to 6.9 MPa (1000 psi) with CH_4
4. Temperature raised to + 5 °C
5. Sample resides for several hours (CH_4 intake monitored)
6. Sample taken to test hydrate transformation
7. Methane evacuated from vessel
8. CO_2 flooded into vessel at about 3 MPa
9. Gas periodically tested for composition
10. Sample extracted and tested for conversion to CO_2 hydrate

As indicated by this proposed procedure, phase equilibrium pressure and temperature does not guarantee the formation of a particular phase. Agitation may be needed to speed conversions. Alternatively, NMR measurements are appropriate to ascertain if any free water exists in our grown hydrates. In general, we will need to employ several such techniques to quantify the actual phase distributions and compositions.

6. In situ (well Log) data:

Analyzing Well Log Data

Much of the data we use for comparison will be from the Mallik, Mount Elbert, and Ignik Sikumi wells provided to us by Tim Collett of the USGS. Guerin and Goldberg (2002, 2005) have examined some of these data and extracted attenuation estimates. Data from the Mount Elbert well is shown in Figure 97. This simple plot shows the sand-rich zones starting at 2015 and 2135 feet (track 1). High hydrate saturation can be inferred immediately from the strong resistivity (track 2) and sonic (track 3) response.

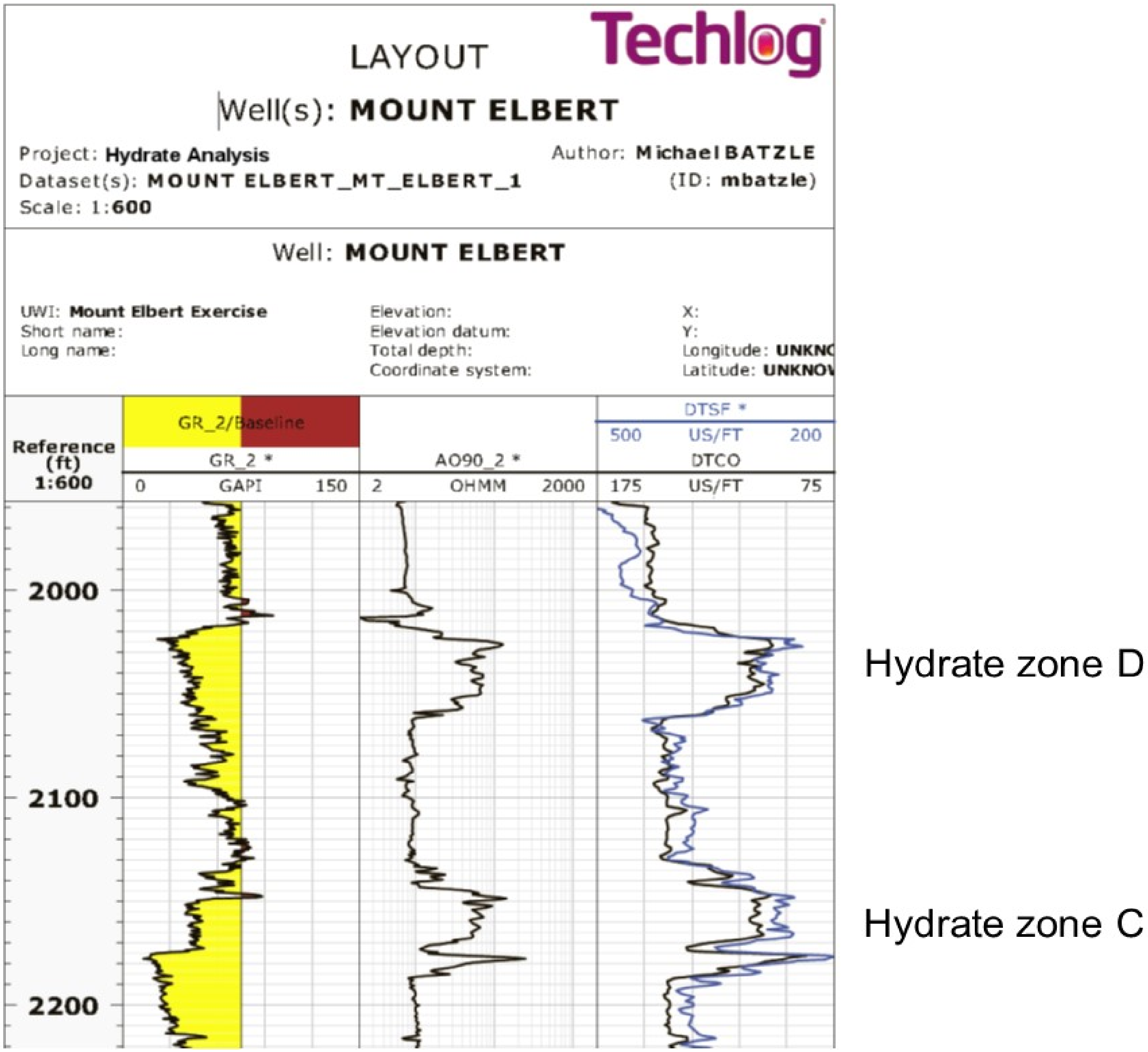

LAYOUT

Well(s): **MOUNT ELBERT**

Project: **Hydrate Analysis**
Dataset(s): **MOUNT ELBERT_MT_ELBERT_1**
Scale: 1:**600**

Author: **Michael BATZLE**
(ID: **mbatzle**)

Well: **MOUNT ELBERT**

UWI: **Mount Elbert Exercise**
Short name:
Long name:

Elevation:
Elevation datum:
Total depth:
Coordinate system:

X:
Y:
Longitude: **UNKNC**
Latitude: **UNKNO**

Figure 97: Gamma ray (GR), Resistivity (AO90), and Sonic (compressional – DTCO; and fast shear - DTSF) for the two prominent hydrate zones in the Mount Elbert well, Alaska. Data provided by Schlumberger.

The sensitivity of Nuclear Magnetic Resonance measurements (NMR) to free water makes the NMR log (here CMR) another valuable tool to quantify hydrate content (Figure 98). Collett and co-workers used these data, combined with other logs, to provide what they consider the most accurate estimate of hydrate saturation.

Lee and Collett (2011) use a composite poroelastic model to derive a similar hydrate saturation estimate from sonic logs (Figure 99). For exploration data sets, such detaied calibration is not possible. Velocity data (either from moveout analysis or inversions) is not sufficient. We are now working on extracting attenuation-related parameters from the in situ data. These results will be compared and calibrated against our laboratory measurements.

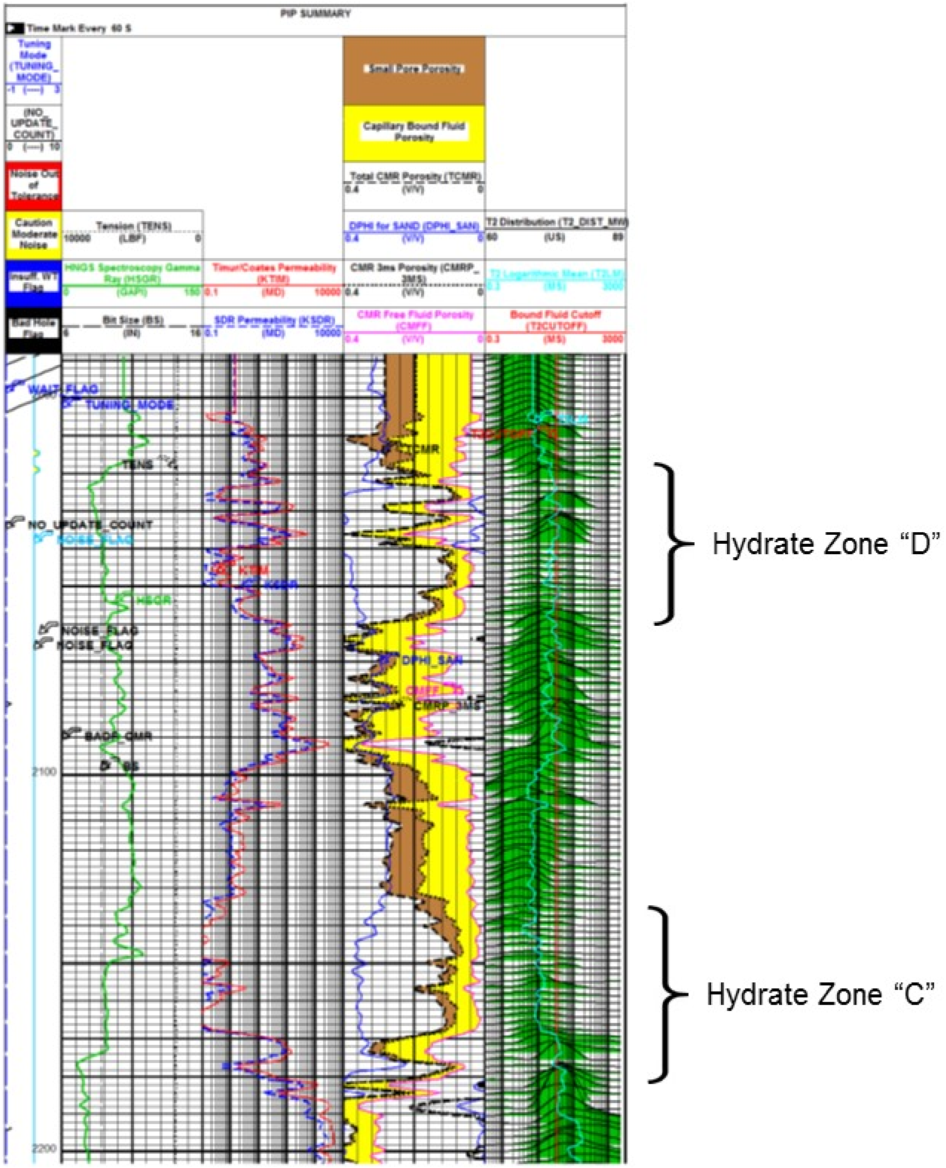

Figure 98: Magnetic Resonance log (CMR) in the Mount Elbert well used to identify the zones of high hydrate saturation. Data provided by Schlumberger and T. Collett.

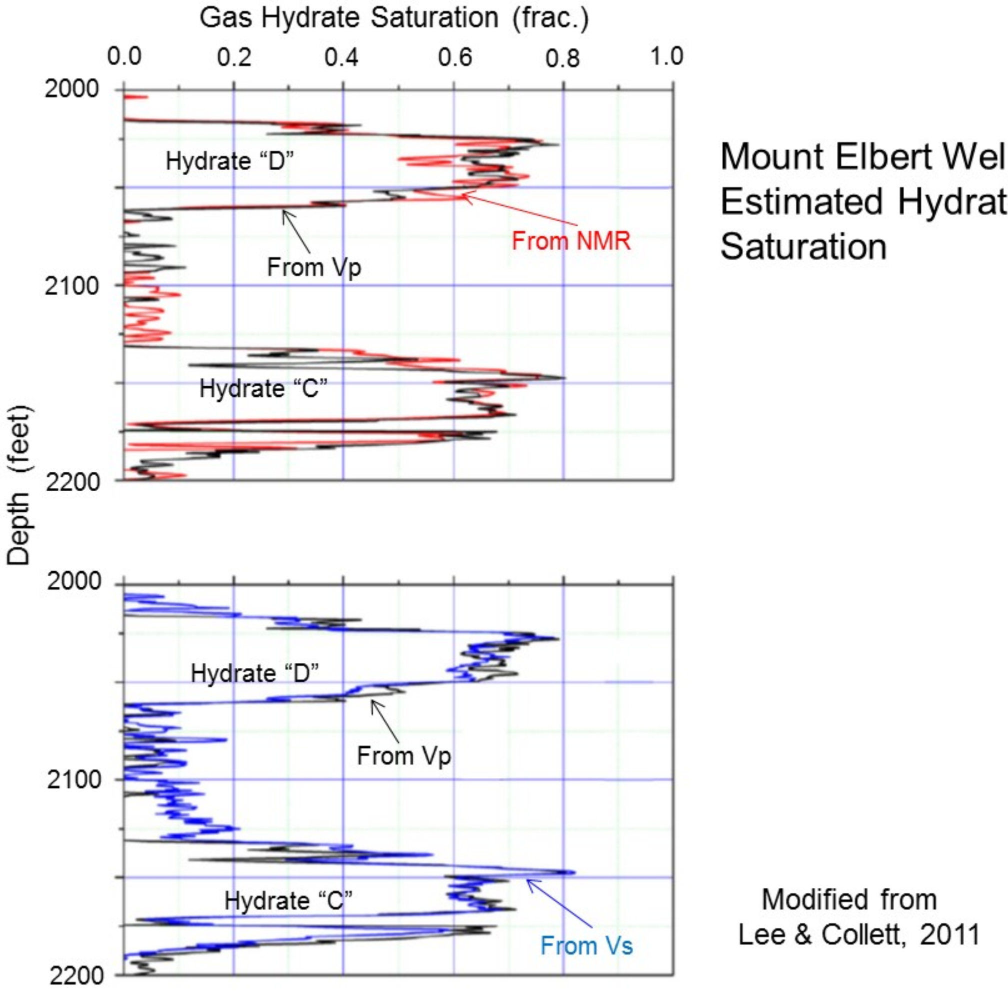

Figure 99: Estimated gas hydrate saturation in the Mount Elbert well using NMR (CMR), compressional wave speed (Vp), and shear wave speed (Vs).

Comparison of Well Log Data to Ultrasonic Velocities and Attenuation

As we reported in the last reports we investigated the ultrasonic attenuation of pure THF hydrates. To employ our previous finding we started to use our developed methods on well log data. The well log data was provided by Dr. Guerin from the JIP Gulf of Mexico gas hydrate research wells. In this report we are presenting preliminary results from well GC955H. A first look at the data shows the presence of hydrates. A drastic increase in velocities accompanied with a weaker signal can be seen in Figure 100. Blanking is usually observed right above the BSR in a zone where hydrates are present. This blanking is thought to be caused by an impedance factor close to zero which is caused by the presence of hydrates (Lee et all, 2009). Additionally, it has been observed that attenuation increases in the presence of hydrates. We started to perform an analysis of the waveforms by looking at the frequency shift due to attenuation (Figure 100). Four waveforms were chosen: one right above the hydrate bearing layer, two within the hydrate zone and one below the hydrate zone (Figure 101). It can be seen that the frequency content reduces within the hydrate layer. Also, the frequency contents increase in the waveform below the hydrate bearing zone, but it is still lower than the one right above the hydrate zone. This could possibly be due to the presence of free gas, which could cause a higher attenuation.

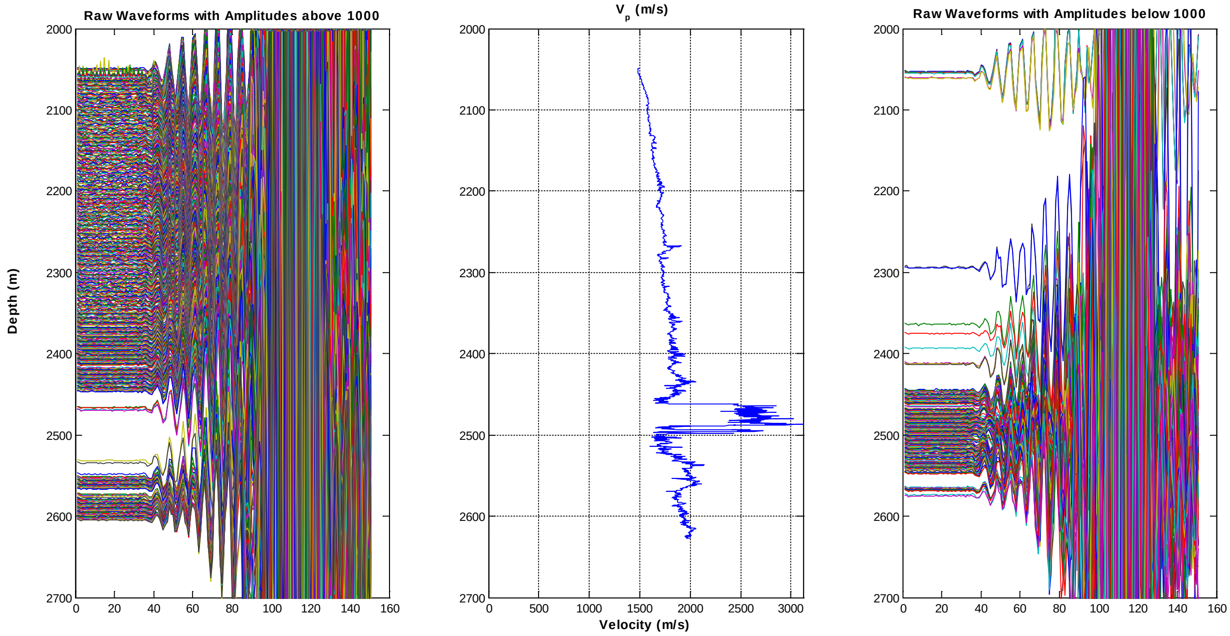

Figure 100. Raw waveform from well log data. (A) shows waveforms with amplitude values of above a 1000 and (C) shows the waveforms with amplitude values below a 1000. As it can be seen the waveforms with lower amplitude values show a correlation with the increase in velocities (B).

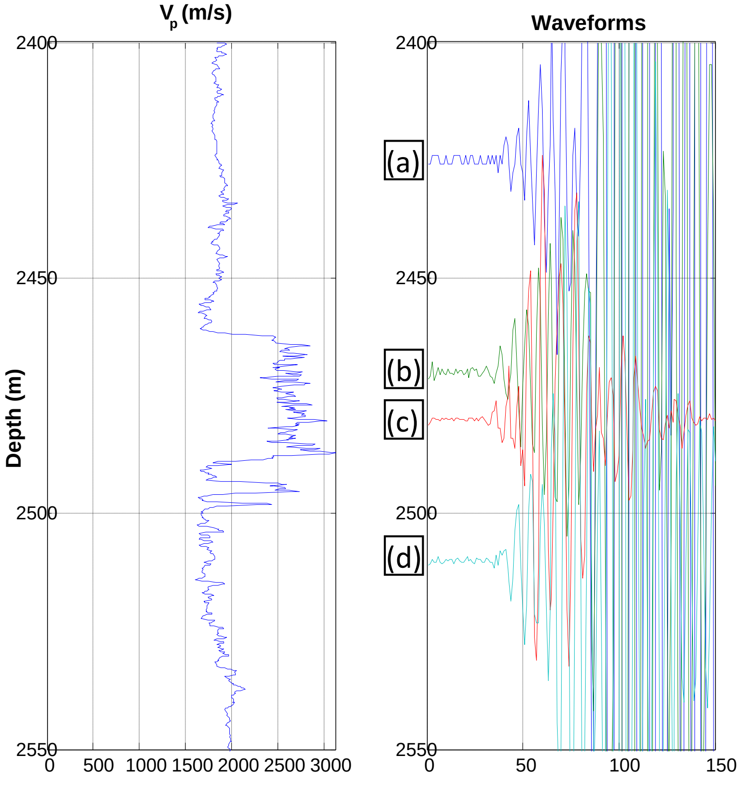

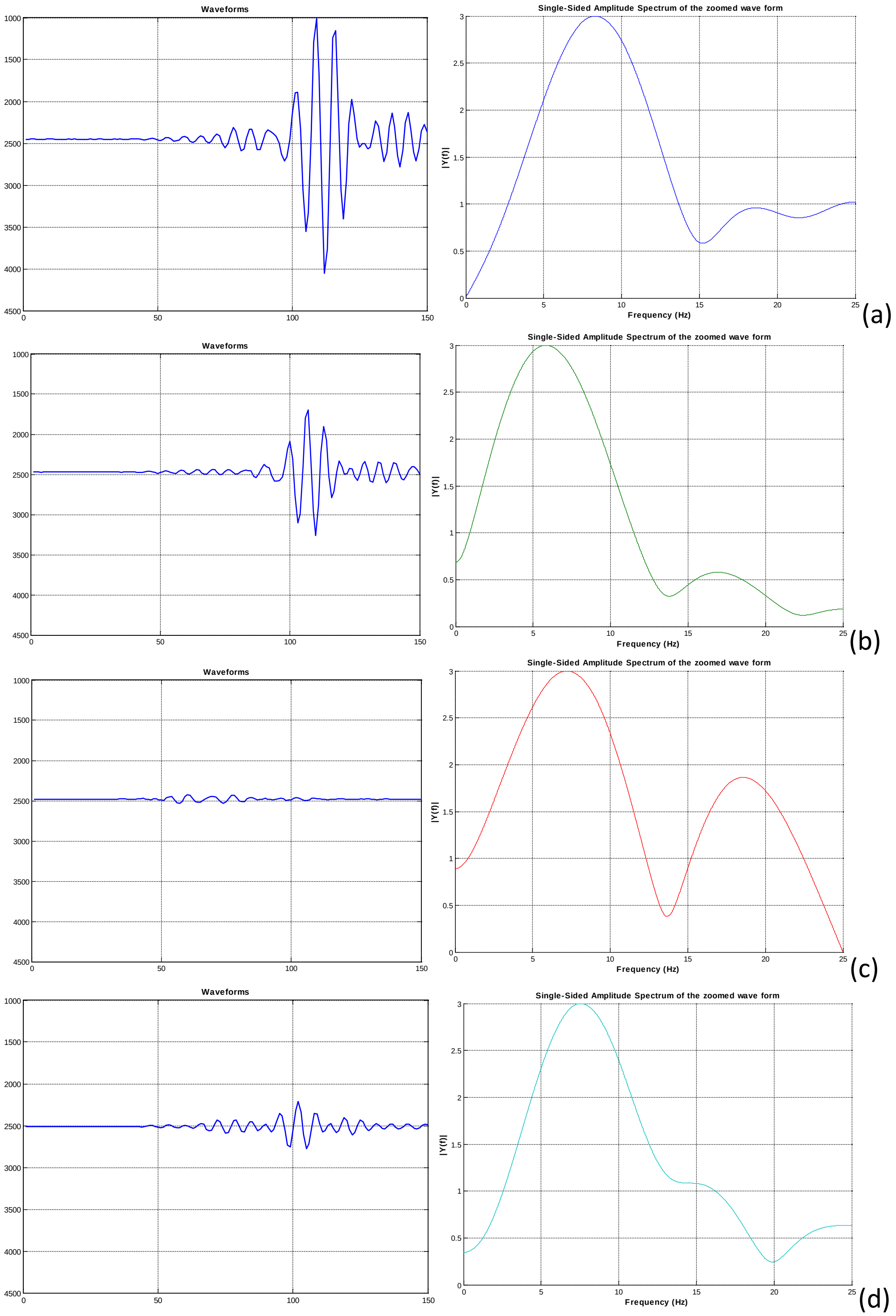

Figure 101. Selected waveforms for frequency analysis. One waveform (a) was selected above the hydrate zone, two waveforms (b, and c) from within the hydrate zone and one waveform (d) from below the hydrate layer. We observed a frequency shift which indicates a higher attenuation within the hydrate layer. Also below the hydrate zone the frequency content increases but it does not get back to the value calculated above the hydrate zone

F. References

Ecker, C. Dvorkin, J., Nur, A., 1998, Sediments with gas hydrates: Internal structure from seismic AVO, Geophysics. 63(5), 1659–1669. doi: 10.1190/1.1444462.

Dvorkin, J., Berryman, J., Nur, A., 1999, Elastic moduli of cemented sphere packs, Mechanics of Materials. 31, 461-469

Dautriat, J., M. Bornert, N. Gland, A. Dimanov, and J. Raphanel, 2011, Tectonophysics Localized deformation induced by heterogeneities in porous carbonate analysed by multi-scale digital image correlation: Tectonophysics, 503, 100–116.

Fabricius, I. L. 2003. How burial diagenesis of chalk sediments controls sonic velocity and porosity. AAPG Bulletin, 87(11), 1755{1778}.

Fusseis, F., X. Xiao, C. Schrank, and F. D. Carlo, 2014, Review article A brief guide to synchrotron radiation-based microtomography in (structural) geology and rock mechanics: Journal of Structural Geology, 65, 1–16.

Guerin, G., and Goldberg, D., 2002. Sonic waveform attenuation in gas hydrate–bearing sediments from the Mallik 2L-38 research well, MacKenzie Delta, Canada. J. Geophys. Res., 107:2088. doi:10.1029/2001JB000556

Gupta, A., 2007. Methane Hydrate Dissociation Measurements and Modeling: The Role of Heat Transfer and Reaction Kinetics, Ph.D. Thesis, Colorado School of Mines, Department of Chemical Engineering

Krishna K. Mohan, Ravimadhav N. Vaidya, Marion G. Reed, H. Scott Fogler, 1993. Water sensitivity of sandstones containing swelling and non-swelling clays, Colloids and Surfaces A: Physicochemical and engineering Aspects. 73 (1993) 237-254

Helgerud, M. B., Dvorkin, J., Nur, A., Sakai, A., Collett, T. S., 1999, Elastic wave velocity in marine sediments with gas hydrates: Effective medium modeling, Geophysical Research Letters. 26(13), 2021–2024. doi: 10.1029/1999GL900421.

Lee, J. Y., Yun, T. S., Santamarina, J. C., Ruppel, C., 2007. Observations Related to Tetrahydrofuran and Methane Hydrates for Laboratory Studies of Hydrate-Bearing Sediments. Geochemistry Geophysics Geosystems An Electronic Journal of the Earth Sciences, 8 (6)

Lee, M.W., T. S.Collett, and T. L. Inks, 2009, Seismic-attribute analysis for gas-hydrate and free-gas prospects on the North Slope of Alaska, in T. S. Collett, A. Johnson, C. Knapp, and R. Boswell, eds., Natural gas hydrates—Energy resource potential and associated geologic hazards. AAPG Memoir 89, p. 541–554.

Lenoir, N., M. Bornert, J. Desrues, P. Besuelle, and G. Viggiani, 2007, Volumetric Digital Image Correlation Applied to X-ray Microtomography Images from Triaxial Compression Tests on Argillaceous Rock: 193–205

Revil, A, N. Florsch and C. Camerlynck (2014). Spectral Induced Polarization Porosimetry, *Geophysical Journal International*, GJI Marine geosciences and applied geophysics, Vol. 198, p. 1016-1033

Sell, K., Chaouachi, M.and Falenty, A., Saenger, E. H., Khan, F.and Schwarz, J.-O., Enzmann, F., Kersten M., and Kuhs, W. F. 2015. Microstructure of hydrate-bearing sediments and determination of P-wave velocities based on high-resolution synchrotron tomographic data. In: Proceedings of the SEG annual meeting, October 2015, New Orleans.

Toksöz, M.N., Johnston, D.H., and Timur, A., (1978), Attenuation of seismic waves in dry and saturated rocks: 1. Laboratory measurement; Geophysics, 44, 681-690.

Winkler, K. W., and Nur, 1982, Seismic attenuation: Effects of pore fluids and frictional sliding: Geophysics, 47, no. 1, 1-15.

G. Products

Publications (Publications; Conference Papers, Presentations, Books)

Peer – reviewed publications

Schindler, M., M. L. Batzle and M. Prasad, 2016, Micro X-Ray computed tomography imaging and ultrasonic velocity measurements in tetrahydrofuran-hydrate-bearing sediments, Geophysical Prospecting, doi: 10.1111/1365-2478.12449

Pohl, M., Prasad, M., Ultrasonic Attenuation of Pure THF-Hydrate: in review with Geophysical Prospecting

Book Chapter

Schindler, M. and Batzle, M. L. 2014. Pore-scale investigation of hydrate-bearing sediments. In: Pore Scale Phenomena: Frontiers in Energy and Environment (eds J. M. Poate, H. Kazemi, T. H. Illangasekare, and R. J. Kee). World Scientific, Golden, CO, USA.

Conference presentations and expanded abstracts

Schindler, M., Pohl, M., Livo, K., Prasad, M. 2017. Understanding Seismic and Petrophysical Indications of Pure Hydrates and Hydrate-bearing Sediments. ICGH 9 to be held in Golden CO.

Schindler, M. and Prasad, M. 2016. Micro X-ray CT Imaging of Sediments under Conning Pressure. SEG Annual Meeting Expanded Abstract, Dallas, 17 - 21 October, 2016

Schindler, M., M. L. Batzle and M. Prasad. 2015. Pore-Scale Imaging of Tetrahydrofuran-Hydrate Bearing Porous Media. SEG Annual Meeting Expanded Abstract, New Orleans, 19 - 23 October, 2015

Schindler, M., Kneafsey, T. J. and Nakagawa, S. 2015. N2/CO2 Substitution in Methane-Hydrate Bearing Sediments, Proceedings of the Third International Workshop on Rock Physics (3IWRP), Perth, Western Australia, 13 - 17 April, 2015

Pohl, M., M. Prasad and M. L. Batzle, 2015, Ultrasonic Attenuation of Pure THF-Hydrates: Third International Workshop on Rock Physics, Expanded Abstracts.

Pohl, M., M. Prasad and M. L. Batzle, 2015, Ultrasonic Attenuation of Pure THF-Hydrates: Third International Workshop on Rock Physics, Expanded Abstracts.

Schindler, M. and Batzle, M. L. 2014. Pore-Scale Imaging and Ultrasonic Velocity Measurements of THF-Hydrate Bearing Sediments, Proceedings of the 8th International Conference on Gas Hydrates (ICGH8-2014), Beijing, China, 28 July - 1 August, 2014

Pohl, M., and M. L. Batzle, 2013, Low frequency and ultrasonic velocity measurements of THF hydrate-bearing Foxhill Sandstone: Second International Workshop on Rock Physics, Expanded Abstracts.

Pohl, M., M. Rydzy and M. L. Batzle, 2013, Investigating the influence of clay content on ultrasonic velocities of THF hydrate-bearing sediment: Second International Workshop on Rock Physics, Expanded Abstracts.

Pohl, M., M. Rydzy and M. L. Batzle, 2013, Investigating the influence of clay content on ultrasonic velocities of THF hydrate-bearing sediment: Second International Workshop on Rock Physics, Expanded Abstracts.

Schindler, M. and Batzle, M. L. 2013. Rock Physics Characterization of Hydrate Bearing Porous quency and ultrasonic velocity measurements of THF hydrate-bearing Foxhill Sandstone: Second International Workshop on Rock Physics, Expanded Media Using Micro X-Ray Computed Tomography and Ultrasonic Velocity Measurements, AGU Fall Meeting, San Francisco, 9 – 13 December, 2013

Presentations and papers to various Annual Industry consortia meetings

DHI/Fluids (about 25 industry sponsors)

Mathias Pohl and Manika Prasad, 2016, Ultrasonic Velocities and Attenuation of Clay Filled Sand Packs before and after Hydrate Formation

Schindler, M. and Prasad, M. 2016. MicroX-Ray CT Imaging of Sediments under Confining Pressure

Schindler, M. and Prasad, M. 2016. Recent Developments in Micro X-ray CT Imaging at Center for Rock Abuse

Mathias Pohl, Manika Prasad, Dawid Szewczyk, 2015, Interlaboratory Comparison Study: A Comparison of Low Frequency Measurements at two laboratories between SINTEF and CSM

Schindler, M. and Prasad, M. 2015. Recent Developments in Micro X-ray CT Imaging at Colorado School of Mines

Mathias Pohl and Mike Batzle, 2014, Ultrasonic Attenuation of Pure THF-Hydrate

Schindler, M. 2014. N2/CO2 Substitution in Methane-Hydrate Bearing Sediments

Patricia E. Rodrigues, Mathias Pohl and Michael L. Batzle, 2013, Advances in Low Frequency Measurements for Soft Samples

Schindler, M. and Batzle, M. L. 2013. Pore-Scale Imaging and Ultrasonic Velocity Measurements of Hydrate-Bearing Sediments

OCLASSH (about 10 industry sponsors)

Schindler, M. and Prasad, M. 2016. Recent Developments in Micro X-ray CT Imaging at Center for Rock Abuse

ROSE Meeting, NTNU Trondheim

Schindler, M. and Prasad, M. 2016. Laboratory measurements on THF-hydrate bearing porous media